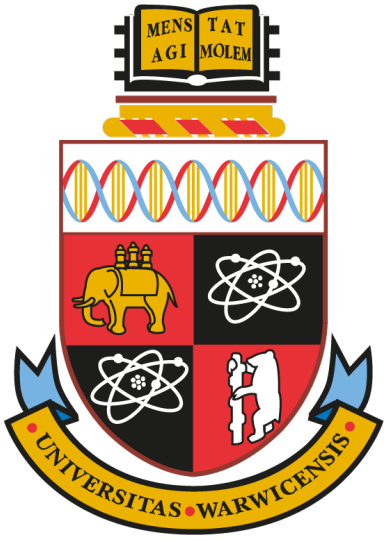


Searching for Orbital Decay with NGTS and TESS

by

Alexander James Romanec

Thesis

Submitted to the University of Warwick

for the degree of

Master of Science (by Research) in Physics

Department of Physics

August 2026

UNIVERSITY OF WARWICK

Contents

List of Tables **iv**

List of Figures **v**

Acknowledgments **vii**

0.1 Personal Acknowledgement vii

0.2 Data Acknowledgement viii

Declarations **x**

Abstract **xii**

Abbreviations **xiii**

Chapter 1 Introduction **1**

1.1 Introduction to Exoplanets 1

1.2 Hot Jupiters 3

1.2.1 Formation 3

1.2.2 Migration 4

1.2.3 Hot Jupiter Properties 5

1.3 Exoplanet Transits 5

1.3.1 Transit Geometry 7

1.3.2 Limb Darkening 8

1.3.3 Transit Timing 10

1.4 Exoplanet Transit Surveys 12

1.4.1 TESS 12

1.4.2 NGTS 16

1.5 Tidal Effects in Planetary Systems 20

1.5.1 Tides 20

1.5.2 Tidal Evolution Overview 23

1.5.3 Tidal Quality Factor . . . 23
1.5.4 Orbit circularization . . . 24
1.5.5 Tidal Decay . . . 25
1.6 Orbital Decay False Positives . . . 28
1.6.1 Rømer (Light Travel-Time) Effect . . . 28
1.6.2 Applegate Mechanism . . . 30
1.6.3 Apsidal Precession . . . 31
1.7 Timing Inhomogeneities . . . 32
1.8 Project Objectives . . . 33

Chapter 2 The NGTS Orbital Decay Programme I: Monitoring of 15 Ultra-Short Period Transiting Hot Jupiter and Brown Dwarf Systems 35
2.1 Introduction . . . 36
2.2 Sample Selection . . . 41
2.3 Observations . . . 42
2.3.1 NGTS Observations . . . 42
2.3.2 *TESS* Observations . . . 44
2.3.3 Danish Telescope Observations . . . 46
2.4 Literature Transit Times . . . 47
2.5 Data Analysis . . . 51
2.5.1 Normalization and de-trending . . . 51
2.5.2 Transit Model Fitting . . . 53
2.5.3 Transit Time Fit . . . 54
2.5.4 Danish Telescope Fitting . . . 56
2.5.5 Ephemeris Fit . . . 57
2.6 Results . . . 59
2.6.1 WASP-4 b . . . 59
2.6.2 WASP-18 b . . . 68
2.6.3 WASP-19 b . . . 68
2.6.4 WASP-43 b . . . 69
2.6.5 WASP-103 b . . . 69
2.6.6 HATS-18 b . . . 70
2.6.7 NGTS-6 b . . . 70
2.6.8 NGTS-10 b . . . 71
2.6.9 TOI-2109 b . . . 71
2.6.10 NGTS-7A b . . . 71

2.6.11 HATS-70 b . . . 72
2.6.12 WASP-128 b . . . 72
2.6.13 WASP-87 b . . . 73
2.6.14 WASP-78 b . . . 73
2.6.15 Qatar-2 b . . . 73
2.7 Discussion . . . 74
2.7.1 Tidal Decay Candidates . . . 74
2.7.2 Systems with other Timing Shifts . . . 75
2.7.3 Gaia Astrometry . . . 75
2.7.4 Ephemeris Updates . . . 78
2.7.5 Transit Timing Precision . . . 78
2.7.6 Future Follow-up . . . 79
2.8 Conclusion . . . 81
2.9 Decay Candidate Stellar Parameters . . . 82
2.10 Decay Candidate Planetary Parameters . . . 83
2.11 Observation summaries . . . 85
2.12 References for Literature Transit Times . . . 87

Chapter 3 Outlook **92**
3.1 Summary . . . 92
3.2 Future Work . . . 93
3.2.1 Further Analysis . . . 93
3.2.2 Further Targeted Observations . . . 95
3.2.3 Project continuation . . . 96
3.3 Conclusion . . . 97

List of Tables

2.1 Mid-transit times derived in this work 50
2.2 Results table, showing our updated system ephemerides, preferred ephemeris model and derived decay rates and $Q'_\star$ values or their upper limits 58
2.3 *Gaia* RUWE values for the targets in this study 76
2.4 Stellar parameters for the targets in this study 82
2.5 Planetary parameters for the targets in this study 84
2.6 Summary of NGTS observations presented in this work. 86
2.7 Continuation of Table 2.6 88
2.8 Summary of Danish 1.54m Telescope observations presented in this work. 89
2.9 Summary of *TESS* observations presented in this work. 90
2.10 Continuation of Table 2.9 91

List of Figures

1.1 Cumulative count of exoplanet detections over time, sorted by discovery method. 2
1.2 Diagram and theoretical light curve of an exoplanet transit 6
1.3 Geometry of an exoplanet transit 7
1.4 Demonstration of the effect of limb darkening as a function of wavelength 9
1.5 Diagram of the *TESS* spacecraft and artist's impression of it in space 12
1.6 Bandpass of the *TESS* telescope cameras 13
1.7 Diagram of *TESS*'s observing strategy 13
1.8 *TESS* observing coverage up to Sector 92 14
1.9 Example *TESS* light curve 15
1.10 Photograph of the NGTS facility 17
1.11 Illustration of the NGTS bandpass 18
1.12 Example NGTS Light Curve 19
1.13 Geometric illustration of tidal forces between two bodies 21

2.1 Orbital periods, masses and brightnesses of the targets in this study. 40
2.2 Sky position of the targets in this study 41
2.3 Timeline of observations taken in this study 43
2.4 Example *TESS* light curve showing transit data extraction 44
2.5 Example NGTS light curve 45
2.6 Demonstration of the light curve normalisation method 52
2.7 Demonstration of the method for fitting precise mid-transit times . . 55
2.8 O-C diagram for WASP-4 60
2.9 O-C diagram for WASP-18 60
2.10 O-C diagram for WASP-19 61
2.11 O-C diagram for WASP-43 61
2.12 O-C diagram for WASP-103 62

2.13 O-C diagram for HATS-18 62
2.14 O-C diagram for NGTS-6 63
2.15 O-C diagram for NGTS-10 63
2.16 O-C diagram for TOI-2109 64
2.17 O-C diagram for NGTS-7 A 64
2.18 O-C diagram for HATS-70 65
2.19 O-C diagram for WASP-128 65
2.20 O-C diagram for WASP-87 66
2.21 O-C diagram for WASP-78 66
2.22 O-C diagram for Qatar-2 67
2.23 Median T_c error against target brightness 77
2.24 Position of targets in this programme within *PLATO*'s LOPS2 field 80

Acknowledgments

0.1 Personal Acknowledgement

My first thanks must go to my supervisors, Dan Bayliss and Ed Bryant. Firstly - for taking me as a student! When we had our first meetings, I was extremely unsure of the direction my career was heading. Speaking to you at 2am from my un-insulated rental house on the South Island of New Zealand in mid-winter was certainly a unique start to a supervisor relationship, but from the very start the plan you laid out caught my interest and I am so glad we made it work.

Dan, your commitment to your students is unparalleled, as demonstrated by the network of loyal former MSc and PhD students of yours that I have been fortunate enough to be able to call on for various reasons through my time at Warwick (particular thanks must go to Yoshi and Toby!). And Ed, having you down the corridor to ask a quick question of or get some advice has been invaluable. I am also immensely appreciative of the support you both gave me in gaining a PhD position, and I hope to remain in touch long after I start the next phase of my scientific career.

This year would not have been the same without the supportive environment and close relationship amongst the Warwick astro PGRs. From unhinged lunchtime conversations and Fat Hippo trips to genuine support and encouragement when things have been hard, I am immensely sad to leave this group. The close friendships I have made this year will, I hope, last for long after I have moved on. While winning the pub quiz without me will be hard, I'll try and come back to help you occasionally :))

Looking back at my year at Warwick, I couldn't not mention the trips I have taken with Warwick Mountains, escaping Coventry for the weekend. These chaotic, wet expeditions to remote mountains in tiny cars have unquestionably been a highlight of my year here, and I will look back with extreme fondness to the adventures I have had. Type 2 fun is unbeatable at mitigating research stress!

Lastly, without the support of my family this year would simply not have been possible. I am immensely grateful for the backing you have always given me to pursue my ambitions.

0.2 Data Acknowledgement

This research has made use of the NASA Exoplanet Archive, which is operated by the California Institute of Technology, under contract with the National Aeronautics and Space Administration under the Exoplanet Exploration Program. We acknowledge the use of *TESS* High Level Science Products (HLSP) produced by the Quick-Look Pipeline (QLP) at the *TESS* Science Office at MIT. This paper includes data collected by the TESS mission, which are publicly available from the Mikulski Archive for Space Telescopes (MAST). Funding for the TESS mission is provided by NASA's Science Mission directorate. This work is based on data collected under the NGTS project at the ESO Paranal Observatory. The NGTS facility is operated by a consortium institutes with support from the UK Science and Technology Facilities Council (STFC) under projects ST/M001962/1, ST/S002642/1 and ST/W003163/1. The operation, servicing and maintenance of the DK-1.54m telescope is supported by a Villum Young Investigator grant (project number 25501) and a Villum Experiment grant (VIL69896) from VILLUM FONDEN. This work has made use of data from the European Space Agency (ESA) mission *Gaia* (`https://www.cosmos.esa.int/gaia`), processed by the *Gaia* Data Processing and Analysis Consortium (DPAC, `https://www.cosmos.esa.int/web/gaia/dpac/consortium`). Funding for the DPAC has been provided by national institutions, in particular the institutions participating in the *Gaia* Multilateral

Agreement.

Declarations

This thesis is submitted to the University of Warwick in support of my application for the degree of Master of Science (by Research). This work was carried out at the University of Warwick in the period September 2025 to August 2026, under the supervision of Professor Daniel Bayliss and Dr Edward Bryant. It has been composed by myself and has not been submitted in any previous application for any degree.

The work presented in chapter two of this thesis has been submitted as a research paper to the *Monthly Notices of the Royal Astronomical Society*, entitled 'The NGTS Orbital Decay Programme I: Monitoring of 15 Ultra-Short Period Transiting Hot Jupiter and Brown Dwarf Systems'. All work on this paper was carried out by myself with the exception of:

- Scheduling, operations and observations at the NGTS facility, as well as the production of NGTS light curves, was carried out by co-author Fernández and other members of the NGTS consortium.
- Scheduling and observations at the 1.54 m Danish Telescope was carried out by members of the MiNDSTEp consortium.
- The observations used in this work from the 1.54 m Danish Telescope were analysed by co-author Southworth and co-author Limb.
- Sections of Chapter 2 relating to observations and analysis of the data from the 1.54 m Danish Telescope (Section 2.3.3, Section 2.5.4 and Table 2.8) were written by co-author Southworth.

- Calculations of the orbit of NGTS-7 A in Section 2.7.2 were performed by co-author Harre
- Contributions to the text in Sections 2.7.3 and 2.7.6, concerning observations from *Gaia*, were made by co-authors Venner and Kelehan
- Contributions to the text of Section 2.7.6 concerning the *PLATO* mission were made by co-author Eschen
- Figures 2.2 and 2.24 were provided by co-author Eschen
- The full author list of this work is: Alex Romanec, Daniel Bayliss, Edward Bryant, John Southworth, Jorge Fernández-Fernández, Jan-Vincent Harre, Alexis M. S. Smith, Yoshi Nike Emilia Eschen, David Anderson, Ioannis Apergis, Catalina Àvalos-Vega, Matthew P. Battley, Valerio Bozza, Matthew R. Burleigh, Richard E. Cannon, Sarah L. Casewell, Josephin Chamoun-Contreras, Benjamin D. R. Davies, Martin Dominik, Abbie Donaldson, Troy Edkins, Fintan Eeles-Nolle, R. Figuera Jaimes, Samuel Gill, Edward Gillen, Michael R. Goad, George Harvey, Tobias Cornelius Hinse, James S. Jenkins, Cameron Kelahan, Alicia Kendall, Elahe Khalouei, Monika Lendl, Dan J. D. Lewis, Georgina Limb, Isobel S. Lockley, Penélope Longa-Peña, Luigi Mancini, James McCormac, Ayush Moharana, Maximiliano Moyano, Cyrielle Opitom, Nuno Peixinho, Markus Rabus, Gavin Ramsay, Jose Ricra, Toby Rodel, Suman Saha, Sedighe Sajadian, Amber Sedgley, Lixian Shen, Jesper Skottfelt, Colin Snodgrass, Stephane Udry, Alexander Venner, Roberta Vieliute, Jose I. Vines, Richard G. West, Peter J. Wheatley, Mauritz Wicker & Tafadzwa Zivave.

Abstract

Through long term monitoring of transit-timing variations in ultra-short period ($P_{orb} \lesssim 2$ days) hot Jupiter and brown dwarf systems, it is possible to gain insight into the tidal interactions present in these environments and probe the structure and energy dissipation properties of the host star. In this thesis I present my work on the Next Generation Transit Survey (NGTS) Orbital Decay Programme, a long term observational campaign to detect transit timing variations in 15 such systems. In this thesis I analyse 85 transit observations from the NGTS facility and 1362 from the *TESS* observatory. I combine these with 45 observations from the 1.54 m Danish telescope and 538 transit times taken from the peer reviewed literature. I derive update orbital ephemerides for these systems and test whether they show evidence for long-term period changes. In the WASP-4 system, I identify an apparent period increase, consistent with previous studies, that may betray the presence of an unseen companion. I identify a positive period trend in the NGTS-7 A system, suggestive of an unseen companion to this system. I find suggestions of apparent period shifts in the WASP-43, WASP-103 and WASP-128 systems, and discuss the possibility of these being due to tidal decay or other processes such as the light travel-time effect from an outer companion or apsidal precession. I derive limits on stellar tidal dissipation factors for systems where no period change is found. Finally, I discuss the impact that continued observations with *NGTS* and *TESS*, and future observations from the *Gaia* and *PLATO* missions will have on constraining the behaviour of these systems.

Abbreviations

NGTS Next Generation Transit Survey

WASP Wide-Angle Search for Planets

PLATO PLAnetary Transits and Oscillations of stars

TESS Transiting Exoplanet Survey Satellite

TIC *TESS* Input Catalogue

PIC *PLATO* Input Catalogue

FFI Full Frame Image

QLP Quick-Look-Pipeline

SPOC Science Processing and Operations Center

MAST Mikulski Archive for Space Telescopes

LTTE Light Travel-time effect

TTV Transit Timing Variation

HEM High-Eccentricity Migration

CCD Charge-Couple Device

BJD Barycentric Julian Date

HJD Heliocentric Julian Date

TDB Barycentric Dynamical Time

UTC Co-ordinated Universal Time

IW Inertial Wave

IGW Internal Gravity Wave

Chapter 1

Introduction

1.1 Introduction to Exoplanets

Throughout history, humanity has long speculated that the planet we inhabit is not alone in the Universe. References to the possibility of other planets date back to antiquity, with the Greek philosopher Epicurus (341–270 BCE) writing "there are infinite worlds both like and unlike this world of ours." (Epicurus, Letter to Herodotus 45, translated in Bailey [1926]). The rise of the Copernican philosophy in renaissance Europe led to a resurgence in ideas of other worlds, however this was initially not welcomed by the religious ruling class of the time. The Italian philosopher Giordano Bruno was burned at the stake for heresy for suggesting that the universe was infinite and contained "infinite worlds" (D'Amico [2000], referenced in Trotta [2024]). These attitudes evolved with the progress of the scientific revolution, with the English astronomer Thomas Wright writing of solar systems around other stars and estimating up to 60,000,000 planets "within the Radius of the visible Creation" [Wright, 1750].

With advancements in astronomical technology and thinking during the 20th century, there were many attempts to discover and confirm planetary bodies outside our solar system. This was initially pursued through using high precision radial velocity measurements of bright stars to look for reflex motion from an orbiting companion, leading to the first suggestions of the presence of sub-stellar companions to nearby stars [Campbell et al., 1988; Marcy & Benitz, 1989; Cochran & Hatzes, 1994]. However the first definitive confirmation of the presence of sub-stellar objects came through pulsar timing measurements, leading to the detection of Earth-mass rocky bodies around neutron stars [Wolszczan & Frail, 1992]. The first detection of a planet around a solar-type star was in 1995 with the discovery of the Hot Jupiter

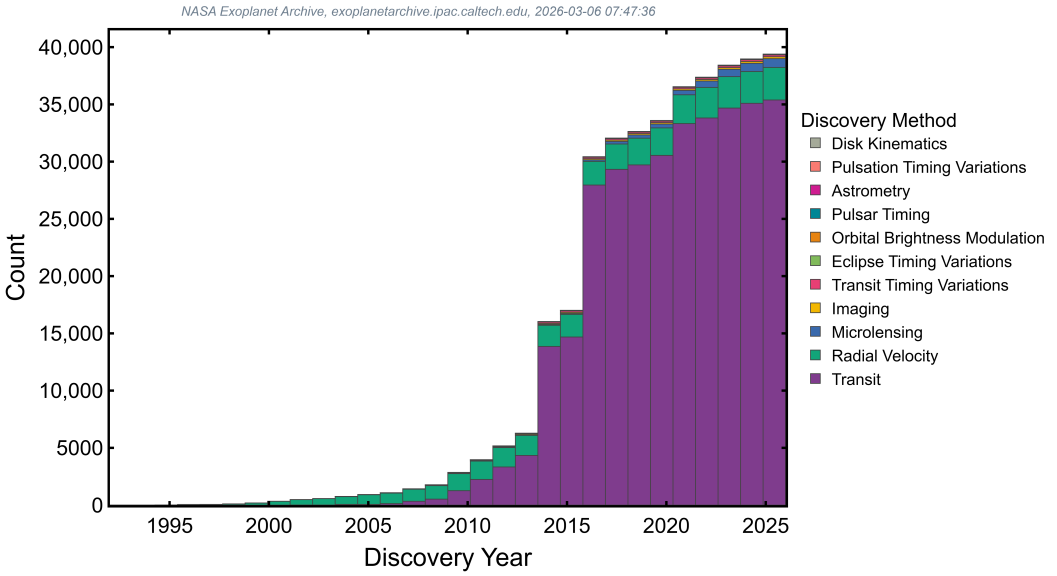


Figure 1.1: Cumulative total number of exoplanets discovered over time, sorted by discovery method. Figure taken from the NASA Exoplanet Archive (https://exoplanetarchive.ipac.caltech.edu/) as of 2026-03-06.

51 Pegasi b [Mayor & Queloz, 1995], a discovery for which the authors were awarded the 2019 Nobel Prize for Physics.

The first detection of an extra-solar planet transiting a star was made by Charbonneau et al. [2000], which paved the way for transit discovery to lead in detection of exoplanet systems. Early ground-based surveys such as HAT [Hungarian-made Automated Telescope; Bakos et al., 2004], WASP [Wide-Angle Search for Planets; Pollacco et al., 2006] and KELT [Kilodegree Extremely Little Telescope; Pepper et al., 2007] contributed significantly to the early exoplanet population, and many planets discovered by these campaigns remain some of the most studied today. Significant leaps in exoplanet discovery came with the advent of space-based transit surveys such as *CoRoT* [COnvection, ROtations et Transits planétaires; Auvergne et al., 2009] and particularly *Kepler* [Borucki et al., 2010]. In the current era, the *TESS* mission [Transiting Exoplanet Survey Satellite; Ricker et al., 2015] is performing a systematic survey of the entire sky and has found 759 confirmed planets and over 7,800 planet candidates [1]. Looking to the future, the launch of ESA's PLATO mission [PLAnetary Transits and Oscillations of stars; Rauer et al., 2025] will massively add to the known sample of transiting exoplanets.

[1]NASA Exoplanet Archive, https://exoplanetarchive.ipac.caltech.edu/, as of 09/03/2026

1.2 Hot Jupiters

In this work I am studying a subclass of exoplanets at ultra-short orbital periods with masses and radii comparable to that of Jupiter in our solar system. These are known as hot Jupiters and although they have no analogue in our Solar System, there are currently 269 known systems falling within this category[2], making them an important planetary population to understand.

1.2.1 Formation

Hot Jupiters form, like all planets, within a protoplanetary disk. However, the exact process by which this happens and where in the disk the planets form remains an open question. Generally speaking, conditions in a protoplanetary disk very close to a star are not conducive to the formation of giant planets *in situ*, and therefore hot Jupiters are likely to have formed further out and migrated inwards later in their lifetimes [Dawson & Johnson, 2018]. In this section I provide a brief summary of the main formation mechanisms of hot Jupiters.

The two principle methods for planet formation are gravitational instability and core accretion. Formation through gravitational instability [as reviewed in Durisen et al., 2007] involves the collapse of density perturbations in the spiral arms of a protoplanetary disk into self-gravitating clumps which, if able to cool on sufficient time-scales, can form a planet. The conditions for gravitational instability [Toomre, 1964] require the self-gravitational attraction of a region of a disk to be large enough to resist sheer forces within the disk. These conditions are unlikely to be satisfied close-in to a protostar [Dawson & Johnson, 2018], with high pressure and fast rotation preventing gravitational collapse, and the high temperatures resulting in a lower gas density than necessary. In addition, Rafikov [2005] argued that any gravitational fragments that do form would be rotationally sheared apart before they had a chance to cool and contract unless the temperature was significantly raised.

Core Accretion [Pollack et al., 1996], requires the accretion of gas onto a rocky ($\sim$10 $M_\oplus$) core. A core will accrete hot or cold gas just as efficiently, but the problem in forming the core requires both that there is sufficient mass in the disk to form it, and that the lifetime of the disk is larger than the timescale to grow the core [Dawson & Johnson, 2018]. While the short orbital periods mean that the core can usually form in the required timescale [Dawson & Johnson, 2018], close-in regions of protoplanetary disks are unlikely to have the required mass of solids to form these

[2] `https://exoplanetarchive.ipac.caltech.edu/`, accessed 26/08/26

cores [Schlichting, 2014], and the formation of giant planets at short orbital periods by core accretion remains an open problem.

1.2.2 Migration

If a hot Jupiter does form further out in the disk, it must therefore migrate inwards in order to adopt its current position. This can happen via migration through the protoplanetary disk or by high-eccentricity migration (HEM) resulting from a perturbation from a companion.

Disk migration [Goldreich & Tremaine, 1980; Baruteau et al., 2014] involves the gravitational interaction between material in a disk and the planet, reducing both its orbital energy and angular momentum such that the orbit shrinks. This method was originally proposed for the formation of 51 Peg b, with the migration of the planet halted by either angular momentum exchange with the young star or with its magnetic field [Lin et al., 1996]. This mechanism is likely to keep the eccentricity of the planets at relatively low levels, in contrast with HEM [Dawson & Johnson, 2018].

The process of HEM involves a planet at wide orbital periods being excited to a high-eccentricity orbit with a close periapsis, which, through tidal interactions with the star, then circularises at a low orbital period. This circularisation process happens due to tidal processes, as explained in Section 1.5.4.

The initial exciting of the planet onto a high eccentricity orbit can occur through planet-planet scattering [Rasio & Ford, 1996], where interactions between planets lead to a dynamical instability, resulting in one planet being ejected from the system and another being pushed onto a high eccentricity orbit. Alternatively, secular interactions between planets in the system, slow exchanges of angular momentum that occur over timescales of up to millions of years, can result in planets being knocked into shorter orbits. An example of these is Kozai-Lidov migration [Kozai, 1962; Lidov, 1962], first studied for satellites in our solar system but thought to be responsible for the inward migration of planetary systems. This involves interaction between the planet and a companion at a different inclination, and the resulting transfer of angular momentum causes the increased eccentricity of the planet [Dawson & Johnson, 2018].

We are now left with a hot Jupiter exoplanet on a short period orbit, with non-zero eccentricity. As discussed in Section 1.5, tidal evolution in these systems may result in the circularisation and eventual in-spiral and engulfment of the planet, which will be the focus of this thesis.

1.2.3 Hot Jupiter Properties

Hot Jupiter exoplanets, due to the extreme environments which they inhabit, exhibit properties not seen among planets in our solar system. These include inflated radii relative those expected, evaporating atmospheres and extreme surface conditions.

Hot Jupiters with high ($> 1000\,K$) equilibrium temperatures are observed to have radii inflated above that expected by standard planetary evolution models [Fortney et al., 2021]. A combination of mechanisms that either slow the rate of cooling in the planets or deposit more heat into the planet have been proposed to explain this feature, however no single mechanism has been found to fully explain this effect [Fortney et al., 2021; Sarkis et al., 2021].

The first detection of an exoplanetary atmosphere was made by Charbonneau et al. [2002] for the hot Jupiter HD 209458 b with transmission spectroscopy, measuring the spectrum of the planets atmosphere as it transits the star. Since then, spectroscopy of hot Jupiter atmospheres has yielded observations of molecules such as water [e.g. Kreidberg et al., 2015] and CO [e.g. Madhusudhan et al., 2011], with higher resolution spectroscopy [Birkby, 2018] providing additional detail into the extreme wind patterns present on these planets [e.g. Ehrenreich et al., 2020]. In extreme cases, observations have shown that in the high radiation environment that hot Jupiters inhabit, their atmospheres can be observed to be escaping [e.g. Owen, 2019; Allart et al., 2025].

1.3 Exoplanet Transits

To date, the most common method by which exoplanets have been discovered is through transit photometry (see Figure 1.1). This is the effect through which a decrease in apparent flux from the star is caused by the planet passing in front of the stellar disk in the observer's line of sight, and will be the focus of the work undertaken in this thesis.

From a historical perspective, the primary experience humanity has had of this effect is through eclipses of Earth's sun and moon, most dramatically through a total solar eclipse, where the moon entirely blocks the sun's disk, leaving apparent darkness in its shadow. Additionally, transits of Venus and Mercury on the sun have long been observed. Exoplanet transits, while not spatially resolved for an observer, arise from the same effect. The terminology *eclipse* refers to the conjunction of any two astronomical bodies, while *transit* is used to describe the passage of a significantly smaller body in front of a larger one, and *occultation* a smaller body passing behind a larger body, as illustrated in Figure 1.2. In this section I describe

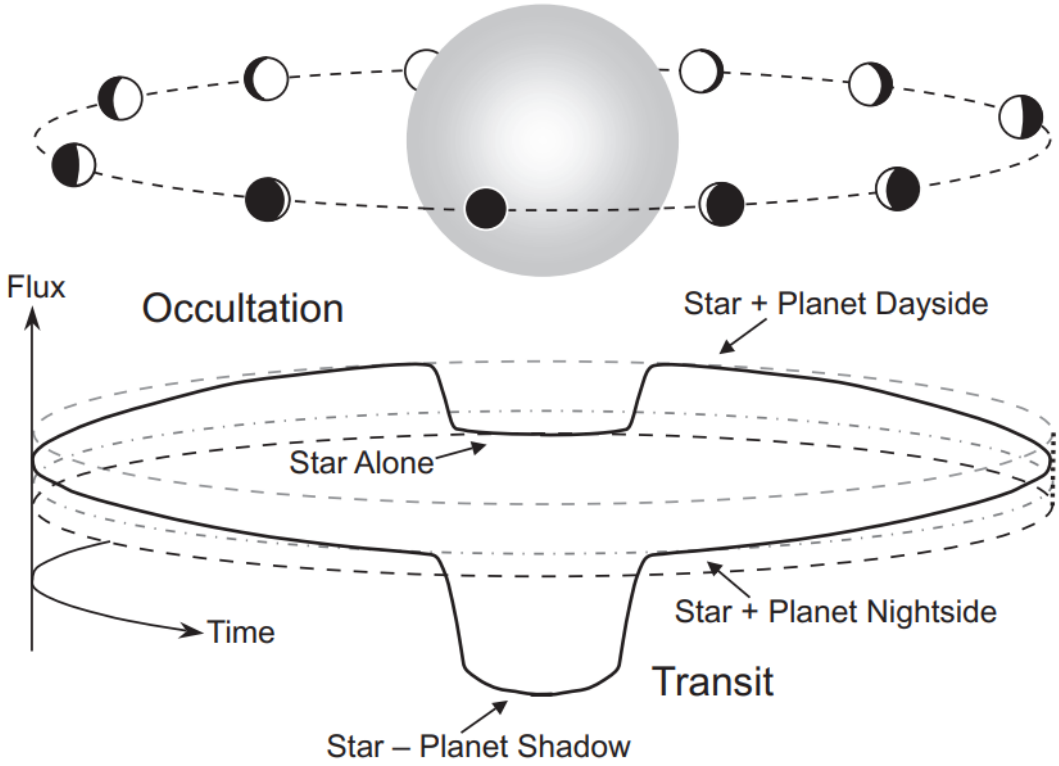


Figure 1.2: Diagram illustrating the geometry of a primary and secondary transit during an exoplanet's orbit. Figure from Winn [2010].

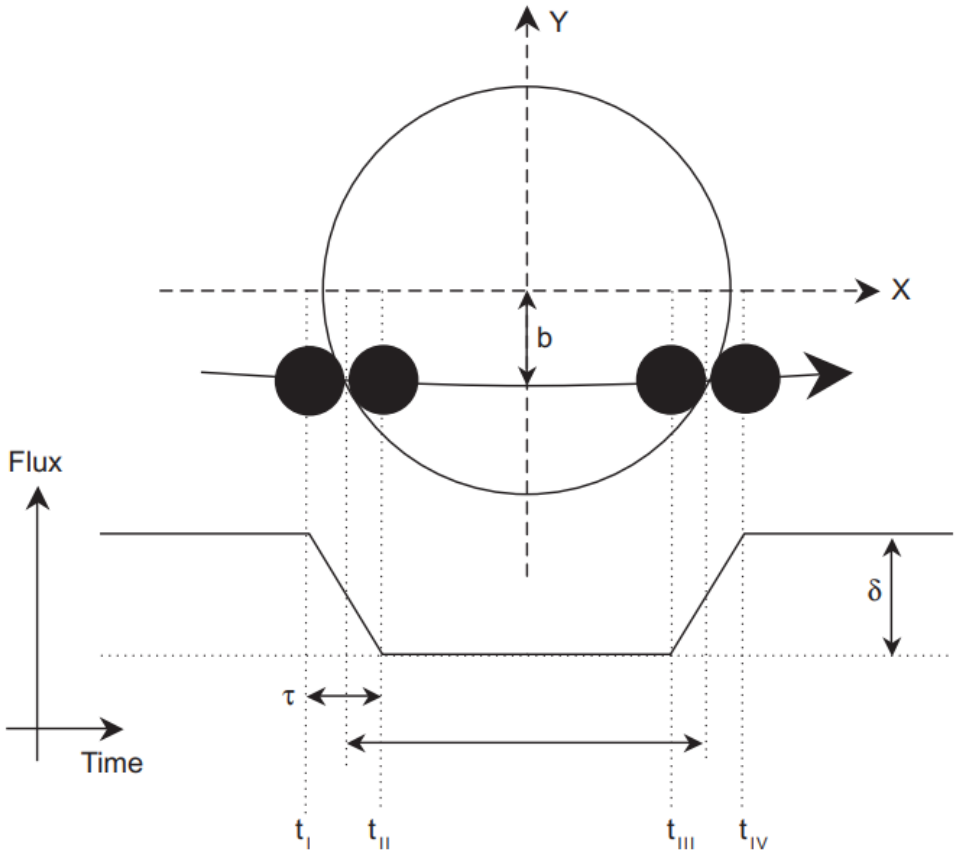


Figure 1.3: The geometry of an exoplanet transit. The top panel shows a planet at various stages along its transit chord across the star, with the resulting light curve shown in the bottom panel. Here, b is the transit impact parameter, δ is the depth of the transit, τ is the duration of ingress and t_{I-IV} are the points of impact when the planetary disc is tangential to the stellar disc. Figure taken from Winn [2010]

aspects of the geometry and timing of exoplanet transits relevant to this study.

1.3.1 Transit Geometry

Through geometry alone, we can construct a simplified picture of an exoplanet transit. We consider a planet of mass M_p, radius R_p and orbital semi-major axis a, transiting a star of mass M_* and radius R_*, as shown in Figure 1.3. We use an X-Y coordinate system centred on the stellar disc. As the planet transits the star, it travels along a chord across the stellar disc, blocking light from the star and causing a reduction in observed flux, as shown in the lower panel of Figure 1.3.

If the condition $R_* \ll a$ is satisfied, the planet's journey across the stellar

disc is largely a straight line along $Y = bR_*$ between $X = \pm R_* \sqrt{1 - b^2}$. The impact parameter b is the sky projected distance of the planet from the centre of the stellar disc at conjunction in units of the stellar radius, given for a transit by:

$$b = \frac{a \cos i}{R_*} \left(\frac{1 - e^2}{1 + e \sin \omega} \right). \tag{1.1}$$

Here e is the eccentricity of the planet's orbit, i is the orbital inclination and ω is the argument of periastron. The depth of a transit light curve, δ, is given, in the idealised case, by the ratio between the disk areas of the planet and the star, which simplifies to:

$$\delta = \frac{\Delta F}{F} = \left(\frac{R_p}{R_*} \right)^2, \tag{1.2}$$

where ΔF is the change in flux F from the star.

If the stellar radius can be determined (potentially through isochrone fitting [e.g. Bressan et al., 2012; Choi et al., 2016] or astroseismology [Chaplin & Miglio, 2013]), the planetary radius can be easily determined. This can be combined with a planetary mass determined from radial velocity observations in order to estimate the planet's bulk density. Equation 1.2 is only valid for a full (non-grazing) transit ($0 \leq |b| \leq 1 - (\frac{R_p}{R_*})$) as for a grazing transit ($1 - (\frac{R_p}{R_*}) \leq |b| \leq 1 + (\frac{R_p}{R_*})$), only part of the planet's disk is blocking light from the star, and determination of the planetary radius is more difficult.

In this idealised, geometric model, the bottom of a transit light curve is a constant function of time, however the variation of stellar luminosity over the disk can affect this. This can be due to the motion of spots, umbrae and plage over the stellar surface, or simply by non-uniform brightness in the limbs of a star (see Section 1.3.2).

1.3.2 Limb Darkening

The implicit assumption in equation 1.2 is that the stellar flux is constant across the diameter of the disk, however in reality the opacity and temperature of the plasma in a stellar atmosphere change with altitude. This leads to variation in flux across the stellar disk.

Photons escaping the plasma of a stellar interior do so at varying depths within a stellar atmosphere. As photons are absorbed in their journey through a stellar atmosphere, we can see further into the deeper regions of the star in its centre, and increasingly only light from the star's atmosphere towards its limbs. This means that the intensity of radiation changes across the stellar disk, varying the profile of

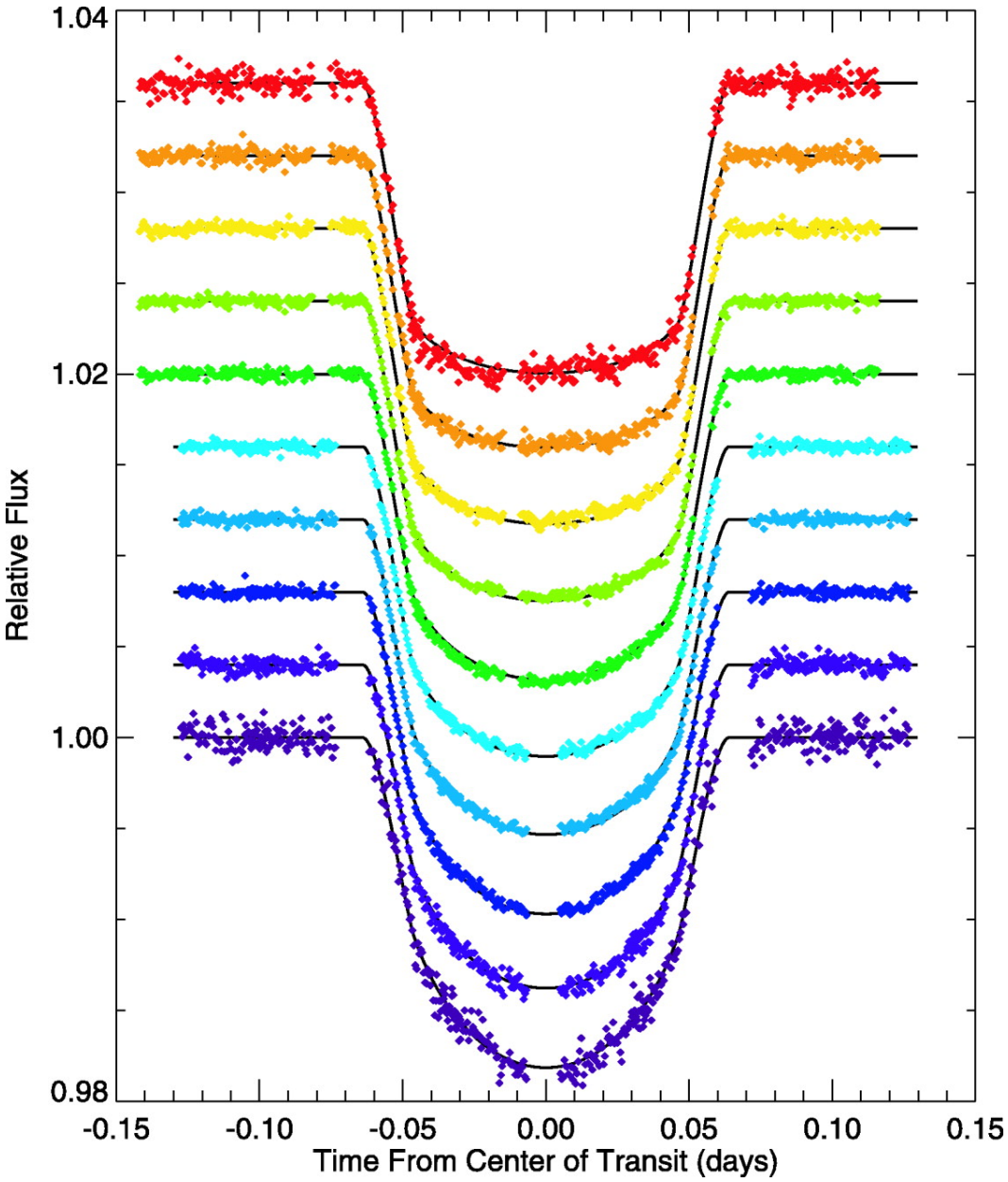


Figure 1.4: Illustration of the effects of limb darkening across the visible spectrum for a transit of HD209458b. Figure taken from Knutson et al. [2007].

an exoplanet transit.

The intensity of radiation escaping the photosphere is dependent on wavelength [Gray, 2022] meaning that limb darkening happens to varying degrees at different wavelengths, as shown in Figure 1.4. This is because the opacity of the plasma is dependent on temperature and therefore wavelength, meaning more photons from deeper layers within the star, a hotter region that more closely resembles a black body spectrum with more blue radiation, travel out to the observer. Consequently the effect of limb-darkening is more pronounced in bluer wavelengths than redder wavelengths.

Limb darkening is a complex effect which can only be measured in detail for our sun, and to calculate analytically would require detailed knowledge of opacity and emissivity at each layer in the stellar atmosphere. Approximations, known as *limb darkening laws*, can be used to model the effect of limb darkening using coefficients that can be fitted to a known light curve. These model the ratio of radiation intensity at the centre and limb of the disk. The simplest, and original, limb darkening law is the linear approximation [Russell, 1912]:

$$\frac{I_0}{I_\mu} = 1 - u(1-\mu). \tag{1.3}$$

A more complex law is the quadratic relation [Kopal, 1950]:

$$\frac{I_0}{I_\mu} = 1 - u_l(1-\mu) - \nu_l(1-\mu)^2. \tag{1.4}$$

Other relations, bringing in logarithmic, cubic and square root terms, give further description of the limb darkening effects. A full comparison of limb darkening effects and comparison of their fitting to light curves of exoplanet transits is given in Southworth [2008].

1.3.3 Transit Timing

In an ideal system, the time at which a planetary transit occurs can be predicted if the orbital period of the planet is known, as a planet on a purely Keplerian orbit will follow the ephemeris:

$$T_N = T_0 + NP \tag{1.5}$$

where T_N is the time of transit, T_0 is a reference transit time and N is the orbital epoch. Variations from a strictly Keplerian orbit can have several causes and will disrupt this periodic relation.

From Kepler's generalised third law, the semimajor axis of the planet's orbit a can be related to the orbital period by:

$$\frac{a^3}{P^2} = \frac{G(M_* + M_P)}{4\pi^2} \tag{1.6}$$

where G is Newton's gravitational constant. In most exoplanetary systems, $M_* \gg M_P$ and M_* can be determined to a reasonable accuracy through the star's spectral type, meaning that an observed orbital period can be converted into a semi-major axis [Haswell, 2010].

The geometry of a transit can be used to time different parts of the transit more precisely. As seen in Figure 1.3, there are four points where the stellar and planetary disks are tangential, labelled t_I to t_{IV}. The period $t_{II} - t_I$ is known as the transit *ingress*, and $t_{IV} - t_{III}$ the transit *egress*, with the total transit duration $T_{tot} = t_{IV} - t_I$ and the full transit duration $T_{full} = t_{III} - t_{II}$.

Assuming circular orbits, the duration of the transit can be found by [Murray & Correia, 2010; Winn, 2010]:

$$T_{tot} = \frac{P}{\pi} \sin^{-1}\left(\frac{R_*}{a} \frac{\sqrt{(1 + \frac{R_p}{R_*})^2 - b^2}}{\sin i} \right) \tag{1.7}$$

$$T_{full} = \frac{P}{\pi} \sin^{-1}\left(\frac{R_*}{a} \frac{\sqrt{(1 - \frac{R_p}{R_*})^2 - b^2}}{\sin i} \right) \tag{1.8}$$

for total and full transits respectively. These are the exact equations for the duration of a transit, however assuming $a \gg R_*$ (an assumption that may not hold for Hot Jupiter exoplanets) and low values of b, Haswell [2010] show that these equations can be approximated to:

$$T_{dur} \simeq \frac{PR_*}{\pi a}, \tag{1.9}$$

which can be thought of as a characteristic timescale of the transit [Winn, 2010]. Additionally, equations 1.7 and 1.8 hold only for a circular orbit; for a non-circular orbit the transit durations are [Winn, 2010]:

$$T_{tot} = \frac{P}{\pi} \sin^{-1}\left(\frac{R_*}{a} \frac{\sqrt{(1 + \frac{R_p}{R_*})^2 - b^2}}{\sin i} \right) \frac{\sqrt{1 - e^2}}{1 + e \sin \omega} \tag{1.10}$$

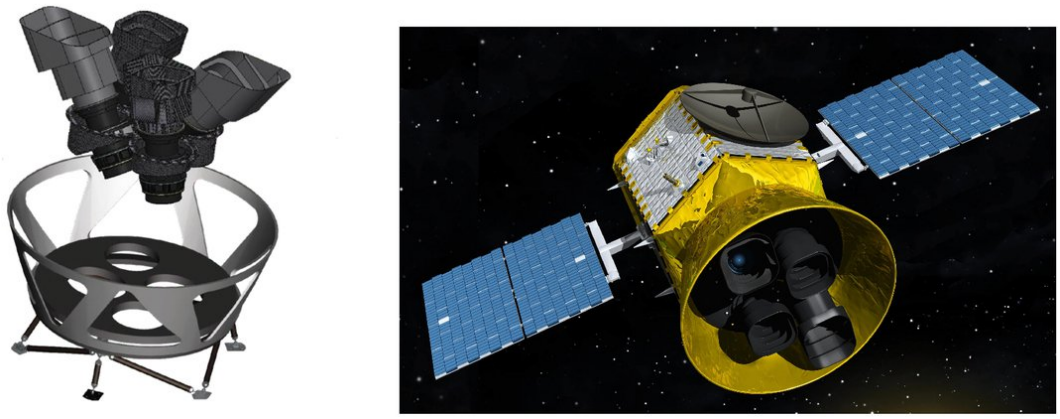


Figure 1.5: Left: Diagram showing the structure of the *TESS* spacecraft, with the four cameras and mounting platform visible. Right: Artist's impression of *TESS* in space. Figure taken from Ricker et al. [2015].

$$T_{full} = \frac{P}{\pi} \sin^{-1} \left(\frac{R_*}{a} \frac{\sqrt{(1 - \frac{R_p}{R_*})^2 - b^2}}{\sin i} \right) \frac{\sqrt{1 - e^2}}{1 + e \sin \omega} \tag{1.11}$$

where ω is the argument of periastron and e is the eccentricity.

For an unperturbed, stable planetary orbit, the time between successive transits will follow Equation 1.5 with strictly periodic transit times. However, other effects can influence the planet's orbit and affect this. These include apsidal precession and tidal orbital decay which will be explored in significant detail throughout this work, as well as the influence of perturbing companions on a planet's orbit.

Planets in multi-planet systems will, to varying degrees, follow non-Keplerian orbits due to gravitational interactions with other planets in the system. This can be used to discover and confirm non-transiting exoplanets [Holman & Murray, 2005; Holman et al., 2010; Ballard et al., 2011; Ford et al., 2012] as well as betraying the presence of exo-moons in a system [Kipping, 2009].

1.4 Exoplanet Transit Surveys

1.4.1 TESS

The Transiting Exoplanet Survey Satellite [*TESS*; Ricker et al., 2015] is a NASA Explorer-class mission dedicated to observing and characterising transiting exoplanets orbiting bright, nearby stars. *TESS* launched in April 2018 from Cape Canaveral Space Force station in Florida atop a SpaceX Falcon 9 rocket, before beginning science operations in July of that year. The technical details of this mission are laid

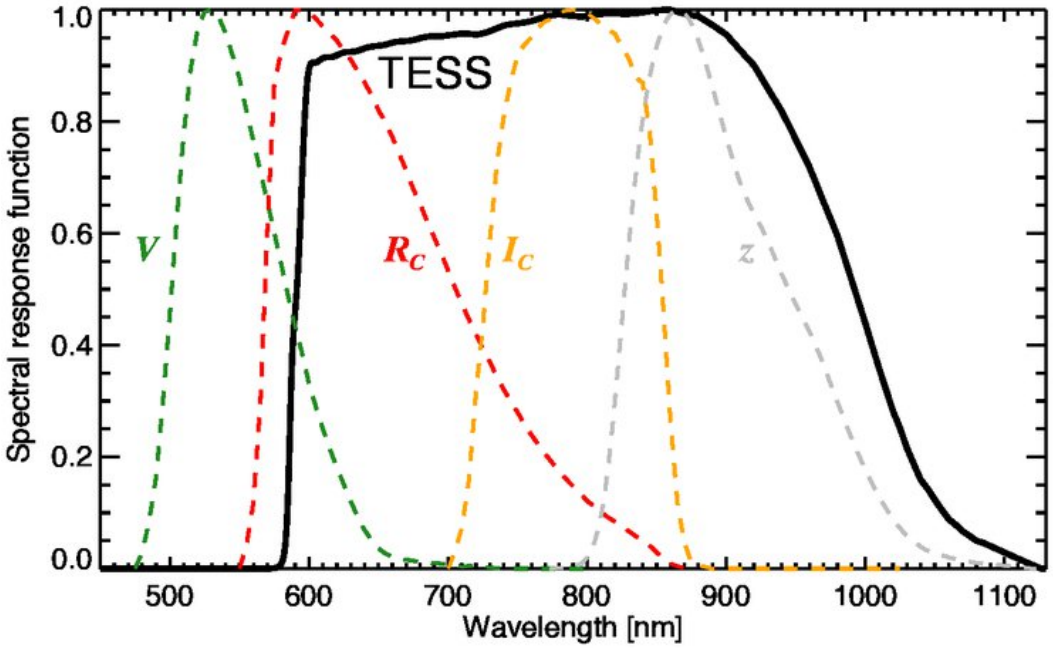


Figure 1.6: The bandpass of the *TESS* telescope system. The *TESS* bandpass is shown in black from 580 nm-1100 nm, and the Johnson-Cousins V, R_c and I_c and SDSS z bandpasses are shown for comparison, in dashed green, red, yellow and grey respectively. Figure taken from Ricker et al. [2015].

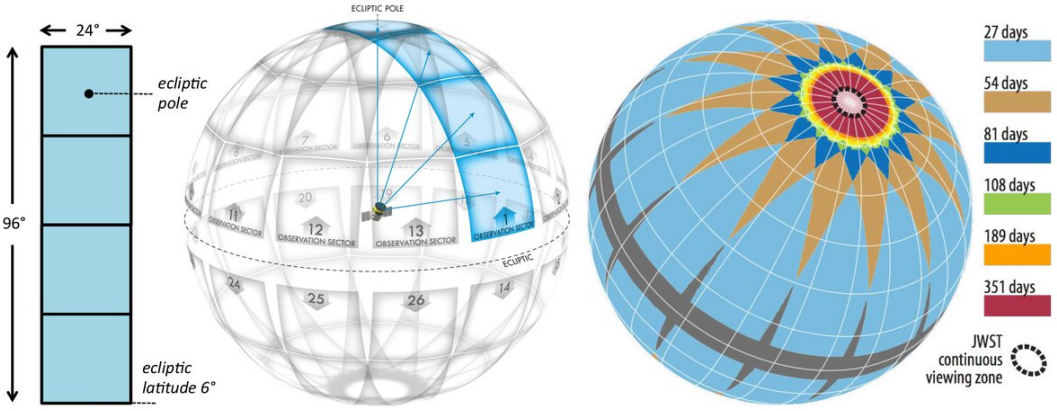


Figure 1.7: Idealised illustration of *TESS*'s initial (years 1 & 2) observing strategy. Left: field-of-view of the telescope with the combination of four cameras. Centre: Illustration of *TESS*'s 'tiling' strategy on the sky. Right: Sky coverage of *TESS* observations after the completion of the primary mission. Figure taken from Ricker et al. [2015].

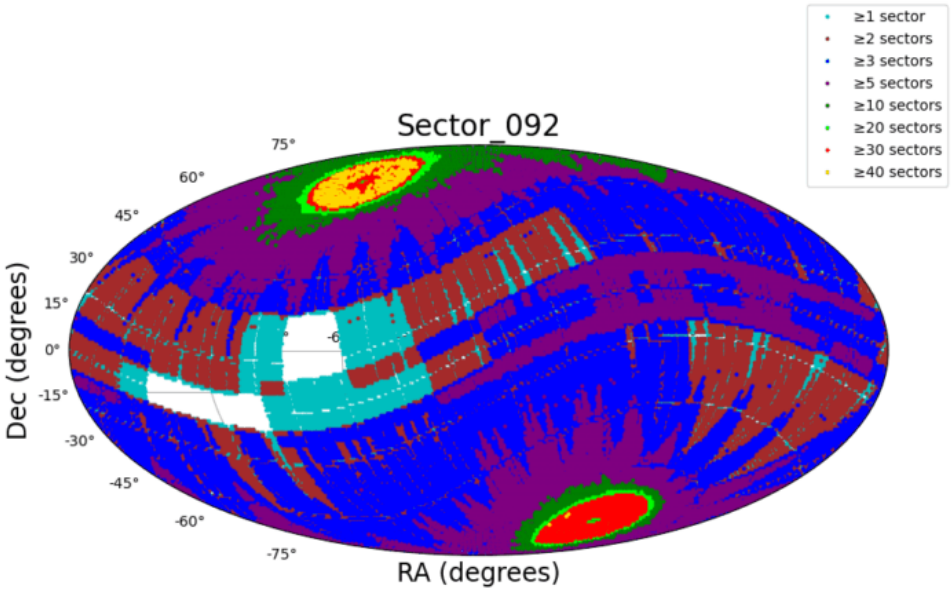


Figure 1.8: Illustration of the sky coverage and observation capacity of the *TESS* mission up to Sector 92 (May 2025), colour coded by the number of observations taken. Figure taken from `https://tess.mit.edu/observations/`.

out in detail in Ricker et al. [2015], and below I summarise the key details relevant to this thesis.

The *TESS* payload consists of four 10.5 cm, $f/1.4$ telescopes and a data handling unit (Figure 1.5). Each telescope has four back-illuminated Charge Couple Devices (CCDs), manufactured by MIT/Lincoln Laboratory and containing 2048 $\times$ 2048 pixels, of size 15 $\times$ 15 μm. Each lens has a 24°$\times$ 24° field-of-view and the telescopes are offset vertically, giving an effective field-of-view for the entire instrument of 24 °$\times$ 96 °. The *TESS* bandpass (580 nm-1100 nm, see Figure 1.6) has been optimised for maximum sensitivity to F5-M5 stars, and is comparable to the combination of the Johnson-Cousins R_c and I_c and SDSS z bandpasses.

TESS was launched into a high, elliptical orbit of earth, inclined away from the ecliptic plane, with perigee and apogee at 17 $R_\oplus$ and 59 $R_\oplus$ respectively. This results in a 13.7 day orbital period, placing it directly in a 2:1 resonance with the Moon. This orbital configuration was carefully chosen to minimise extended eclipses by, or periods of scattered light from, the Earth or the Moon, as well as remaining above the earth's radiation belts and being stable on a time scale of decades.

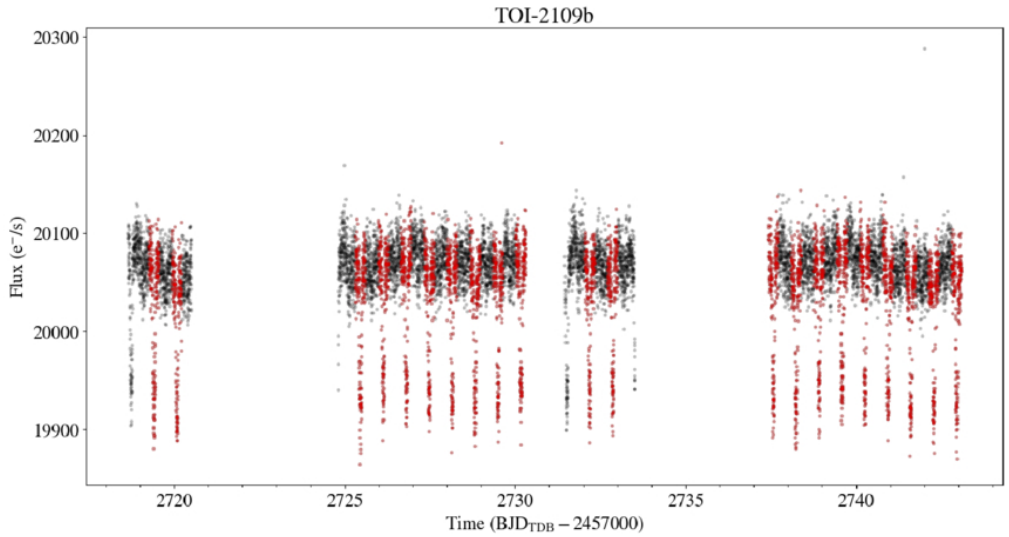


Figure 1.9: Example of a SPOC light curve from the *TESS* mission, for the ultra-short period exoplanet TOI-2109 b. This figure demonstrates the data gaps present in *TESS* light curves, due to downlink of data (central) and likely technical errors. The red highlighting shows transit events with enough data points to provide an accurate timing measurement. Figure taken from Alvarado-Montes et al. [2025].

TESS's initial observing strategy involves it taking observations of the entire sky over the course of two years, which it completed during its initial primary mission. As shown in Figure 1.7, the 24°× 96° field-of-view of *TESS* is used to tile a complete hemisphere of the sky over 13 'Sectors', each lasting for two full orbits of the spacecraft, meaning almost the entire sky can be observed over two years. Some areas of the sky are observed in multiple sectors, with the continuous viewing zones at the ecliptic poles providing near-continuous coverage when *TESS* is pointing in that hemisphere, and *TESS*'s visibility is limited near the ecliptic plane. In recent sectors, *TESS*'s observing strategy has changed from that used at the beginning of the mission and shown in Figure 1.7, to observing fields of view for a longer duration of four orbits and at a 40° roll angle, in order to extend coverage of mid-latitudes and the ecliptic plane[3]. The observational coverage of *TESS* up to Sector 92 is shown in Figure 1.8. The native observational cadence of the *TESS* CCDs is 2 s, however images taken at this cadence are co-added on board the spacecraft to produce the required data products - Target Pixel Files and Full Frame Images (FFIs) [Ricker et al., 2015]. FFIs were initially produced at 30 min cadence before being reduced in the extended mission to 10 min then 2 min

[3]Up-to-date information on the current observing strategy of *TESS* is available at `https://tess.mit.edu/observations/`

cadence. For the light curves, there are two main data processing pipelines. The Science Processing Operations Centre [SPOC; Jenkins et al., 2016] produces light curves at a 2 min cadence for ∼200,000 stars selected as the prime sample of stars for higher cadence observation, with the cadence reduced in later sectors to 20 s for some of the highest priority targets. Using mostly FFI data, the *TESS* Quick-Look Pipeline [QLP; Huang et al., 2020a,b] generates light curves of all stars contained in the *TESS* Input Catalogue [Stassun et al., 2018, 2019], in order to allow for easy identification of planetary candidates in previously un-studied systems. Data quality flags are associated with each *TESS* data point, flagging effects such as scattered light or cosmic rays, as well as more serious incidents such as the spacecraft entering 'Safe Mode', which allows for the user of the data to make selections based on the desired quality of their data. A full description of the *TESS* data products is available at `https://heasarc.gsfc.nasa.gov/docs/tess/data-products.html`, and an example SPOC light curve for a sector is shown in Figure 1.9 for the ultra-short period hot Jupiter system TOI-2109 [Alvarado-Montes et al., 2025]. In this figure the planet transits are clearly visible, with instrumental effects or scattered light seen in the baseline variations and data gaps due to technical errors or data downlinks visible.

All *TESS* data products are freely available to download from the Mikulski Archive for Space Telescopes (MAST)[4]. For as long as the *TESS* mission operates, contingent on further NASA support, it will continue to scan the sky and reveal the secrets of exoplanetary systems in our solar neighbourhood.

1.4.2 NGTS

The Next Generation Transit Survey [NGTS; Wheatley et al., 2018] is a ground-based exoplanet-hunting facility located at the European Southern Observatory's Cerro Paranal site in Chile and optimised for high precision photometry of exoplanet transits. Designed as a successor to the highly successful SuperWASP [Pollacco et al., 2006] project, NGTS was built in 2014/15 and gained first light in 2015, before starting science operations in 2017. Full details of the NGTS project are given in Wheatley et al. [2018], and below I summarise the key points relevant to this thesis.

The NGTS facility consists of an array of twelve 20 cm telescopes situated in a purpose-built enclosure at an altitude of 2440 m in the Atacama desert. Each camera is a modified Andor iKon L camera fitted with a 2048 × 2048 pixel back-illuminated CCD with 13.5 μm pixels. The NGTS photometric bandpass (520-890 nm, Fig-

[4] `https://mast.stsci.edu/`



Figure 1.10: The NGTS observatory in Chile. The twelve telescopes are shown taking flat field images during twilight. Figure taken from Wheatley et al. [2018].

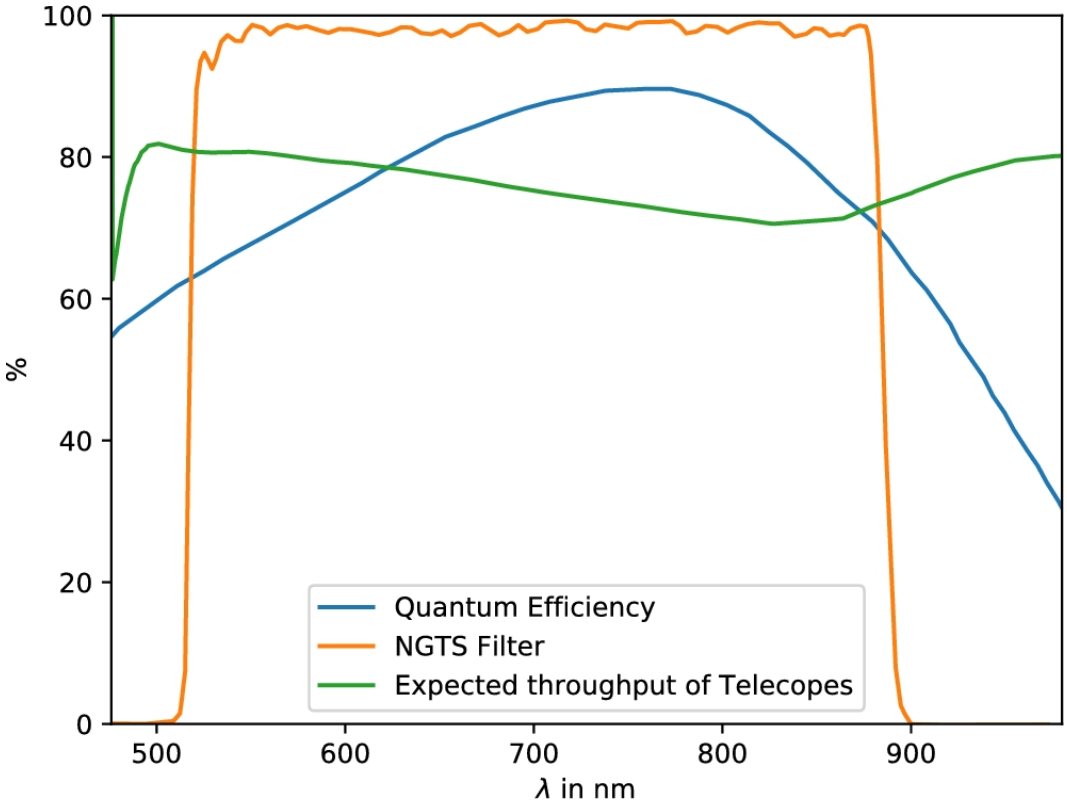


Figure 1.11: The NGTS photometric bandpass, showing the theoretical throughput of the detector (green), the quantum efficiency of the CCD (blue) and the measured throughput of the instrument (orange). Figure taken from Wheatley et al. [2018].

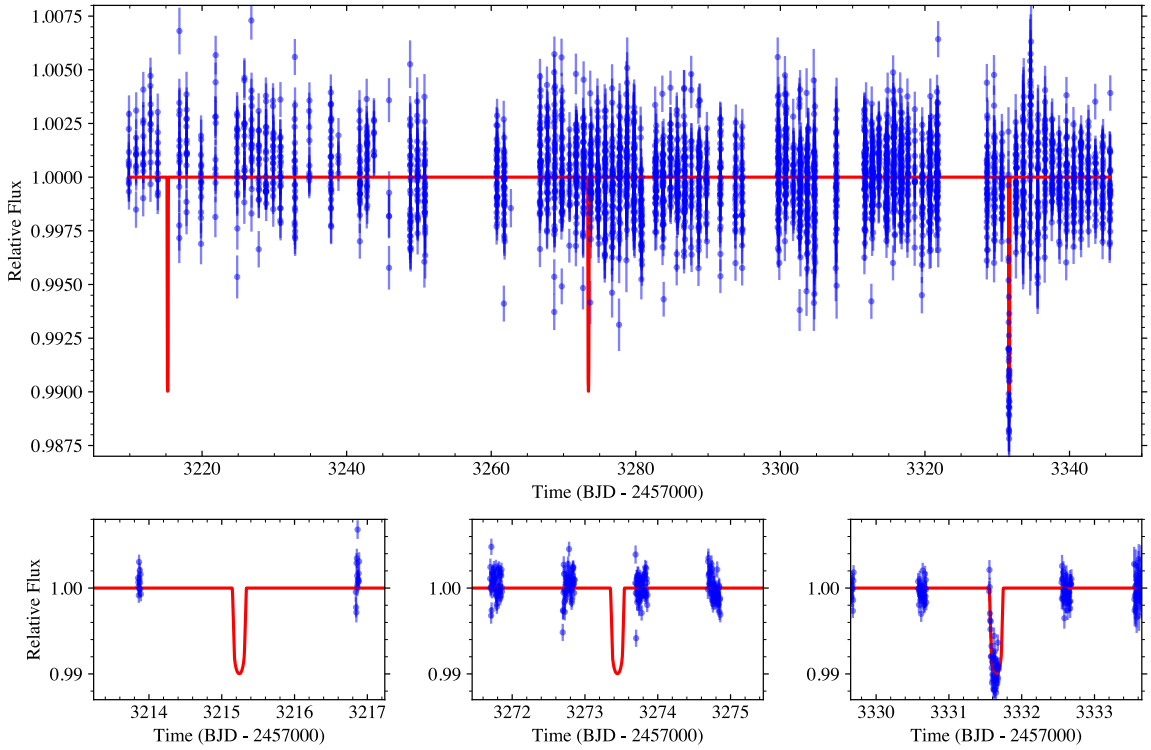


Figure 1.12: Example of a 150 day season of photometric monitoring by NGTS. The top figure shows the photometry resulting from a targeted monitoring campaign of the warm Jupiter host NGTS-39 [Apergis et al., 2026], with bottom panels showing a model light curve (red) with predicted transit events. Blue markers show the real NGTS photometry. Figure taken from Apergis et al. [2026].

ure 1.11) was specifically designed for this facility to maximise sensitivity to late K- and early M-dwarfs. The field-of-view of each telescope is 2.8°×2.8°and these combine to give a field-of-view of the facility of 96 $\deg^2$.

The NGTS facility uses high-precision autoguiding provided by the DONUTS algorithm [McCormac et al., 2013] which helps to achieve high-precision photometry through keeping stars on the same pixel, reducing read noise. In addition, the wide field-of-view of the telescopes means a large number of comparison stars are available for a given target and makes multi-telescope observations of bright stars effectively scintillation limited [O'Brien et al., 2022]. This, combined with the location of the facility at the Cerro Paranal Observatory, one of the best photometric observing sights on Earth, means NGTS is ideally positioned to perform high-precision photometric observations of exoplanet transit events.

The NGTS facility observes with 10 s exposures and a ∼3 s readout time, giving an effective observing cadence of around 13 s per observation. Targeted ob-

servations with NGTS are reduced using the Bright Star reduction pipeline [Bryant et al., 2020]. The observations are analysed using aperture photometry [Bertin & Arnouts, 1996; Barbary, 2016] with circular apertures to extract a given radius around the target star, and the radius selected to minimise the Root Mean Square (RMS) scatter of each observation. Comparison stars are observed for each observing field to correct for atmospheric and instrumental trends in the light curves, with the optimum comparison stars selected for each observation.

To date, the NGTS facility has contributed to the discovery of 66 new exoplanets [5]. Significant discoveries with NGTS involve NGTS-1 b [Bayliss et al., 2018], at the time the largest planet discovered transiting an M-dwarf star, NGTS-4 b [West et al., 2019], the first planet found in the 'Neptune Desert' (a known under-density of sub-Jupiter mass planets found in short orbital periods), NGTS-10 b [McCormac et al., 2020], at the time the shortest-period hot Jupiter discovered and NGTS-11 b [Gill et al., 2020], the first transiting planet discovered from a *TESS* single-transit event. Discoveries from this facility continue to push the parameter space of known exoplanets to longer orbital periods, such as the recent discovery of the warm-Jupiter exoplanet NGTS-38 b, with a 180 day orbital period [Rodel et al., 2026].

Outside of planet detection, the NGTS facility is used for a range of astronomical research, including the monitoring of stellar clusters [e.g. Gillen et al., 2020], study of eclipsing binary stars [e.g. Rodel et al., 2025; O'Brien et al., 2025] and the detection of stellar flares [e.g. Jackman et al., 2021], as well as targeted observations of known planetary systems in support of other facilities [e.g. Doyle et al., 2022; Barragán et al., 2026]. Targeted observations of this type can also be performed of known transiting systems in order to monitor the properties of these systems, and it is observations of this type that this thesis will focus on.

1.5 Tidal Effects in Planetary Systems

Tidal effects present in close-in planetary systems can have a dramatic effect on shaping their architecture and survival. In this section I will outline some of these effects, including an explanation of tide-induced orbital decay which will form the focus of this study.

1.5.1 Tides

In many studies of Newtonian gravity, the interactions between two bodies are approximated as being between two point masses, an approximation which holds when

[5] `www.ngtransits.org`

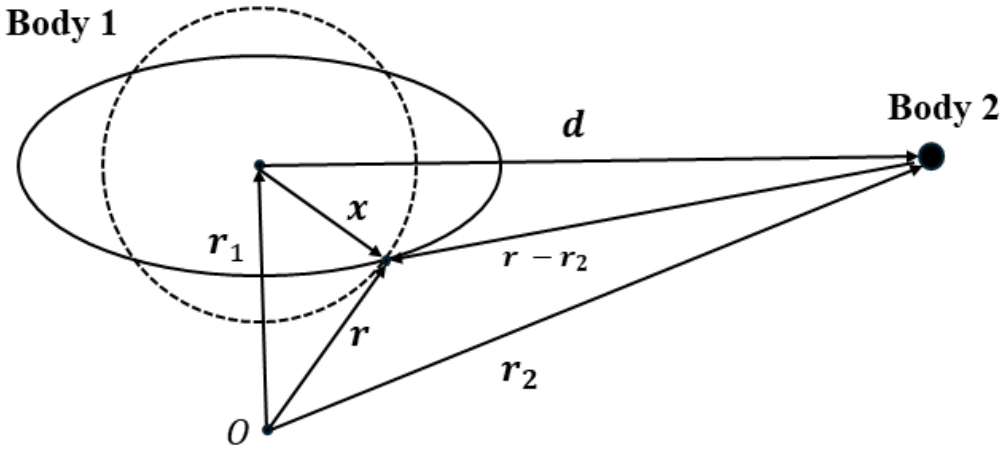


Figure 1.13: Illustration of the tidal forces between two bodies. Here the force of body 2, modelled as a point mass, on body 1 is displayed. Figure adapted from Barker [2025].

the distance between the bodies is much larger than their spatial extent. However, this approximation rapidly breaks down in the study of planetary systems with short orbital periods, and it is necessary to consider the differential gravitational force across an object. This arises from the inverse square dependence of the gravitational force with distance, which when an object has a finite size, means that the gravitational force varies across it. This results in tidal forces being present. In the following section, the reviews of Barker [2025] and Ogilvie [2014] are used to give an introduction to the theory of tides in short period planetary systems.

As displayed in Figure 1.13, we consider a body of mass M_1, unperturbed radius R_1 rotating around its spin axis at the rate Ω_s, which is perturbed by a body, modelled as a point mass, with mass M_2. This can be taken to represent a short period planet orbiting a star. The distance between the centres of the two bodies is given by $\boldsymbol{d}(t) = \boldsymbol{r}_2(t) - \boldsymbol{r}_1(t)$, where $\boldsymbol{r}_1$ and $\boldsymbol{r}_2$ are the position vectors of each body with respect to an arbitrary origin O. We define a point on the surface of body 1 with position vector between this point and the centre of body 1 $\boldsymbol{x} = \boldsymbol{r} - \boldsymbol{r}_1$.

Assuming $|\boldsymbol{x}| \ll |\boldsymbol{d}|$, the Taylor expansion of the gravitational potential due to body 2 is:

$$\Phi(\boldsymbol{x}, t) = -\frac{GM_2}{|\boldsymbol{d}|}\left(1 + \frac{\boldsymbol{d}\cdot\boldsymbol{x}}{|\boldsymbol{d}|^2} + \frac{3(\boldsymbol{d}\cdot\boldsymbol{x})^2 - |\boldsymbol{x}|^2|\boldsymbol{d}|^2}{2|\boldsymbol{d}|^4}| + O\left(\frac{|\boldsymbol{x}|^3}{|\boldsymbol{d}|^3}\right)\right) \tag{1.12}$$

The first term in this equation has no distance dependence so does not provide any contribution to the gravitational force ($\boldsymbol{F} = -m\nabla\Phi$). The second term is the

standard Newtonian force, present when treating both objects as point masses, that provides the orbital motion. The third and further terms contribute to differential forces across the body and are referred to as the tidal potential.

We consider the case of a circular, aligned orbit ($e = i = 0$, $|\boldsymbol{d}| = a$) and non-synchronous rotation ($\Omega_s \neq \Omega_0$), where

$$\Omega_0 = \sqrt{G(M_1 + M_2)/a^3} = 2\pi/P \tag{1.13}$$

is the orbital mean motion. Using spherical coordinates centred on body 1 and the standard spherical harmonics, the tidal potential Ψ can be expressed as:

$$\Psi(\boldsymbol{x}, t) = \frac{GM_2r^2}{a^3} Re\left[\sqrt{\frac{\pi}{5}} Y_2^0(\theta, \phi) - \sqrt{\frac{6\pi}{5}} Y_2^2(\theta, \phi) \mathrm{e}^{-2\mathrm{i}\Omega_0 t}\right]. \tag{1.14}$$

The circular and aligned orbit means that the only components of the potential are a static tide, term one in Equation 1.14, causing deformation of body 1, and an asynchronous component which causes fluid flow and time dependent deformation of body 1. This asynchronous component is the dominant cause of tidal dissipation mechanisms that lead to tidal orbital decay.

The amplitude factor in Equation 1.14 introduces a key factor for consideration in tidal evolution:

$$\frac{GM_2r^2}{a^3} = \epsilon_T \omega_d^2 r^2 \tag{1.15}$$

where

$$\omega_d = \sqrt{GM_1/R_1^3} = 2\pi/P_d \tag{1.16}$$

is the dynamical frequency of body 1. The term ϵ_T is known as the tidal amplitude:

$$\epsilon_T = \frac{M_2}{M_1}\left(\frac{R_1}{a}\right)^3. \tag{1.17}$$

This is used as a measure of the ratio, at the surface of body 1, of the gravity of body 2 to the self-gravity of body 1. If $\epsilon_T \gtrsim 1$, this is approaching the Roche limit and we would expect that body 2 would be tidally destroyed. For the case of the hot Jupiter exoplanets of concern in this study, we would expect $\epsilon_T \sim 10^{-6}$, as calculated for a $3\,\mathrm{M_J}$ planet orbiting a $1\,\mathrm{M_\odot}$ star with radius $1\,\mathrm{R_\odot}$ at semi-major axis a=0.05 AU. This is largely in the realm of linear tidal analysis, from which the processes that lead to tidal decay are derived.

For an asynchronous orbit, when the planet's orbital angular velocity differs from that of the star, the tidal response can be approximated by the constant phase

lag model of Hut [1981]. This was first introduced by Darwin [1880][6], who's work largely focused on the Earth-moon system, and it can be applied to exoplanetary systems. As the star and planet orbit each other, tides are raised on each object by the other by the differential gravitational force across the object, causing deviation from an equilibrium shape. As the objects are rotating and this deformation is not instantaneous, the surface of the object will appear as it was a constant time τ ago. This results in a tidal 'bulge' forming on the surface of the object which leads to a net torque being present in the system. As a result, angular momentum can be exchanged between the orbit and the spin of these objects, with this transfer happening from the planet's orbit to the star's spin in the case that the planet spins faster than the star rotates. This results in tidal orbital decay (Section 1.5.5).

1.5.2 Tidal Evolution Overview

As described qualitatively by Penev [2026], there are four principal processes at play in the tidal evolution of an exoplanetary system. These are the synchronization of a planet's orbit with its spin (or pseudo-synchronization in the case of eccentric orbits), the circularization of a planet's orbit, the reduction of a planet's orbital period, and the spin-up of the star. The timescales for these processes are all necessarily far greater than the planet's orbit, an assumption required for planets to remain stable over the timescales needed for their observation.

Given that the planet's spin angular momentum is small relative to that of its orbit and the star's spin, the timescale for synchronization of the orbit will be the smallest. In addition, forces driving a planet's orbit to circularize involve tidal effects on the planet from the star rather than those from the star on the planet, as is the case for decay. As the self-gravity of a planet is significantly reduced compared to the star, the circularization of a planet's orbit is expected to occur on a shorter timescale than its decay.

Once the orbit is circularized, the only significant tidal forces present are those raised on the star, with exchange of angular momentum with the planet's orbit and energy dissipation within the star leading to stellar spin-up and tidal decay on similar timescales [Penev et al., 2018].

1.5.3 Tidal Quality Factor

The quantification of tidal effects in a planetary system is usually performed in terms of the tidal quality factor, Q, describing the distortion of a body due to tidal

[6]This is George Darwin – not to be confused with his father Charles Darwin, proponent of the theory of evolution.

forces [Goldreich & Soter, 1966]:

$$Q^{-1} = \frac{1}{2\pi E_0} \oint \left(-\frac{\mathrm{d}E}{\mathrm{d}t} \right) \mathrm{d}t, \tag{1.18}$$

where E_0 is the maximum energy stored in tidal distortion, and the integral is of the total dissipation over one tidal period. This is most often expressed in terms of the modified tidal quality factor Q', where

$$Q' = \frac{3Q}{2k_2}, \tag{1.19}$$

where k_2 is the second order tidal love number [Love, 1909].

The Q' parameter can, in principle be computed for any celestial body susceptible to deformation by tidal forces. In this study however, we focus on the tidal quality factors of the host stars of exoplanet systems, due to the above conclusion that stellar tides are the driving factor behind tidal decay.

Within this parameter is encapsulated many effects causing the dissipation of energy within a star. This includes equilibrium tides - large-scale, low-frequency responses of the star stemming directly from the response of the body that causes the forcing - and dynamical tides - resonant, wave-like components of the response.

The dynamical tide is primarily composed of two regimes, with convective zones in the star hosting inertial waves (IWs), and the radiative zones hosting Internal Gravity Waves (IGWs) or 'g'-modes, which propogate from the convective-radiative interface into the stellar core [Barker, 2020]. These dissipate energy through turbulent convection and wave-breaking in the stellar interior [Barker & Ogilvie, 2010] and of the two, IGWs contribute more strongly to tidal dissipation in hot Jupiter host systems [Barker, 2020].

1.5.4 Orbit circularization

As mentioned above, the tidal forces present on a planet at short orbital period can act to circularize its orbit. This has long been confirmed observationally, with large campaigns showing that giant planets with short orbital periods have eccentricities of zero or close to zero [Pont et al., 2011; Bonomo et al., 2017]. The timescale for this circularization to occur is given by [Rasio et al., 1996; Goldreich & Soter, 1966]:

$$\tau_e = \frac{4}{63} Q_p \left(\frac{a^3}{GM} \right)^{1/2} \left(\frac{m}{M} \right) \left(\frac{a}{R_p} \right)^5, \tag{1.20}$$

where M is the mass of the star, R_p and m are the radius and mass of the planet, a is the orbital semi-major axis, G is the Gravitational constant and Q_p is the tidal quality factor of the *planet*. Tidal dissipation within the planet in the case of these short period orbits is usually dominated by inertial waves within the convective region of the planet [Ogilvie & Lin, 2004]. Constraints on Q_p values can be found through observational studies of planet eccentricities, as performed by Bonomo et al. [2017] who found $10^5 \lesssim Q'_p \lesssim 10^9$ necessary to explain the eccentricity distribution of the planets in their sample.

1.5.5 Tidal Decay

Considering a planet on a circular, aligned, orbit, we can show that the orbital period is expected to reduce due to tidal dissipation. This derivation is taken from Barker [2025].

We consider a planet with mass M_p and a star with mass $M_\star$ on an asynchronous orbit, $\Omega_0 \neq \Omega_\star$. The total energy in the system (orbital and rotational), E, and its angular momentum, L, are given by:

$$E = \frac{-GM_\star M_p}{2a} + \frac{1}{2} I_\star \Omega_\star^2 \tag{1.21}$$

$$L = \frac{M_\star M_p}{M_\star + M_p} \sqrt{G(M_\star + M_p)a} + I_\star \Omega_\star, \tag{1.22}$$

where the star's moment of inertia $I_\star = r_g^2 M_\star R_\star^2$. Here we define

$$r_g = \frac{8\pi}{3M_\star R_\star^2} \int_0^{R_\star} \rho r^4 \mathrm{d}r \tag{1.23}$$

to be the *Radius of Gyration*, with $\rho(r)$ as the stellar density profile. The derivatives of E and L are given by:

$$\dot{E} = \frac{GM_\star M_p}{2a} \frac{\dot{a}}{a} + I_\star \Omega_\star \dot{\Omega}_\star \tag{1.24}$$

$$\dot{L} = \frac{M_\star M_p}{M_\star + M_p} \sqrt{G(M_\star + M_p)a} \frac{\dot{a}}{2a} + I_\star \dot{\Omega}_\star. \tag{1.25}$$

Neglecting effects such as magnetic braking and mass loss and defining the tidal dissipation rate $D \equiv -\dot{E}$, Equations 1.24 and 1.25 can be rearranged under the assumption of conservation of angular momentum ($\dot{L} = 0$), by equating the $I_1 \Omega_s$

terms, to form an expression for $\dot{a}/a$:

$$\frac{\dot{a}}{a} = -2D\frac{M_\star + M_p}{M_\star M_p}\frac{1}{\Omega_0 a^2}\frac{1}{\Omega_0 - \Omega_\star}. \tag{1.26}$$

This shows that through tidal dissipation, the semi-major axis of body 2's orbit can be changed. The direction of this change is dependent on the factor $\Omega_0 - \Omega_\star$, the difference between the orbital mean motion of body 2 and the angular rotation of body 1. It can be seen that if $\Omega_0 > \Omega_\star$ (i.e. the planet orbits faster than the star rotates), $\dot{a}/a < 0$ and the orbit decays. This can be understood in terms of the constant time-lag model of Hut [1981] explained in Section 1.5.1 through the planet leading the tidal bulge on the stellar surface. This creates a net torque on the system which reduces the planet's orbital energy through tidal dissipation within the star. Consequently, through conservation of angular momentum, the planet's semi-major axis and therefore orbital period must reduce.

The D term in Equation 1.26 can be related to the Q' factor in Equation 1.18, meaning that the rate of change of semi-major axis can be used to quantify the rates of tidal dissipation within the star. In this case we focus on $Q'_\star$, the modified tidal quality factor of the host star in the system. An expression for this in terms of observable quantities of the system is given in Yee et al. [2020] through the formalism of Goldreich & Soter [1966]:

$$\frac{\mathrm{d}P}{\mathrm{d}t} = -\frac{27\pi}{2Q'_\star}\frac{M_p}{M_\star}\left(\frac{R_\star}{a}\right)^5, \tag{1.27}$$

where $\frac{\mathrm{d}P}{\mathrm{d}t}$ is the rate of change of orbital period, $M_P/M_\star$ is the mass ratio between the planet and the star and $a/R_\star$ is the orbital semi-major axis scaled to the stellar radius.

Through observations of planetary transits taken over a long baseline, reductions in orbital period due to tidal dissipation may be detectable. With the first observations of exoplanet transits now over two decades ago, an observational study of this type is possible. The decrease in orbital period would present as a quadratic ephemeris, in contrast to the linear ephemeris of Equation 1.5, which would take the form:

$$T_N = T_0 + NP + \frac{1}{2}\frac{\mathrm{d}P}{\mathrm{d}N}N^2, \tag{1.28}$$

which relates the changing orbital period to the orbital epoch N. This can be related

to Equation 1.27 through the relation:

$$\frac{\mathrm{d}P}{\mathrm{d}t} = \frac{1}{P}\frac{\mathrm{d}P}{\mathrm{d}N}, \tag{1.29}$$

through which the ephemeris trend can be converted to a changing period.

A key target of studies of this type has been the ultra-short period hot Jupiter WASP-12 b [Hebb et al., 2009]. At the time of discovery, the orbital period of this planet (1.09 days) was the shortest of any known planet and it also had the highest equilibrium temperature out of the known planets [Hebb et al., 2009]. Early transit timing studies revealed a hint of a non-linear ephemeris [Maciejewski et al., 2016; Patra et al., 2017], with the study of Yee et al. [2020] providing a definitive detection of orbital decay in this system. This study required the ruling out of alternative sources of these ephemeris trends which will be discussed in Section 1.6. Despite the effort of many analyses on large and small samples of ultra-short period systems [e.g. Patra et al., 2020; Vissapragada et al., 2022; Ivshina & Winn, 2022; Adams et al., 2024], no further definitive detections of orbital decay have been found.

Even if no orbital decay can be confirmed, limits on the possible decay rates can allow for limits to be placed on the tidal quality factors of the host stars ($Q'_\star$). Although reported uncertainties on these are often large, meaning an order-of-magnitude estimate is often the best possible result, this can still help constrain the tidal dissipation properties inside a star. Barker [2020] perform a detailed modelling of tidal mechanisms within stars known to host a short period exoplanet, and provide estimates of $Q'_\star$ values in these cases. Comparison of observed $Q'_\star$ values against these theoretical predictions will allow for refinement of theoretical models and insight into the strength of IGW dissipation within the stars. Barker [2020] also provide provide predictions for the existence of wave-breaking mechanisms [Barker & Ogilvie, 2010] in stars where IGW dissipation is present. Refinement of an observed tidal quality factor will help to determine the presence of these mechanisms as they increase dissipation efficiency.

Tidal dissipation can also be studied in the case of close binary systems, where the circularization timescale gives an estimate of the strength of these processes in the star [e.g. Van Eylen et al., 2016]. Here similar physical effects are at play but act on both objects, making this a more complicated scenario for modelling. For example, the tidal circularization times calculated for binary systems by Barker [2022] only considered tides in the primary star of the system. In the case of short period planetary systems, the tides raised by the star on the planet in its state of spin-orbit circularization are negligible [Penev, 2026], meaning that

the situation can be more accurately modelled in the case of hot Jupiter systems. This emphasises the importance of these systems in accurate determination of stellar tidal dissipation.

In this thesis I present new transit-timing observations of ultra-short period systems that are likely to be undergoing orbital decay, and will aim to determine if these systems are truly undergoing decay and if not, provide limits on $Q'_\star$ values that can be estimated from my results.

1.6 Orbital Decay False Positives

While the detection of a negative quadratic trend in the ephemeris of an ultra-short period planet can be suggestive of decay, there are other physical effects that can cause this and it is important to be aware of these in the interpretation of a timing trend. Notable physical effects described here are the Rømer (light travel-time) effect (Section 1.6.1), changes in stellar structure (the Applegate Mechanism; Section 1.6.2) and precession of an eccentric orbit (Section 1.6.3).

1.6.1 Rømer (Light Travel-Time) Effect

The discovery that the speed of light has a finite value was made by the Danish astronomer Ole Rømer in the late 17th century, through observations of the times of conjunction of Jupiter's moon Io [Roemer, 1677]. He estimated that light would take 11 minutes to travel from the Sun to Earth, making this the first calculation of the speed of light [van Helden, 1983]. The speed of light in a vacuum, as fixed by the International Bureau of Weights and Measures, is now known to be $299{,}792{,}458\,\mathrm{m\,s^{-1}}$.

The finite speed of light plays a role in precise timing of astrophysical events. The timing of pulsar signals [Edwards et al., 2006] and the eclipses of binary stars [Woltjer, 1922; Irwin, 1952] have long been documented to be affected by variations in distance of the event from an observer if a massive outer companion is pulling the system towards or away, due to the differing distances that light has to travel.

The same effect can be observed in ultra-short period exoplanetary systems. In this work we focus on observations of a large planet or brown dwarf on a close orbit with relation to its host star, however if this system has another massive outer companion (ranging from planetary to stellar mass), the perturbations of the inner system caused by this companion will cause variations in light-travel distance [Schneider, 2005]. If the system is moving towards us, the transit events will appear

to occur closer together, and the reverse is true if the line-of-sight motion is away from the observer.

The magnitude of the expected shift in transit time due to the Rømer effect (ΔT) can be given by [Schneider, 2005; Harre & Smith, 2023]:

$$\Delta T = 2\frac{M_B}{M_\star}\frac{a\sin i}{c}, \tag{1.30}$$

where M_B is the mass of the outer companion, $M_\star$ is the mass of the host star, c is the speed of light and a and i are the semi-major axis and inclination of the outer companion's orbit. If the outer companion's orbit is well known, this can be extended to calculate the magnitude of this effect over its entire orbit [Harre & Smith, 2023]:

$$\Delta T(t) = \Delta T_{max}\left(\frac{1}{2}\cos\left(2\pi\frac{t - T_{0,c}}{P_c}\right) + \frac{1}{2}\right), \tag{1.31}$$

where $T_{0,c}$ is the time of inferior conjunction of the outer companion, and P_c is its orbital period. This calculation requires significant prior knowledge of the orbital parameters of the companion, so providing more than wide constraints on timing variations is challenging. Likewise, constraints on the companion's behaviour could be calculated, however this would require confidence that the sinusoidal relation in Equation 1.31 had been sufficiently sampled.

Further information on a companion can be obtained through radial-velocity observations, due to the Rømer effect being directly analogous to the Doppler shift that occurs simultaneously in frequency space [Borkovits et al., 2015]. These measurements have proved crucial in confirming the presence of orbital decay over the Rømer effect in the WASP-12 system [Yee et al., 2020], and also provided strong evidence for the presence of an outer orbiting companion causing observed TTVs in WASP-4b [Bouma et al., 2020; Winn & Stefánsson, 2025]. High-precision radial velocity observations taken at regular intervals (preferably from the same instrument to avoid the influence of a systematic instrumental offset) will be vital in constraining the influence of light-travel time effects on future candidates for orbital decay [Harre & Smith, 2023].

An additional future opportunity to constrain the presence of outer companions to hot Jupiter systems that could be causing TTVs through the Rømer effect will be through the upcoming *Gaia* Data Release 4 [DR4; Gaia Collaboration et al., 2016]. Through providing the astronomical community with 5.5 years of high-precision astrometry from the *Gaia* mission, this Data Release is predicted to lead to the discovery of thousands of new unseen companions, in the mass range of

high-mass planets to low mass stars, meaning this will be a valuable resource with which to search for outer companions to systems with ultra-short period planets [Lammers & Winn, 2026].

1.6.2 Applegate Mechanism

TTVs of a similar magnitude to those observed due to dynamics of a planet can also be caused by variations in stellar structure and activity. The Applegate Mechanism [Applegate, 1992] has been proposed as a process through which TTVs can be caused which may mimic the signal of tidal decay.

Proposed by Applegate [1992], the Applegate mechanism was originally used to explain observed variations in eclipse timing of binary stars where one is a low mass star with an outer convective envelope [e.g. Baptista et al., 2002; Borges et al., 2008]. This process occurs as a result of variations in the magnetic activity cycle of a star, which re-distribute angular momentum within the stars interior. This causes variations of the quadropole moment of the host star which, through resulting variations in the gravitational field, is coupled to the orbital period of the system, causing variations in observed eclipse times. Applegate [1992] quantify these variations in orbital period through the relation:

$$\frac{\Delta P}{P} = -9\left(\frac{R}{a}\right)^2 \frac{\Delta Q}{MR^2}, \tag{1.32}$$

where $\frac{\Delta P}{P}$ is the fractional change in orbital period, R and M are the active star's radius and mass, a is the orbital semi-major axis and ΔQ is the change in the quadrupole moment.

Watson & Marsh [2010] extended this description of the Applegate mechanism to the study of exoplanet systems, proposing that the same mechanism is applicable due to most known exoplanet-hosting systems (at the time) containing early-main sequence, relatively low mass stars with convective outer layers. They calculated the predicted modulation in transit times caused by this effect for different lengths of activity cycles, including for several of the systems within this study. They found expected modulations of the order of $\sim$10 s, comparable in timescale to those observed through tidal decay. Watson & Marsh [2010] note the possibility that this mechanism can either mimic or mask the presence of tidal decay in a system, therefore observations of the stellar activity cycles of these stars are essential for distinguishing the true presence of tidal decay.

1.6.3 Apsidal Precession

The previous two sections have concerned process which, while inducing observed TTVs, still involve systems for which the planet is in a Keplerian-orbit. However, if the planet's orbit is slightly eccentric, the precession of the orbital major axis can induce non-Keplerian motion which manifests as TTVs that can mimic decay.

Although, as described in Section 1.5.4, a planet with an ultra-short orbital period is expected to orbit with zero eccentricity due to tidal interactions, the presence of an outer companion to the system can induce a small eccentricity through gravitational interaction as observed for WASP-19 [Bernabò et al., 2024]. From this, the argument of periastron ω will precess due a combination of three contributions, from general relativity, tidal interactions and rotation:

$$\frac{\mathrm{d}\omega}{\mathrm{d}t} = \frac{\mathrm{d}\omega_{\mathrm{GR}}}{\mathrm{d}t} + \frac{\mathrm{d}\omega_{\mathrm{tide}}}{\mathrm{d}t} + \frac{\mathrm{d}\omega_{\mathrm{rot}}}{\mathrm{d}t}, \tag{1.33}$$

For the purposes of fitting timing data, the ephemeris trend in the presence of apsidal precession is of the form [Giménez & Bastero, 1995]:

$$T = T_0 + NP_s - \frac{eP_a}{\pi}\cos\omega(N), \tag{1.34}$$

where T is the calculated mid-transit time, T_0 is a reference transit, N is the epoch and e is the orbital eccentricity. $\omega(N)$ can be explicitly expressed as a function of the precession rate relating to a reference ω value:

$$\omega(N) = \omega_0 + \frac{\mathrm{d}\omega}{\mathrm{d}t}. \tag{1.35}$$

P_a is known as the anomalistic period and corresponds to the time between one pericentre passage and the next. This is related to the siderial (observed) period P_s, the time between successive transits by the relation:

$$P_a = \frac{P_s}{1 - \frac{1}{2\pi}\frac{\mathrm{d}\omega}{\mathrm{d}t}}, \tag{1.36}$$

and can be longer or shorter than P_s depending on the sign of precession. Similarly, the ephemeris trend for occultation timing measurements can be expressed as:

$$T_{\mathrm{occ}} = T_0 + P_s N + \frac{P_a}{2} + \frac{eP_a}{\pi}\cos\omega(N). \tag{1.37}$$

As the trend in Equation 1.34 is sinusoidal once the linear ephemeris has been subtracted, it is at risk of being mistaken for a quadratic ephemeris resulting

from tidal decay. Numerical calculations performed by Jackson et al. [2026] found no way of distinguishing between a decay or precession ephemeris when simulating a WASP-12 like dataset of transit observations. However, a key tool in distinguishing precession from decay lies in occultation timing measurements, due to eccentricity information that can be deduced from observing both sides of a planet's orbit. Mathematically, the change in sign on the cosine term in Equation 1.37 compared to in Equation 1.34, as found by the numerical simulations of Jackson et al. [2026], allows for a strong distinction between the two processes. In addition, the only unambiguously confirmed detection of tidal decay, in the WASP-12 system [Yee et al., 2020] was confirmed as decay rather than precession thanks to the inclusion of occultation-timing data from the *Spitzer* telescope.

The inclusion of occultation observations does present difficulties when relying on ground-based observations due to the high photometric precision required. In the case of the observations of WASP-12 [Yee et al., 2020], the depth of an occultation was $\sim$0.4% in *Spitzer's* Infra-Red waveband, compared to the $\sim$2% optical transit depth, a difference that would only be more stark with a wider-orbiting planet and for a planet with lower equilibrium temperature. This would correspond to an equivalent increase in timing uncertainty, meaning for these observations to be useful in distinguishing between a precession and decay model, extremely high precision photometry is required.

The detection of apsidal precession can still yield interesting physical parameters, due to insights the precession rate can give to the planetary Love number and hence its structure [Ragozzine & Wolf, 2009; Bernabò et al., 2025].

1.7 Timing Inhomogeneities

With the detection (or non-detection) of orbital decay (or other astrophysical effects that mimic it) dependent on precise timing measurements, it is vital that consistency in timing conventions are applied throughout datasets spanning multiple decades. In particular, the use of the $\mathrm{BJD_{TDB}}$ timing convention over any others is preferable, which involves the conversion of a recorded time to the correct reference frame and time standard [Eastman et al., 2010].

Variations in distance caused by the orbital motion of our Solar System have a real effect on timing measurements due to the finite speed of light and must be taken into account. For this reason, a time conversion to Barycentric Julian Date (BJD), a time referenced to the orbital barycentre of the solar system, is necessary, to avoid timing discrepancies of up to 8.3 minutes. The difference between BJD

and the Heliocentric Julian Date (HJD, referenced with respect to the sun) is less significant as the discrepancies are only $\lesssim$4 s, but still vital.

In addition, it is important to ensure the correct time standard is used. The definition of a day according to the mean solar day is the basis for Universal Time (UT1) however due to changes in the Earth's rotation, a more commonly used standard is Coordinated Universal Time (UTC), which is corrected to the run speed of atomic clocks but is corrected from differing from UT1 by more than 0.9 s through the addition or subtraction of leap-seconds[7]. The addition of a correction for relativistic effects resulting from the motion of an observed, referred to as the Einstein delay by Eastman et al. [2010], completes the corrections necessary to express time values in the Barycentric Dynamical Time (TDB) system, the optimal system for timing of astrophysical observations.

While most of these corrections are far too small to influence daily life for most people, the differences induced, which can be as large as $\sim$60 s if an incorrect time system is reported, are extremely significant when performing high-precision timing measurements in astrophysics. In the context of orbital decay observations, Adams et al. [2024] found multiple instances where inconsistencies in timing systems, when collating timing data from archival databases, materially influenced the interpretation of an ephemeris fit. Therefore, consistency and accuracy in converting and reporting timing systems is of paramount importance to high quality astrophysical timing.

1.8 Project Objectives

The observational baseline available for some ultra-short period exoplanet systems is now approaching 20 years. Transit timing analysis over this timescale should be able to place constraints on the changing orbital period of these systems, as has been demonstrated for WASP-12 b [Yee et al., 2020]. The NGTS facility, with its high-precision photometry, optimum observing conditions and wide field-of-view, is well placed for continuous monitoring of systems likely to be undergoing tidal decay.

For the past $\sim$7 yrs, the NGTS telescopes have been conducting the NGTS Orbital Decay Programme, monitoring known ultra short period ($P_{orb} \lesssim 2$ days) transiting hot Jupiter and brown dwarf systems for the purpose of detecting subtle decreases in their orbital period suggestive of tidal decay. In this thesis, I present the first results from this programme, which involves analysing the observational data

[7]Notification of this is published by the US Naval Observatory: `https://maia.usno.navy.mil/products/leap-second`

from NGTS through making precise transit timing measurements. I also perform the same analysis on publicly available from the *TESS* observatory and observations taken with the Danish 1.54 m telescope on La Silla, and collate archival transit timing data from the peer-reviewed literature. I derive precise ephemerides for the 15 systems in this programme and determine whether the ephemeris shows a quadratic trend suggestive of decay.

Chapter 2

The NGTS Orbital Decay Programme I: Monitoring of 15 Ultra-Short Period Transiting Hot Jupiter and Brown Dwarf Systems

This chapter is reproduced from a Paper submitted to the Monthly Notices of the Royal Astronomical Society (MNRAS) on 28th August 2026. I am the first author of this study. For a full author list and details of the contributions of co-authors, please see the declarations section of this thesis.

Paper Abstract

Monitoring transit timing variations in ultra-short period hot Jupiter and brown dwarf systems ($P_{orb} \lesssim 2$ days) is a powerful probe into the structure and energy dissipation properties of the host star through tidal interactions. We present the first results of the Next Generation Transit Survey (NGTS) Orbital Decay programme, a long-term monitoring campaign to measure transit timings of 15 ultra-short period systems. We use 85 NGTS transit observations collected between 2019 and 2026. Additionally, we use 45 new transit observations taken with the 1.54 m Danish telescope, transit observations from the *TESS* mission and archival transit times compiled from the literature. We derive updated orbital ephemerides and search

for evidence of long-term orbital period evolution. We find an apparent decrease in orbital period in the WASP-4 system of $\dot{P} = -5.3 \pm 0.3\,\mathrm{ms\,yr^{-1}}$, consistent with previous studies. We also find new signs of decreasing orbital periods in the WASP-43, WASP-103 and WASP-128 systems, with period shifts of $\dot{P} = -0.6 \pm 0.2\,\mathrm{ms\,yr^{-1}}$, $-3 \pm 1\,\mathrm{ms\,yr^{-1}}$ and $-28 \pm 8\,\mathrm{ms\,yr^{-1}}$ respectively. These signals may be due to tidal decay, or some combination of tidal decay, the light travel-time effect and apsidal precession. We also observe a positive quadratic trend in the NGTS-7 A system, suggestive of a light travel-time effect. Continued monitoring by NGTS and *TESS*, as well as future observations from *Gaia* and *PLATO*, will help confirm the nature of the period shifts we find in these systems.

2.1 Introduction

The detection of the first exoplanet orbiting a sun-like star [Mayor & Queloz, 1995] was revolutionary not only for expanding humanity's perspective and awareness of our place in the universe but also because the planet discovered did not have any known analogue in the Solar System. The 4.2 day orbital period of 51 Peg b is shorter than any body in our Solar System, and therefore this discovery introduced an entirely novel category of planet: hot Jupiters [e.g. Fortney et al., 2021]. Named for the largest planet in our Solar System due to their size and low density, as well as the high temperatures that come from being so close to their host stars, these giants accompany only $\sim$0.3 % of stars in our galaxy [Beleznay & Kunimoto, 2022, from large scale transit surveys]. However, due to favourable biases in detection methods, hot Jupiters have a strong footing among exoplanet discoveries with $\sim$10 % of confirmed planets falling into this category[1].

A subclass of these planets occupying the closest position relative to their stars ($P_{orb} \lesssim 2$ days), known as ultra-short period hot Jupiters, are particularly interesting for the dynamical effects occurring in these systems [e.g. Penev et al., 2018; Collier Cameron & Jardine, 2018; Allart et al., 2025] and form the basis for this study.

Even in the earliest days of the study of exoplanetary systems, these ultra-short period systems were thought not to be dynamically stable over long timescales [Rasio et al., 1996]. The extreme tidal forces resulting from these close orbits raise a fluid bulge on the stellar surface which, due to frictional forces within the star, lags the planetary position by an angle $\epsilon \simeq \frac{1}{2Q}$rad. Here, Q is the *tidal quality factor* of the star [Goldreich & Soter, 1966], quantifying the ratio of energy available in

[1]NASA exoplanet archive (`exoplanetarchive.ipac.caltech.edu`) accessed on 24/09/2025

the star to that dissipated by frictional losses during an orbital cycle. The resulting torque, arising from the misalignment of the bulge with respect to the line between the stellar and planetary centres, causes the dissipation of energy within the star and the transfer of angular momentum in the planet-star system, resulting in tidal decay of the planet [Hut, 1981] and spin-up of the host star [Brown et al., 2011; Penev et al., 2018]. At an extreme level, this leads to total engulfment of a planet by a star, as reportedly observed by the Zwicky Transient Facility [De et al., 2023; Lau et al., 2025].

The efficiency of these tidal energy dissipation mechanisms is encapsulated within the dimensionless parameter Q, the tidal quality factor, as expressed in Goldreich & Soter [1966]:

$$Q^{-1} = \frac{1}{2\pi E_0} \oint \left(-\frac{\mathrm{d}E}{\mathrm{d}t} \right) \mathrm{d}t, \tag{2.1}$$

where E_0 is the maximum energy stored in the tidal distortion of a body and $\frac{\mathrm{d}E}{\mathrm{d}t}$ is the rate of dissipation of this energy, which is integrated over a complete orbit of the body. This quantity is often expressed in the form of the *modified* tidal quality factor

$$Q'_\star = \frac{3Q_\star}{2k_2}, \tag{2.2}$$

where k_2 is the second order tidal Love number of the orbiting body, in order to take into account this body's rigidity [Love, 1909]. For cool, main-sequence stars, Penev et al. [2018] find values of $Q'_\star$ in the range $10^{5.0-7.5}$, derived from the spin periods of these stars. This $Q'_\star$ value can vary significantly through a star's lifetime as well as depending on its mass, rotation and the period and amplitude of tidal forces present [Barker, 2020].

Encapsulated within the parameter $Q'_\star$ are two principal forms of tidal response in a star: equilibrium tides – large scale, non-wavelike deformations caused by the low frequency response within the star from tidal forcing – and dynamical tides – wavelike components dissipated by viscosity within the star and the non-linear effects of wave-breaking [Barker, 2020]. Of the two, wavelike dynamical tides are expected to greatly dominate mechanisms within main sequence stars, however, as stars evolve off the main sequence, the contribution from equilibrium tides is expected to increase. This contributes to the increase in decay rates implied from lower occurrence rates of giant planets around evolved stars [Bryant & Van Eylen, 2025].

Dissipation mechanisms due to dynamical, wavelike effects vary through the structure of a star. Internal gravity wave (IGW) dissipation in radiative regions of stars is expected to be the dominant process in the case of main sequence stars,

with dissipation in convective zones through inertial waves negligible except for cases when $P_{\mathrm{rot},\star} < 2P_{\mathrm{orb}}$, a condition not expected to be satisfied for hot Jupiters around main sequence stars [Barker, 2020].

Through precise timing measurements taken over a timescale of several years, variations in the orbital period of a planet can be detected and the presence, or lack, of orbital decay in the system can be deduced. The formalism of Goldreich & Soter [1966] shows a relationship between decay rate ($\dot{P}$) and the modified stellar tidal quality factor:

$$\dot{P} = -\frac{27\pi}{2Q'_\star}\left(\frac{M_P}{M_\star}\right)\left(\frac{R_\star}{a}\right)^5, \tag{2.3}$$

where $M_\star$ and M_P are the stellar and planetary masses, a is the semi-major axis and $R_\star$ is the stellar radius [Yee et al., 2020]. This shows that an observed rate of orbital decay can constrain rates of tidal dissipation in planet-hosting stars as well as, through the Love number, providing insight into planetary internal structure.

Ultra-short period sub-stellar companions, through interactions with their host stars, can therefore provide a unique probe into energy dissipation mechanisms and the structure of stars along their evolution, which can be measured through analysis of their transit timing variations (TTVs).

The presence of tidal decay processes can also be implied through population-level analysis of hot Jupiter systems. For example, Hamer & Schlaufman [2019] found that hot Jupiter host stars are younger, as implied through their galactic velocity distributions, than stars without these companions. This result has however been recently disputed [Hu et al., 2026]. Additionally, recent occurrence rate studies of the hot Jupiter population have found a decreasing correlation of hot Jupiter occurrence with age, implying that these companions are greatly outlived by their host stars [Chen et al., 2023; Miyazaki & Masuda, 2023].

For a system with a constant orbital period, the ephemeris will follow a simple linear trend:

$$T = T_0 + NP, \tag{2.4}$$

where T is the observed mid-transit time, T_0 is the reference mid-transit time , N is the transit number (epoch) and P is the observed constant orbital period. This will give a constant gradient when the difference between the observed and calculated mid-transit time is plotted over time. If a linear model with non-zero gradient provides the best fit, this implies a constant orbital period, but that the ephemeris used in calculating these values needs a slight correction. In the case of

orbital decay, the ephemeris will follow a quadratic trend [Yee et al., 2020]:

$$T = T_0 + NP + \frac{1}{2}\frac{dP}{dN}N^2. \tag{2.5}$$

Here, $\frac{dP}{dN}$ is the observed rate of change of orbital decay with respect to orbital epoch, from which the orbital decay rate can be found through the relation:

$$\frac{dP}{dt} = \frac{1}{P}\frac{dP}{dN}. \tag{2.6}$$

However, the method of analysing TTVs in a system can produce false detections of decay as apparent changes in orbital period can in some cases be explained by light travel-time effects, apsidal precession or the Applegate mechanism. Light travel-time effects, known as the Rømer effect, occur due to differences in the travel time of light across a system from line-of-sight acceleration due to a massive outer orbiting companion [Bouma et al., 2020; Harre & Smith, 2023; Winn & Stefánsson, 2025], and can be verified using long-term radial velocity monitoring to determine the line-of-sight acceleration of a system. The effect of orbital decay can also be mimicked by apsidal precession of a slightly eccentric orbit [Jackson et al., 2026] or variations of the quadropole moment of the star by stellar activity [the Applegate Mechanism; Applegate, 1992; Watson & Marsh, 2010]. Decay can be distinguished from these effects through occultation timing measurements and long term stellar activity monitoring respectively.

So far, a robust detection of orbital decay has only been confirmed in the WASP-12 system [Maciejewski et al., 2016; Yee et al., 2020]. Extending this sample will provide further observational insight to tidal dissipation properties over a range of systems and in order to do this, it is necessary to conduct an intensive campaign of photometric observations of a star, so that any observed TTVs can be quantified and decay rates constrained.

In 2019 we began the Next Generation Transit Survey (NGTS) Orbital Decay programme to use the NGTS facility to observe a set of 15 likely orbital decay candidates (selected based on their visibility from the NGTS observatory and short orbital period, see Section 2.2) in a homogeneous manner. Our goal is to continue to monitor these systems with NGTS for an extended period of time, and in this work present our progress to date.

This paper is structured as follows. In Section 2.2 we give an overview of the target selection process of the planets and brown dwarfs at the subject of this study. We then provide details of the observational facilities and methods used in this work

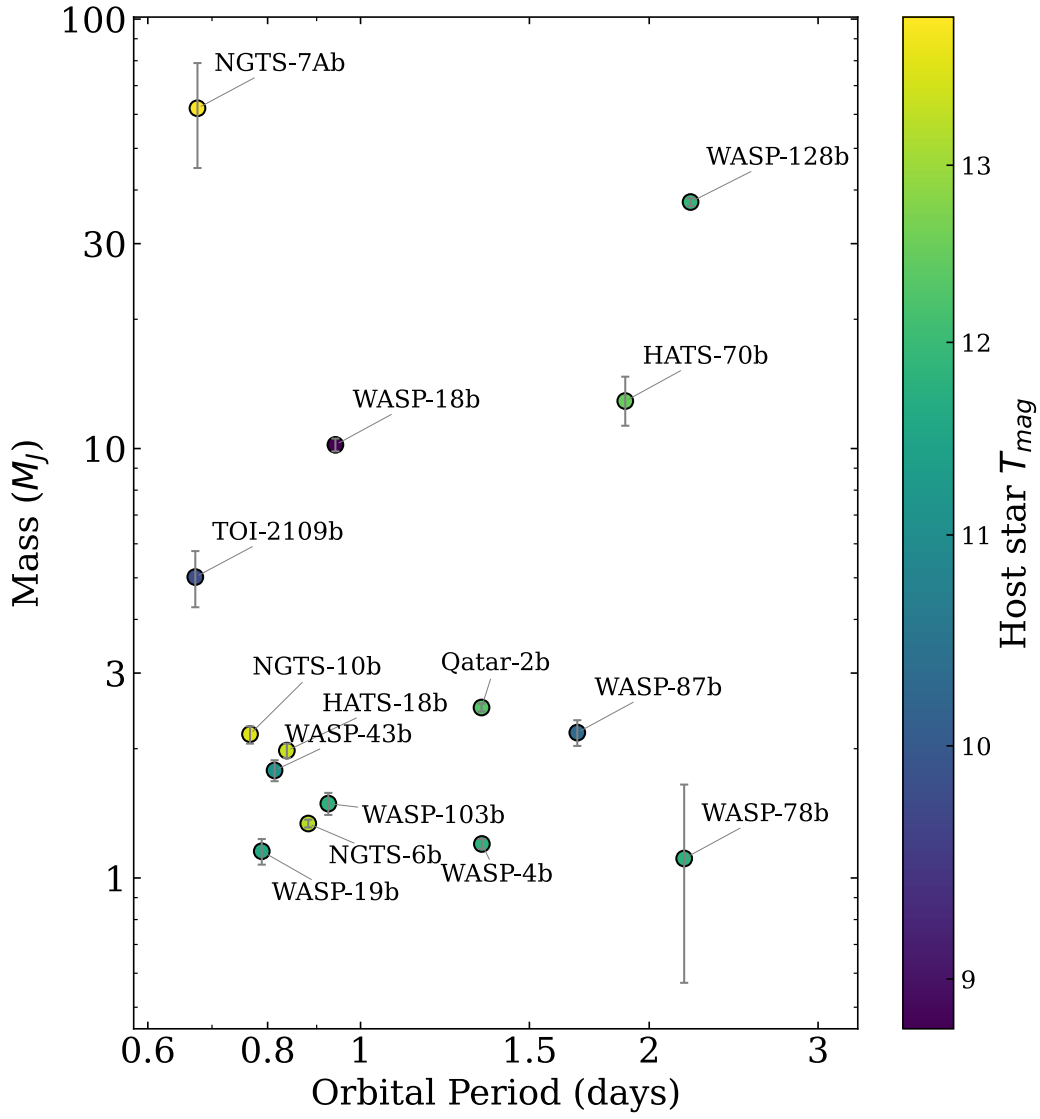


Figure 2.1: The masses and orbital periods for our sample of 15 hot Jupiters and brown dwarfs. The colour scale indicates the T-band magnitude of their host stars.

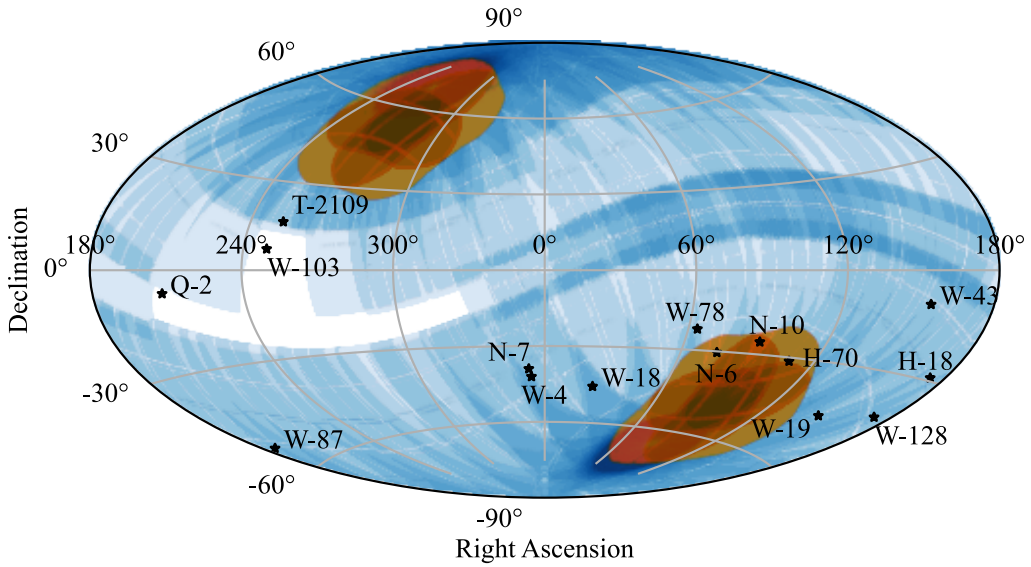


Figure 2.2: Sky position of the 15 targets in this study. The sky coverage of the *TESS* mission is shown in blue, with darker shades corresponding to more sectors of observation, and the *PLATO* LOPS2 and LOPN1 fields are shown in orange, with darker shades corresponding to more cameras observing [Eschen et al., 2024].

in Section 2.3, before describing the process we undertook in curating transit timing measurements from the scientific literature in Section 2.4. In Section 2.5 we describe our methods of reducing and analysing the observations we took in order to extract our precise transit times. The results of our analysis for each system are presented in Section 2.6, before we discuss their implications in Section 2.7 and end with conclusions in Section 2.8.

2.2 Sample Selection

We select a sample of orbital decay candidates from the set of confirmed transiting exoplanet and brown dwarf systems with planet masses $>1\,\mathrm{M_J}$ and orbital periods $\lesssim 2\,\mathrm{days}$. We only consider systems that can be well monitored from the Paranal Observatory in Chile – which we define to be targets where transits occur with airmass $z < 1.5$. We also require that the host star is bright enough for us to obtain high precision photometry with the NGTS facility, which in practice means stars with $T_{\mathrm{mag}} < 14$. Our sample contains 15 known ultra-short period hot Jupiter and brown dwarf systems. The masses, orbital periods and host star T-magnitudes of our sample are plotted in Figure 2.1 and their on-sky distribution is shown in

Figure 2.2. Full stellar and planetary parameter lists for these systems are given in Appendix 2.9 and Appendix 2.10, respectively.

2.3 Observations

2.3.1 NGTS Observations

The NGTS facility [Wheatley et al., 2018] is an array of twelve 20 cm telescopes located at the Paranal Observatory in Chile, optimised for the high photometric precision necessary for the detection of exoplanet transits. Each telescope is fitted with a deep-depletion back-illuminated 2048×2048 pixel CCD detector operating at a custom bandpass of 520 to 890 nm, allowing for increased sensitivity to late K and early M dwarf stars.

Tracking of target stars is performed using the high-precision DONUTS auto-guiding algorithm [McCormac et al., 2013], which minimises read noise on observations through high-stability star tracking. Combined with a large number of reference stars available due to the wide field-of-view of the telescopes (2.8°×2.8°per telescope), this makes observations of bright ($G_{\rm mag} \leq 11.5$) stars effectively scintillation-limited in noise [O'Brien et al., 2022].

In this project, transits are observed with NGTS telescopes in the NGTS bandpass using the standard 10 s exposure time which, combined with an average 3 s readout time, gives an effective cadence of 13 s between images. In most cases we use six NGTS telescopes per target to provide an increase in photometric precision compared with using just a single telescope [see e.g. Bryant et al., 2020; Smith et al., 2020b]. We observe at low airmass (z<2) and cover approximately an hour either side of the transit event in order to provide baseline for normalization.

Observational data are reduced using the standard NGTS Bright Stars reduction pipeline [Bryant et al., 2020], which uses a custom version of SEP (Source Extractor) aperture photometry [Bertin & Arnouts, 1996; Barbary, 2016] to extract photometry for a given radius around a star and subtracts a background flux level. For each night of observations, we selected an optimum target aperture (using the aperture with the lowest RMS flux over all telescopes) and a new master comparison star was selected based on that night's set of comparison stars. We perform a visual inspection of the raw photometry and sky background flux for each observation to check the data quality. In particular we use these checks to exclude cloudy data, data contaminated by the VLT laser guide star system, or data where there have been any telescope or detector problems. All timestamps for these NGTS lightcurves are generated in $\rm BJD_{TDB}$.

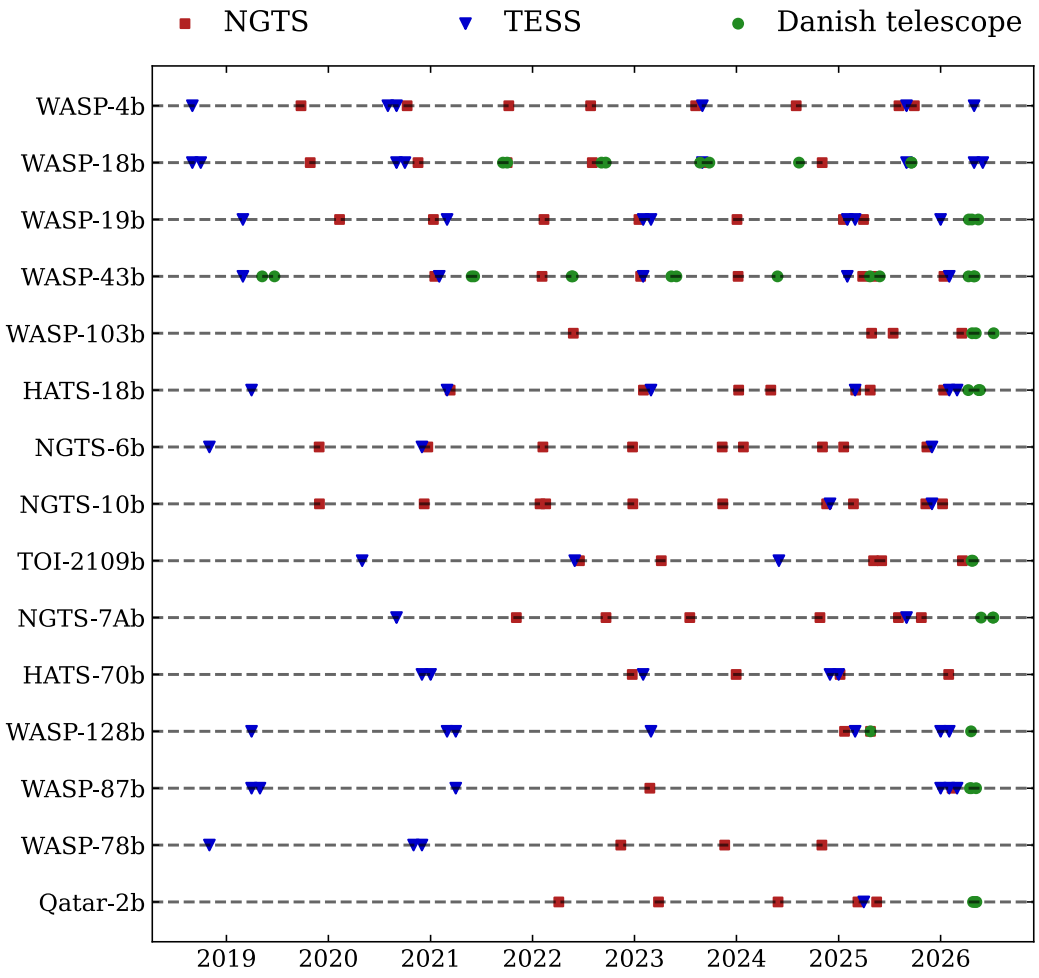


Figure 2.3: Timeline of NGTS (red squares), *TESS* (blue triangles) and Danish 1.54 m telescope (green circles) observations of our sample of 15 transiting hot Jupiters and brown dwarfs. One blue triangle represents an entire *TESS* sector of observations.

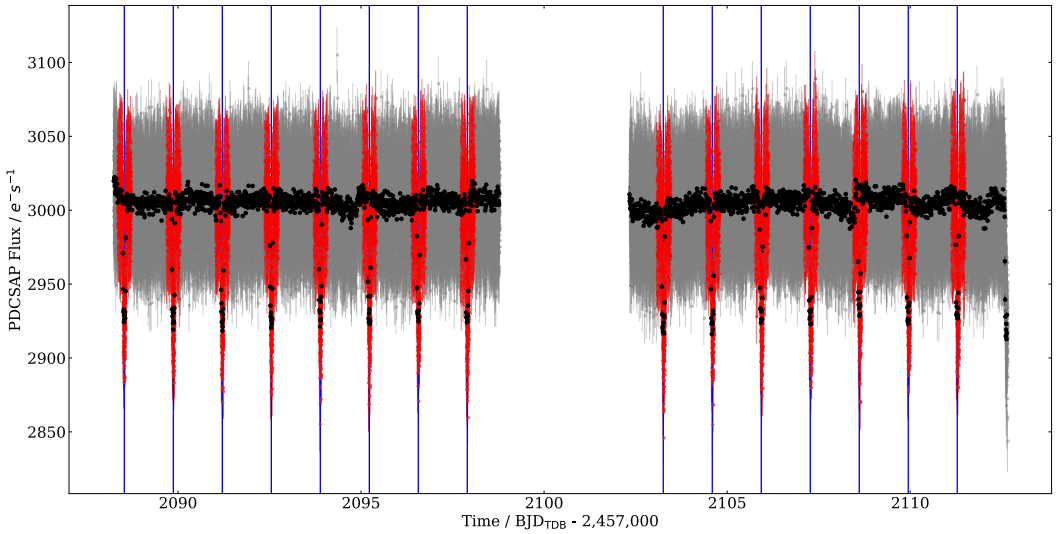


Figure 2.4: *TESS* PDC-SAP light curve of sector 29 observations of WASP-4, taken at 20 s cadence (grey points) and binned to 10 minute intervals (black points), showing the method used to extract the in-transit intervals. The blue vertical lines denote those predicted transit times with enough data present ($\geq$75% of the amount predicted given the cadence) for that transit to be used. Red points are the transit intervals used, spanning two transit durations either side of the predicted time.

To date we have monitored 85 transits of our sample of 15 targets over the course of 7 years. We summarise these observations individually in Table 2.6 and the timeline of observations used in this work is shown in Figure 2.3.

2.3.2 *TESS* Observations

The majority of the systems in our sample have been monitored by the Transiting Exoplanet Survey Satellite [*TESS*; Ricker et al., 2015]. Launched in 2018, *TESS* is a NASA mission dedicated to discovering exoplanets transiting bright stars through precise space-based photometric measurements of millions of stars in our stellar neighbourhood. The initial observing strategy of *TESS* involved a systematic survey across 13 sectors in each hemisphere, each with an area of 24°$\times$ 96°, taking a year to cover half of the sky. Each sector is observed for 27.4 days, corresponding to two orbits of the spacecraft in its 2:1 resonance with the period of the Moon. Apart from a 16 hr interruption at perigee to allow for downlink of data to Earth, *TESS* observes this field-of-view continuously.

TESS began science observations in July 2018, with the primary mission in the first two years (26 sectors) dedicated to a systematic scan of the southern sky followed by the northern sky. This monitoring has continued into the extended

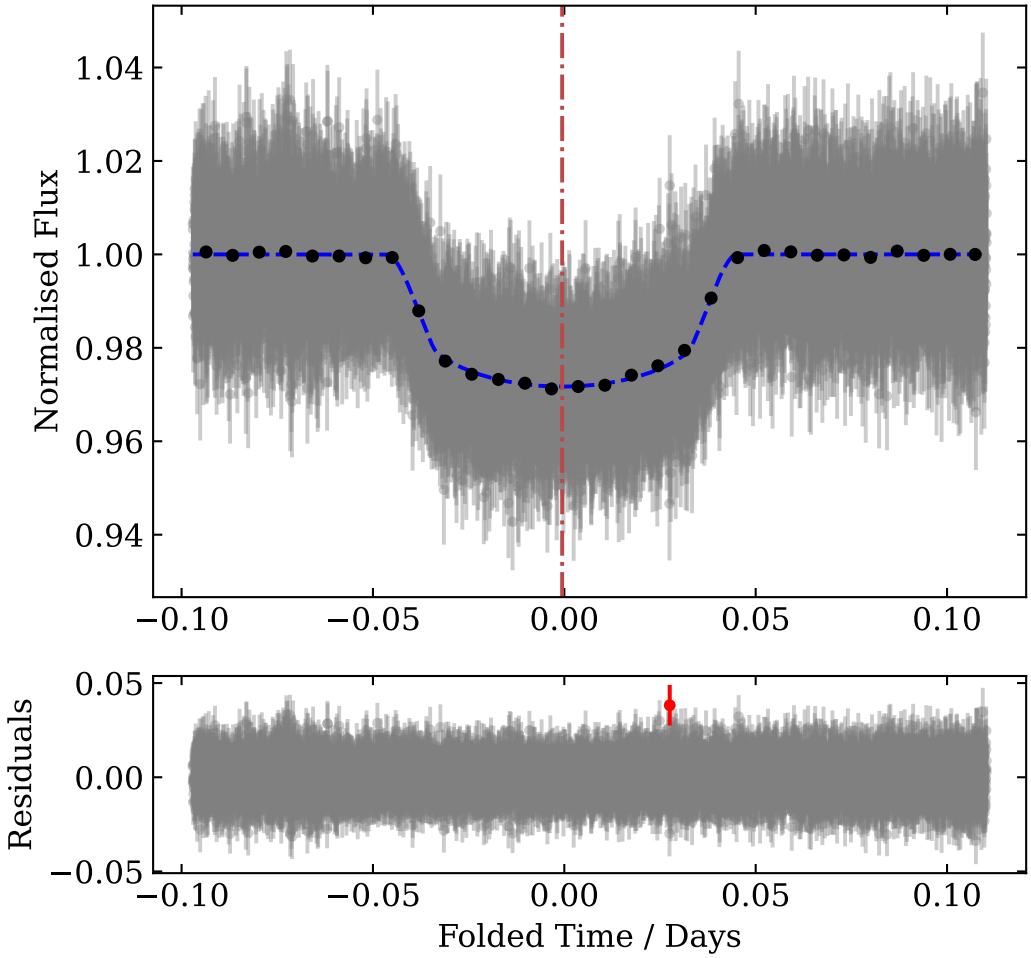


Figure 2.5: Stacked 6-telescope NGTS observation of the transit of WASP-4 on the night of 2023-08-08. This observation has been reduced and detrended according to the procedure in Section 2.5. The black dots are 10-minute time bins, and the blue dashed fit is the best-fitting Mandel & Agol [2002] transit model found through the procedure in Section 2.5.2, with residuals in the bottom plot and a 5σ outlier represented in red.

missions, allowing for repeated observations of many of these stars, a strategy vital for long term monitoring of transit timing.

The *TESS* data used in this study were those reduced by the SPOC (Science Processing Operations Centre) pipeline, in particular the PDCSAP_FLUX (Pre-search Data Conditioning Simple Aperture Photometry) data [Jenkins et al., 2016], which were downloaded from the NASA Mikulski Archive for Space Telescopes (MAST) portal[2]. These data products have been pre-treated to remove systematic features caused by instrumental signatures due to changes in focus or pointing, as well as some isolated outliers and radiation effects on the CCD detectors [Jenkins et al., 2016]. In this study we opted to only use flux data points with a data quality flag of zero.

To ensure we obtained the best precision on our transit timing measurements, we used the shortest cadence observations available for each sector of observations. For most targets, data are available at 2 minute cadence for earlier sectors, and this was shortened to a 20 s cadence for some targets in more recent observations. For some targets, the only data products available for earlier sectors were those at 30-minute cadence [Caldwell et al., 2020], and these were treated with extra care (see Section 2.5.2). If SPOC light curves were not available for 30 minute cadence observations, we used the TESS QLP [Quick Look Pipeline; Huang et al., 2020a,b] light curves, utilizing the KSPSAP_FLUX data product with the same data quality cuts.

As of July 2026, *TESS* has observed up to Sector 106, covering all tidal decay candidates in our study with the exception of WASP-103, and we include all observations of our targets that are available. These are listed in Table 2.9 and the timeline of observations is presented in Figure 2.3.

2.3.3 Danish Telescope Observations

We observed 45 transits of our targets using the 1.54 m Danish Telescope at ESO La Silla, Chile, as a side-project of the MiNDSTEp consortium [Dominik et al., 2010]. We used the Danish Faint Object Spectrograph and Camera (DFOSC), which is equipped with a 2048^2 px CCD camera with a $13.7'$ field-of-view sampled at $0.39''\,\mathrm{px}^{-1}$. The CCD was windowed to decrease the read-out time in all cases. Each transit was observed through either a Johnson V, Bessell R or Bessell I filter. The telescope was defocussed to improve the precision of the observations [Southworth et al., 2009].

[2] `https://mast.stsci.edu/`

The data were reduced using the DEFOT pipeline [Southworth et al., 2009, 2014]. Aperture photometry was performed using the IDL[3] implementation of the APER routine from DAOPHOT [Stetson, 1987] contained in the NASA ASTROLIB library[4]. The data were not debiassed or flat-fielded as the main effect of such calibrations was to increase the noise in the observations. A differential-magnitude light curve was generated for each transit observation versus a composite comparison star. The star weights and the coefficients of a low-order polynomial were optimised to minimise the scatter of the data outside transit.

The timestamp for each image refers to the midpoint of the exposure and was converted to the $\mathrm{BJD_{TDB}}$ timescale using routines from Eastman et al. [2010]. Manual time checks were performed for many transits to confirm the reliability of the timestamps in the FITS headers.

Observations taken with the Danish telescope are listed individually Table 2.8 and the timeline of observations is presented in Figure 2.3.

2.4 Literature Transit Times

In order to extend the timing baseline of our study, we combine our results with transit times available in the peer-reviewed literature. For some of the targets we study, archival observations now stretch back nearly 20 years, adding substantial weight to our analysis and meaning it is essential to interpret our results in the context of the cumulative transit timing literature.

As a starting point for our literature search, we used the database curated by Ivshina & Winn [2022]. These authors performed an extensive, semi-automated search of the transit timing literature pre-2022 and present their results in an accessible format, complete with data sources and time systems for each timing point. Given the scale of their study (382 planets were studied), some inaccuracies are inevitable, as reported by Adams et al. [2024], whose recommendations for the curation of archival timing points are discussed below.

We performed a detailed examination of the literature in which timing points, reported in the database curated by Ivshina & Winn [2022], were originally reported, as well as a manual search of the NASA Astrophysics Data System database[5] for more recently reported timing data for each system (post-2022). Having compiled literature transit times, it was then necessary to exercise judgement over the quality

[3] `https://www.ittvis.com/idl/`
[4] `http://idlastro.gsfc.nasa.gov/`
[5] `https://ui.adsabs.harvard.edu/`

of these data and their uncertainties and reporting. Where possible, we kept this selection homogenous and consistent, in accordance with the following principles:

1. We checked all times were reported as $\mathrm{BJD_{TDB}}$. Helpfully, the database provided by Ivshina & Winn [2022] ensures this, and the more recent results generally follow this convention.

2. Following Ivshina & Winn [2022], where timing uncertainties are reported as asymmetric, the larger error bar was adopted and the uncertainty assumed to be symmetric.

3. Following Ivshina & Winn [2022], we did not use timing points reported by the Exoplanet Transit Database (ETD) or other platforms that compile observations performed and analysed by both professional and amateur astronomers, as it can be difficult to ascertain the accuracy of the fitting method and uncertainties adopted. Instead, we only use transit times reported in the professional peer-reviewed literature. While analysing the timing data compiled by Ivshina & Winn [2022], we found a few instances when data from the ETD were reported in the literature and absorbed into subsequent studies, and for our analysis these have been removed.

4. We ensured that the transit fit in the published analysis included the mid-time T_c as a free parameter.

5. Following Adams et al. [2024], care was taken with the treatment of composite transit times (transit times derived from more than one transit light curve). Stacked transits, where a transit mid-time is derived from stacking photometry from multiple observational epochs on a fixed orbital period in order to detect a transit signal, were largely removed from our analysis. The exception to this rule came in the case of high precision ephemeris mid-times reported in the discovery paper for a planet. These often provide a crucial anchor to the timing fit at the earliest available epoch and are useful to include in the analysis. When an ephemeris mid-time is included in the analysis, care was taken to ensure no other timing points included in the fit were involved in the derivation of this timing point.

6. We identified cases where more than one mid-transit time was available for a given epoch, and examined the cause of this in detail. Where observations of a given epoch were taken by more than one observatory, these were taken to be independent measurements and therefore all included. Where a single

telescope observed a transit in multiple wavebands simultaneously, the measurements were combined and reported as the mean T_c value and error as the mean of the uncertainties on the individual measurements. If the same observation was analysed and reported by multiple groups, special care was taken in determining the most accurate reporting of these observations.

Table 2.1: Mid-transit times used in this work. Values taken from the literature are presented with their respective source(s), and those derived from NGTS or *TESS* data in this work are labelled as such. The orbital epoch is defined relative to the orbital ephemeris listed in Appendix 2.10. The full version of this table will be available in the online version of the published article, the first ten lines are presented here for information.

Target	Epoch	T_c (BJD_{TDB})	T_c error (days)	Source	Bibcodes
WASP-4	-1650	2454368.59279	0.00033	Ivshina & Winn [2022], Wilson et al. [2008]	2022ApJS..259...62I, 2008ApJ...675L.113W
WASP-4	-1629	2454396.69576	0.00012	Ivshina & Winn [2022], Gillon et al. [2009]	2022ApJS..259...62I, 2009A&A...496..259G
WASP-4	-1404	2454697.79821	0.00010	Ivshina & Winn [2022], Southworth et al. [2019]	2022ApJS..259...62I, 2019MNRAS.490.4230S
WASP-4	-1404	2454697.79817	0.00009	Ivshina & Winn [2022], Winn et al. [2009]	2022ApJS..259...62I, 2009AJ....137.3826W
WASP-4	-1401	2454701.81293	0.00011	Ivshina & Winn [2022], Southworth et al. [2019]	2022ApJS..259...62I, 2019MNRAS.490.4230S
WASP-4	-1401	2454701.81292	0.00020	Ivshina & Winn [2022], Hoyer et al. [2013]	2022ApJS..259...62I, 2013MNRAS.434...46H
WASP-4	-1398	2454705.82715	0.00029	Ivshina & Winn [2022], Hoyer et al. [2013]	2022ApJS..259...62I, 2013MNRAS.434...46H
WASP-4	-1381	2454728.57767	0.00042	Ivshina & Winn [2022], Hoyer et al. [2013]	2022ApJS..259...62I, 2013MNRAS.434...46H
WASP-4	-1378	2454732.59197	0.00050	Ivshina & Winn [2022], Hoyer et al. [2013]	2022ApJS..259...62I, 2013MNRAS.434...46H
WASP-4	-1378	2454732.59192	0.00017	Ivshina & Winn [2022], Southworth et al. [2019]	2022ApJS..259...62I, 2019MNRAS.490.4230S
...					

Using these principles we adopt a total of 538 transit timing measurements from the literature. These are presented, alongside the timing values from NGTS, *TESS* and the Danish 1.54 m telescope calculated in this work, in Table 2.1, and the respective citations are given in Appendix 2.12. For timing values from the literature we present the associated source and ADS bibcode to aid in future use of this database.

2.5 Data Analysis

In this section we describe the data analysis procedure for detrending our observational data, finding mid-transit times and fitting these to ephemeris models. In Sections 2.5.1 to 2.5.3 we describe the method used to analyse observational data from *TESS* and NGTS. This analysis was largely the same as that described for the extraction of mid-transit times from *TESS* data by Ivshina & Winn [2022], and we have adapted it as appropriate to be relevant for NGTS observations. In Section 2.5.4 we describe the data analysis and fitting procedure used for observations from the Danish 1.54 m telescope, before describing the procedure adopted to fit different ephemeris models to our derived mid-transit times in Section 2.5.5.

As a summary, in the case of NGTS and *TESS* observations, we perform polynomial baseline de-trending before fitting a Mandel & Agol [2002] transit shape model independently to each NGTS observation or stacked light curve of the *TESS* observations in a sector. We then perform a transit timing fit using an MCMC formalism in order to find the mid-transit time and its uncertainty. Observations from the Danish telescope were analysed differently, performing polynomial de-trending before fitting simultaneously for transit model parameters and the mid-transit time, with uncertainties scaled to give an overall reduced χ^2 value of unity. All timing points were then combined with those from the literature to perform a fit of the observed ephemeris.

2.5.1 Normalization and de-trending

To extract the in-transit data from observations, we calculated the predicted mid-transit time of each event using the published orbital ephemeris. The ephemerides used in the analysis of each of the systems in this study are listed in Section 2.10. These were taken, where available, from Ivshina & Winn [2022], or otherwise from the relevant planet discovery paper. Although the aim of this study is to find variations in the orbital period of these planets in relation to that published, using the published period at this stage was sufficient to find the times of transit.

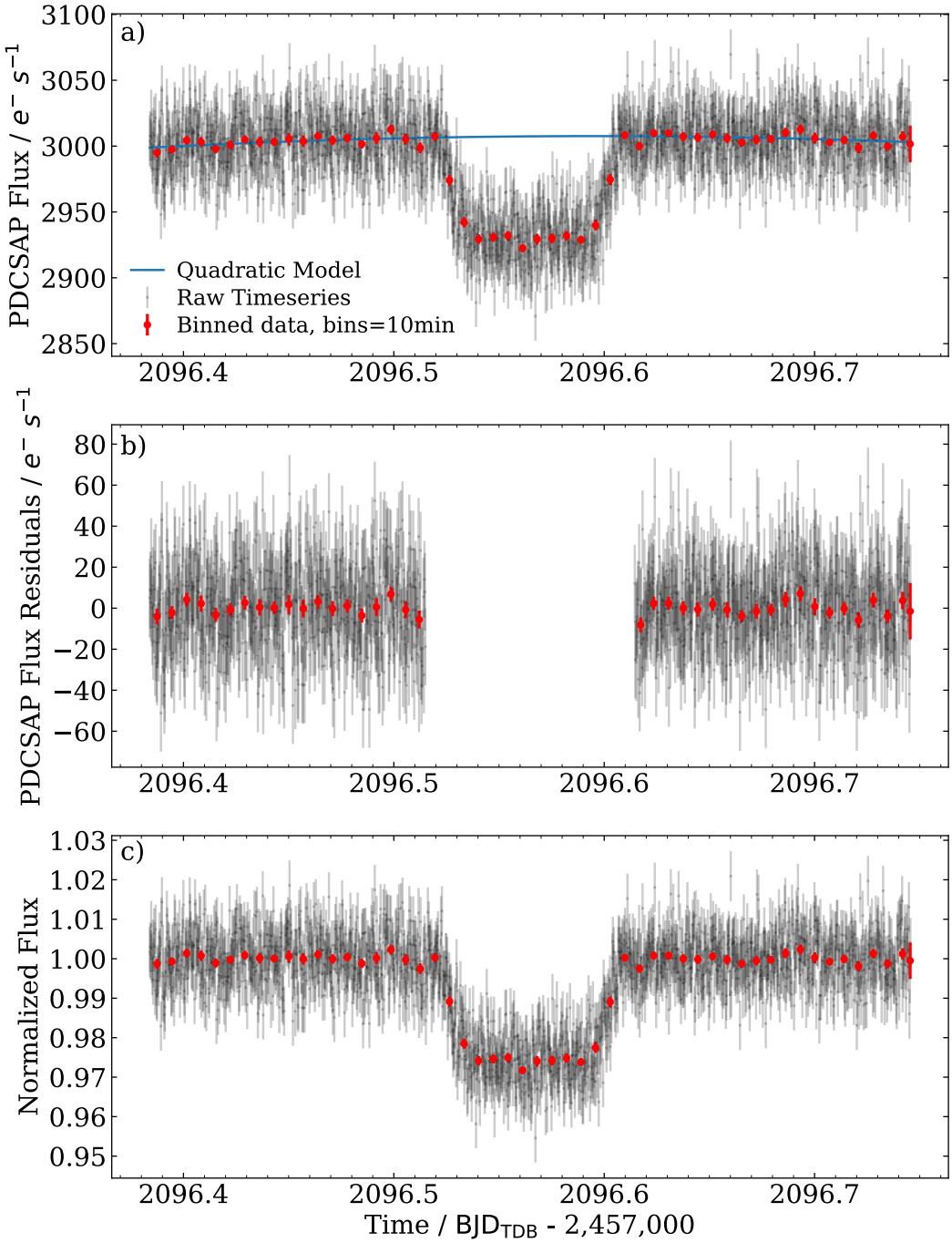


Figure 2.6: Illustration of the procedure to normalise and detrend *TESS* light curves, shown for WASP-4, sector 29, transit epoch 1883 taken at 20s cadence. a) Shows the PDC-SAP flux, with a quadratic polynomial fitted to the transit baseline (blue line). The residuals from this fit are shown in b) and the normalised light curve is shown in c).

For *TESS*, the data extracted spanned four full transit durations in total, giving an extended section of baseline with which to perform de-trending. Figure 2.4 shows an example of this transit data extraction process. For NGTS observations the process was similar, except all available baseline data points were used. Figure 2.5 shows an example NGTS light curve from this investigation.

Having recovered transit data points, we then normalized the light curve to remove photometric trends. We performed a visual inspection of the light curve to check for any instrumental effects, before extracting the out-of-transit baseline in each interval, using the published transit duration to select the in-transit data points, and centred this around the predicted midpoint. We extended this duration by 10% in our analysis to ensure no data points involved in the transit were included in this baseline from uncertainties in the transit duration or predicted midpoint. To this baseline, we fitted polynomials of order 1, 2 and 3 as a function of time and selected which to use by minimizing the Bayesian Information Criterion [BIC; Schwarz, 1978],

$$\mathrm{BIC} = \chi^2 + k \cdot \log(n), \tag{2.7}$$

which combines the χ^2 goodness-of-fit parameter with the number of free parameters k and the number of data points n. We then normalised each light curve by dividing by this polynomial. An example of this process is shown in Figure 2.6. This procedure was performed for both *TESS* and NGTS observations.

We adopted the same data quality check as Ivshina & Winn [2022] at this point by comparing the number of data points within each transit interval to the number predicted given the time interval and cadence. If there were less than 75% of the predicted value, this interval was removed from the analysis. This allowed automatic vetting of transits with significant contamination or gaps in time coverage. Additionally, we performed a visual inspection of the baseline fitting to ensure accuracy.

2.5.2 Transit Model Fitting

Following the normalisation of the light curve, we fit a transit model to quantify the shape of the transit event. For *TESS* observations, the normalized transit data for each sector were folded on the known value of the orbital period (Table 2.5) in order to fit this shape, whereas for NGTS data all observations for each night were stacked.

These stacked light curves were fitted with a Mandel & Agol [2002] transit model with quadratic limb darkening coefficients using the BATMAN transit fitting

code [Kreidberg, 2015]. This fit was performed by minimising the χ^2 value on the model parameters using a Nelder-Mead optimiser [Nelder & Mead, 1965] within the LMFIT Python package [Newville et al., 2016]. Within this fitting formalism, the values of R_p/R_*, a/R_* and the transit midpoint were allowed to vary, the eccentricity was fixed at zero, and when fitting the *TESS* light curves stacked over a whole sector, the orbital inclination and quadratic limb darkening parameters were kept as free parameters. In the case of NGTS light curves for only one night of observation, given degeneracies in these parameters and these only representing one transit event, values were taken from the literature for the planet's inclination and limb darkening parameters. This procedure was carried out separately for each *TESS* sector or NGTS observation night, with no link between the derived parameters.

Where limb darkening parameters were not available for the appropriate waveband in the literature, these were calculated using the PY-LDTK [Limb-Darkening ToolKit; Parviainen & Aigrain, 2015] which uses the stellar spectrum libraries of Husser et al. [2013]. Priors for the values used in the transit model fits and the stellar parameters for limb darkening coefficients were taken from the sources listed in Section 2.10.

For *TESS* light curves taken at 30-minute cadence, we used the 'supersample' parameter in BATMAN to fit the transit model. This returns the average value of the light curve taken over 9 evenly spaced samples within each 30-minute exposure in order to model the reduced resolution of these observations. Otherwise, the extraction of the timing values from these data was consistent with the rest of the *TESS* data.

To minimize outliers affecting the fit at this stage, we calculated the mean absolute deviation (MAD) of the residuals from this fit, and rejected any points lying more than 5 times this value away from the model fit. If points were rejected, we then re-performed the same fit, using the previous fit results as the initial conditions passed to the model.

2.5.3 Transit Time Fit

To find the mid-transit point of each transit in a *TESS* sector, we performed a fit with a Markov-Chain Monte Carlo (MCMC) method using the EMCEE Python code [Foreman-Mackey et al., 2013]. In this process we held constant the values of $R_p/R_\star$, $a/R_\star$, orbital inclination and the limb darkening parameters found through the least-squares fit outlined in Section 2.5.2 for that observation night (NGTS) or sector (*TESS*). This model was then applied separately to each transit in a *TESS* sector, or to the relevant NGTS observation, with the only free parameter being the

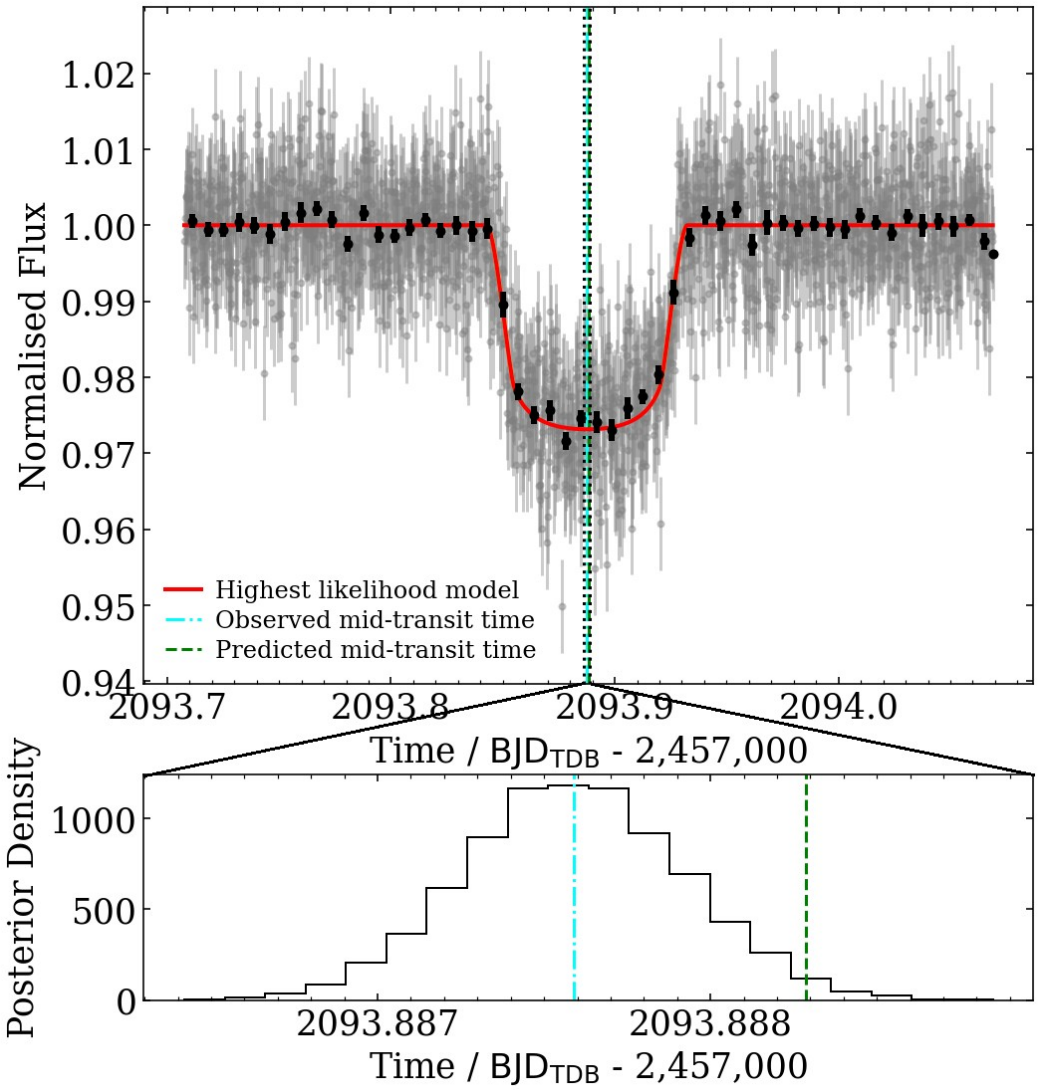


Figure 2.7: Illustration of the MCMC fitting process to extract precise mid-transit times as applied to WASP-4, sector 29, transit epoch 1881. The best fit model is shown in red in the top plot, and the posterior histogram showing the results of the MCMC fit is shown in the bottom plot. Black lines denote the relevant zoom region in which this histogram is located, and green dashed and dashed-dotted lines show the predicted and observed mid-transit times respectively. Grey points are the *TESS* data at 20 s cadence and black points are these binned to 10 min intervals.

mid transit point. This transit shape was different for each *TESS* sector and NGTS observation. An example of this fitting process is shown in Figure 2.7.

To perform the timing fit, we used 5 walkers with 10,000 iterations, with 500 used as a burn-in, and uniform priors on the mid-transit time of half a transit duration either side of the predicted transit time. In keeping with earlier stages of this analysis, we analysed the residuals of the observational data relative to this timing fit and clipped those which lay further than 5 times the MAD of the data away from the model. If any data points were clipped during the analysis of a transit, that fit was then re-run. The resulting mid-transit times and their uncertainties were then compared to those predicted using the linear ephemeris in Table 2.5 in order to calculate and plot the deviation of these planets' ephemerides from a constant model (Observed minus Calculated or O-C values).

As a final data quality check within the analysis of the *TESS* data used in this programme, we calculated the MAD of the O-C transit times relative to the mean O-C value within a sector, as well as the average size of the error bars on these times. The value of these two statistics should be similar if the scatter of the timing points within a *TESS* sector is insignificant. As part of this analysis, to remove any significantly anomalous values we removed timing points that lay more that five times the MAD from the mean in a sector, and those with error bars more than three times the average for that sector. These follow similar data selection criteria as those adopted by Naponiello [2026]. Additionally, for input into our ephemeris fitting and in keeping with the curation of literature timing values in Ivshina & Winn [2022], we took the uncertainty on the measured mid-transit time to be the larger of an asymmetric error bar.

2.5.4 Danish Telescope Fitting

Each transit light curve observed using the Danish telescope was modelled using the JKTEBOP code [Southworth et al., 2004; Southworth, 2013] in order to determine the transit midpoint, following our standard practise with this facility [e.g. Southworth et al., 2022]. We fitted for the sum and ratio of the fractional radii (where the fractional radii are the true radii divided by the semi-major axis of the relative orbit), the orbital inclination, and time of midpoint. These transit shape parameters are independent of those derived for *TESS* and NGTS observations. The transits were already de-trended as part of the data reduction process, but we included a polynomial versus time to ensure we captured the uncertainties incurred by this step. No de-trending was explicitly done against airmass, FWHM or detector position. We used the quadratic limb darkening law for the star, fitted for the linear coefficient,

and fixed the non-linear coefficient to theoretical values.

The uncertainties in the fitted parameters were calculated using Monte Carlo and residual-permutation simulations [Southworth, 2008]. Formal errors from the Fisher matrix were also calculated, after the data uncertainties had been scaled to give a reduced χ^2 of unity. For each transit, the largest of the three uncertainty value was adopted.

2.5.5 Ephemeris Fit

Once the O-C values have been calculated, we perform an MCMC fit using EMCEE to determine the preference for either a quadratic (Equation 2.5) or linear (Equation 2.4) ephemeris model. We first perform a least-squares fit of the O-C values in order to determine starting values, before using these in the MCMC fit. Wide uniform priors are given for this fit for both models, of ± 100 s relative to the T_0 value found with the least squares fit, and $\pm 100\times$ the linear and quadratic terms as applicable.

Table 2.2: Best-fit transit ephemerides for the 15 planets in this study. We present an updated linear ephemeris and the ΔBIC value used to determine the preference for a linear or quadratic ephemeris for each system. Where the quadratic ephemeris fit is preferred, we present the derived decay rate and $Q'_\star$ value assuming this apparent change in period is caused by tidal decay. Where a linear fit is preferred, we present upper (3σ) limits on the decay rate and the corresponding lower limit on $Q'_\star$. We do not present a $Q'_\star$ value for NGTS-7 A due to the positive quadratic trend.

System	Num Transits	Updated T_0 ($\mathrm{BJD_{TDB}}$)	Updated Period (days)	ΔBIC	Preferred model	Decay rate ($\mathrm{ms\,yr^{-1}}$)	$Q'_\star$ (derived)
WASP-4 b	201	2456576.675136±0.000033	1.338231244±0.000000025	345.51	Quad	-5.3 ± 0.3	$(6.9\pm0.6)\times10^5$
WASP-18 b	209	2453403.35991±0.00005	0.94145237±0.00000004	1.14	Lin	> -1.2	$>2.1\times10^7$
WASP-19 b	300	2456977.77659±0.00005	0.78883897±0.00000002	-4.71	Lin	>-0.8	$>3.8\times10^6$
WASP-43 b	261	2457423.44965±0.00005	0.81347409±0.00000003	6.45	Quad	-0.6 ± 0.2	$(2.2 \pm 0.7) \times 10^6$
WASP-103 b	83	2457511.94451±0.00008	0.9255453±0.0000001	6.90	Quad	-3 ± 1	$(1.9 \pm 0.7) \times 10^6$
HATS-18 b	200	2458217.64345±0.0002	0.837844±0.000002	-4.57	Lin	>-8	$>4.4\times10^5$
NGTS-6 b	113	2457982.3793±0.0030	0.88206±0.00008	2.35	Lin	>-35	$>2.4\times10^4$
NGTS-10 b	90	2457518.84460±0.00023	0.7668933±0.0000030	-3.54	Lin	>-12	$>1.9\times10^5$
TOI-2109 b	126	2459378.45907±0.00007	0.6724742±0.0000003	-4.33	Lin	0.9±1.3	$>2.4\times10^7$
NGTS-7 A b	103	2457708.5533±0.0002	0.67599148±0.00000008	52.72	Quad	$+15 \pm 2$	-
HATS-70 b	70	2459202.3104±0.0013	1.8882395±0.0000031	-4.23	Lin	>-75	$>9.9\times10^4$
WASP-128 b	74	2456720.6841±0.0002	2.2088254±0.0000005	7.86	Quad	-28 ± 8	$(1.1 \pm 0.3) \times 10^5$
WASP-87 b	79	2458571.3499±0.0002	1.6827942±0.0000004	-4.37	Lin	>-9	$>3.3\times10^5$
WASP-78 b	37	2458440.3766±0.0022	2.175185±0.000004	-2.24	Lin	>-54	3.5×10^4
Qatar-2 b	84	2456030.7505±0.0002	1.337117±0.000001	-2.51	Lin	>-3.1	$>1.1\times10^5$

The MCMC fit is performed using 10,000 iterations and 10 walkers, with 500 discarded as burn in. After we perform the fit once, we find the difference between the best-fit linear ephemeris and the input linear ephemeris and re-run using our new model, thereby providing an ephemeris update for the community for each system. These are presented in Table 2.2.

From the fit of each model, we calculate the value of the BIC for each model. The difference in the BIC value is calculated by:

$$\Delta\mathrm{BIC} = \mathrm{BIC}_{lin} - \mathrm{BIC}_{quad} \tag{2.8}$$

with a positive value of ΔBIC suggesting a preference for a quadratic fit. We take a ΔBIC value of +10 to be sufficient evidence to claim a definitive preference for a quadratic ephemeris in our results, and +5 as the suggestion that a quadratic fit may be preferred. In Table 2.2 we list the calculated orbital decay rate and $Q'_\star$ value, calculated using Equation 2.3, for our systems. Where no preference for a quadratic trend is found, these are presented as the 3σ lower limits on these values in order to place constraints on tidal dissipation in systems with a linear ephemeris.

2.6 Results

In this section we set out the results for each of the 15 systems in our sample, focusing on whether the transit timing measurements fit best to a quadratic function (Equation 2.5, which could indicate tidal decay) or a linear function (Equation 2.4), which would suggest a constant ephemeris.

2.6.1 WASP-4 b

WASP-4 b [Wilson et al., 2008] was one of the early discoveries from the SuperWASP project [Pollacco et al., 2006], and the first exoplanet to be discovered by SuperWASP in the southern hemisphere. The first claims of detection of orbital decay in this system were made by Bouma et al. [2019], and was quickly confirmed by Southworth et al. [2019]. These studies derived decay rates of $-12.6 \pm 1.2\,\mathrm{ms\,yr^{-1}}$ and $-9.2 \pm 1.1\,\mathrm{ms\,yr^{-1}}$ respectively. However, subsequent radial velocity measurements of this system presented in Bouma et al. [2020], suggested that the apparent change in orbital period was due to light travel-time effects from the influence of a wide-orbiting (10-100 AU) companion to the star and its associated reflex motion. This effect was also investigated by Turner et al. [2022], who presented evidence for a companion planet causing this effect in addition to the presence of orbital decay

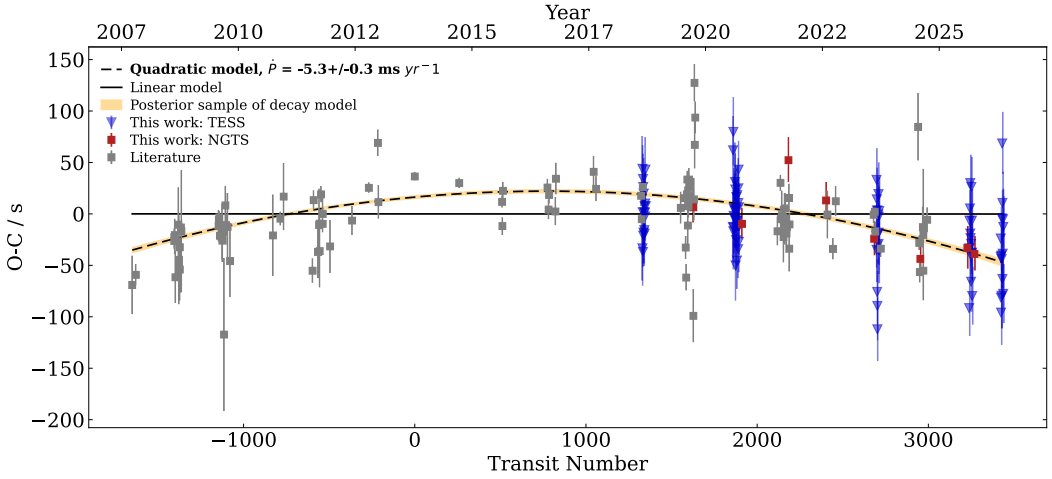


Figure 2.8: O-C diagram for our transit observations of WASP-4 b, corrected to the updated orbital ephemeris in Table 2.2. Grey squares, blue triangles and red squares show transit timing values from the literature, *TESS* and NGTS respectively. Linear and quadratic ephemeris models are shown with solid and dashed lines respectively with the preferred model highlighted in bold font in the legend. We also plot a random sample of 100 draws from the posterior results of the quadratic fit in yellow shading. The orbital decay rate listed in the legend is calculated assuming the quadratic ephemeris trend is the result of true orbital decay.

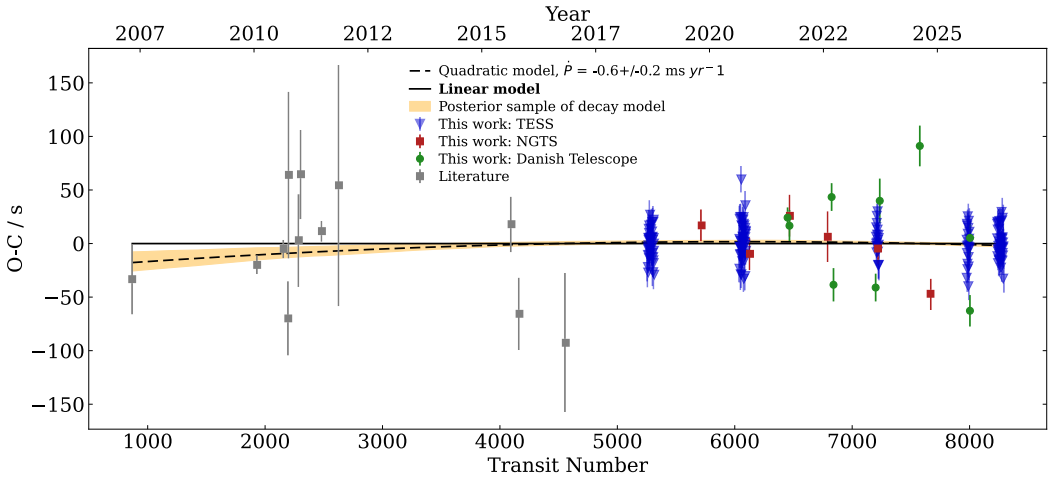


Figure 2.9: As Figure 2.8 but for WASP-18 b.

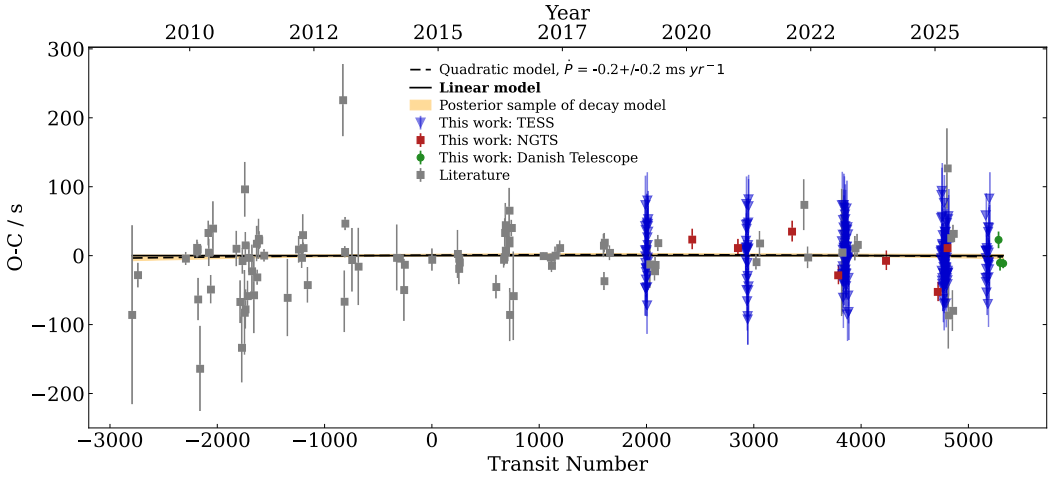


Figure 2.10: As Figure 2.8 but for WASP-19 b.

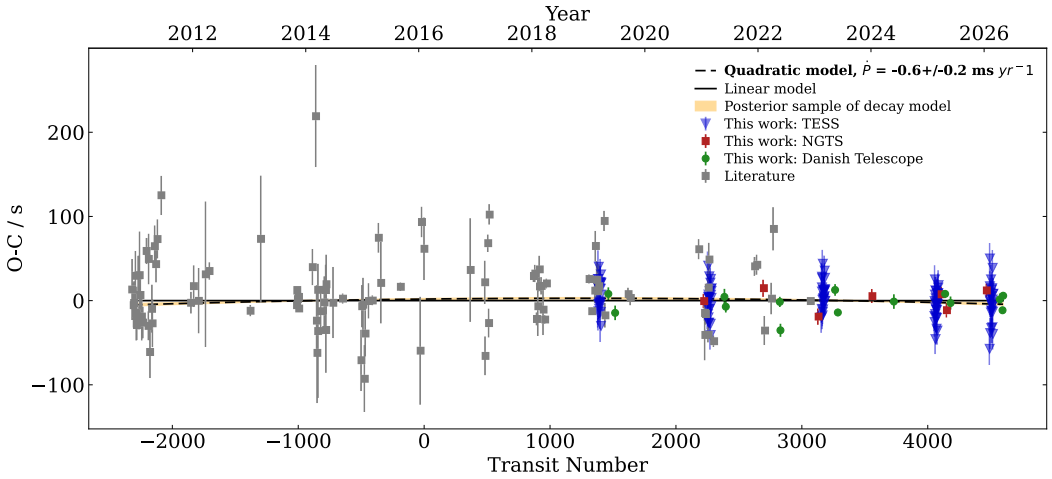


Figure 2.11: As Figure 2.8 but for WASP-43 b.

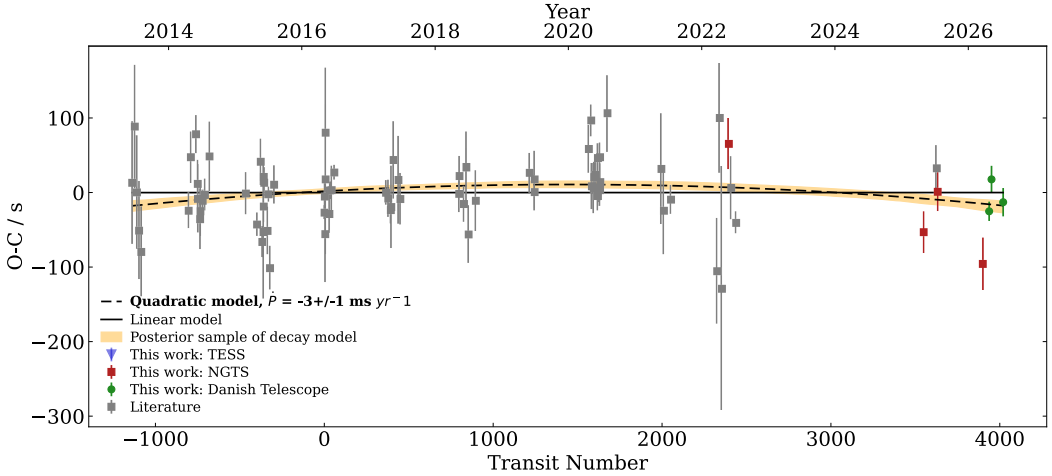


Figure 2.12: As Figure 2.8 but for WASP-103 b.

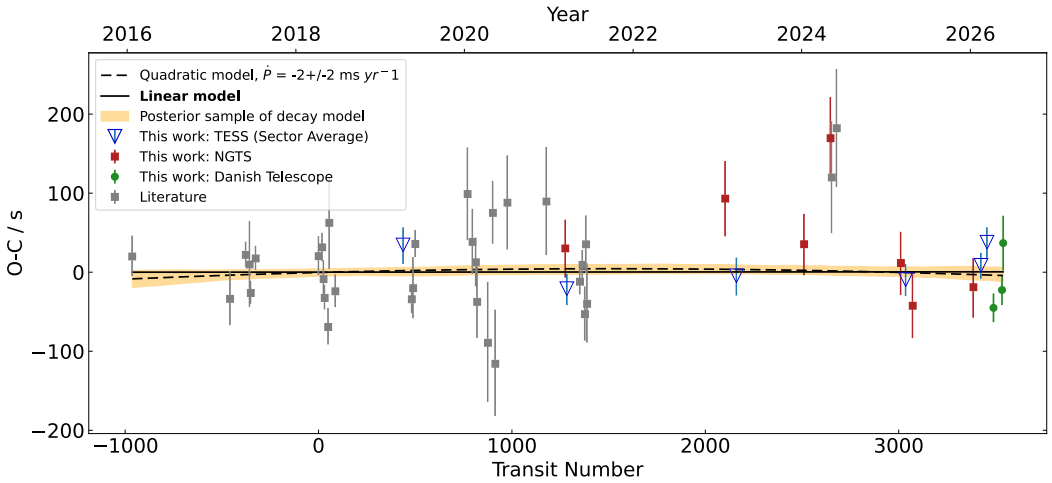


Figure 2.13: As Figure 2.8 but for HATS-18 b. Due to large scatter of the individual *TESS* transit measurements, we plot the average and standard error for a whole sector (open blue triangles). Individual *TESS* timing values were still used in model fitting.

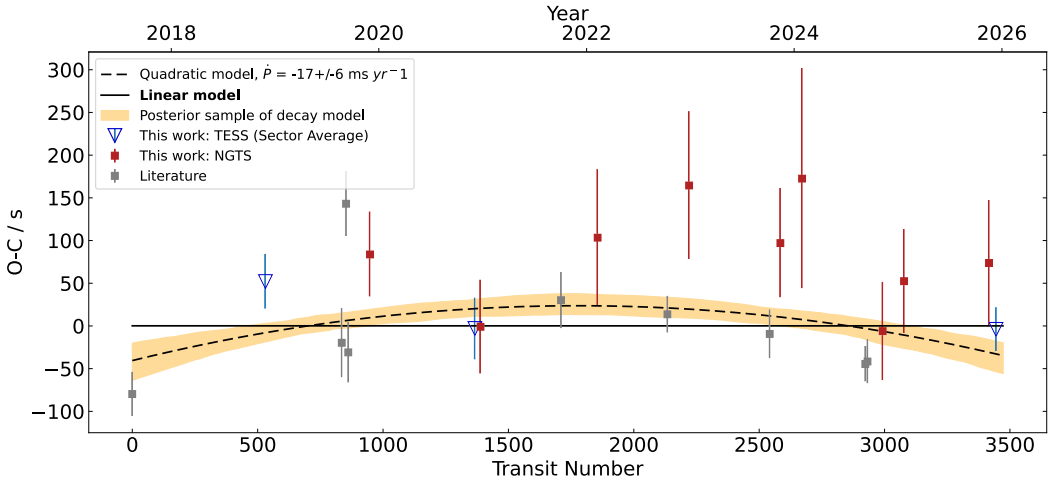


Figure 2.14: As Figure 2.8 but for NGTS-6 b. Due to large scatter of the individual *TESS* transit measurements, we plot the average and standard error for a whole sector (open blue triangles). Individual *TESS* timing values were still used in model fitting.

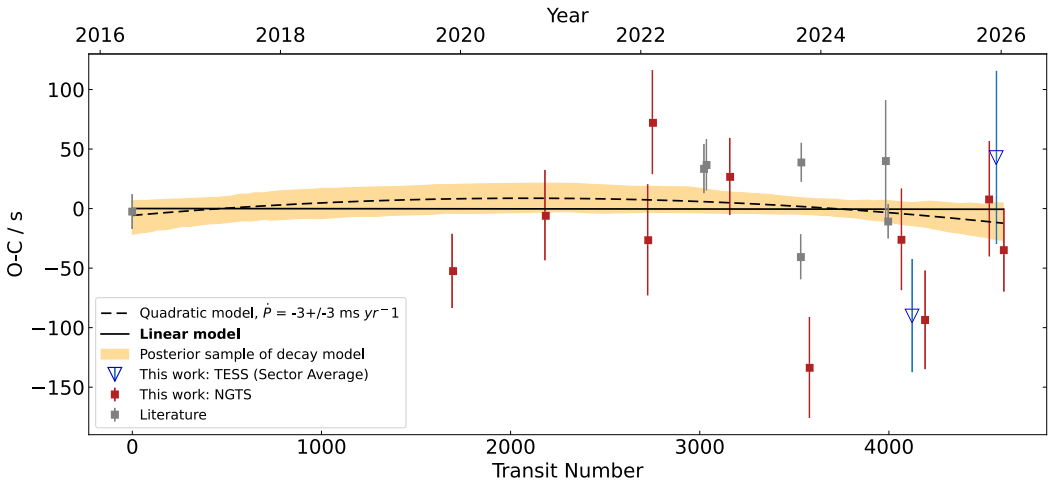


Figure 2.15: As Figure 2.8 but for NGTS-10 b. Due to large scatter of the individual *TESS* transit measurements, we plot the average and standard error for a whole sector (open blue triangles). Individual *TESS* timing values were still used in model fitting.

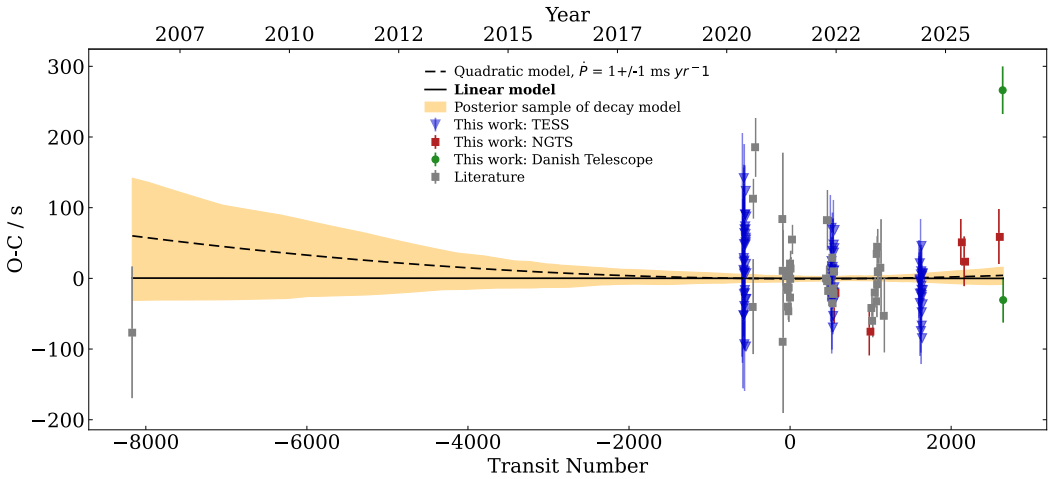


Figure 2.16: As Figure 2.8 but for TOI-2109 b.

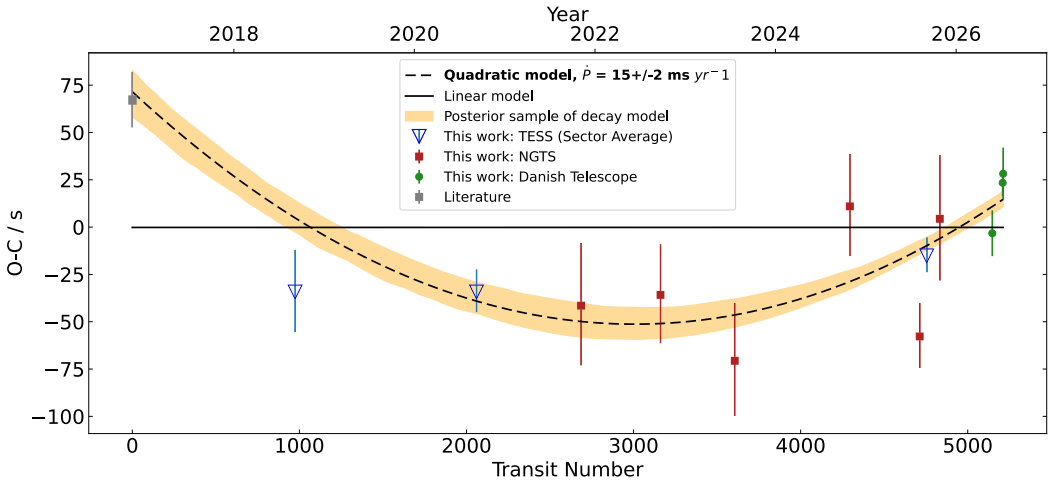


Figure 2.17: As Figure 2.8 but for NGTS-7 A b. Due to large scatter of the individual *TESS* transit measurements, we plot the average and standard error for a whole sector (open blue triangles). Individual *TESS* timing values were still used in model fitting.

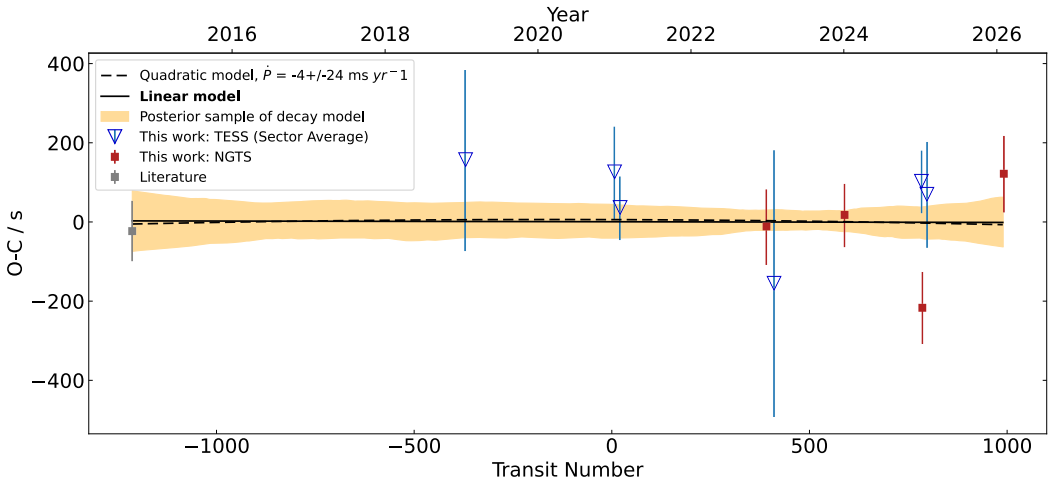


Figure 2.18: As Figure 2.8 but for HATS-70 b. Due to large scatter of the individual *TESS* transit measurements, we plot the average and standard error for a whole sector (open blue triangles). Individual *TESS* timing values were still used in model fitting.

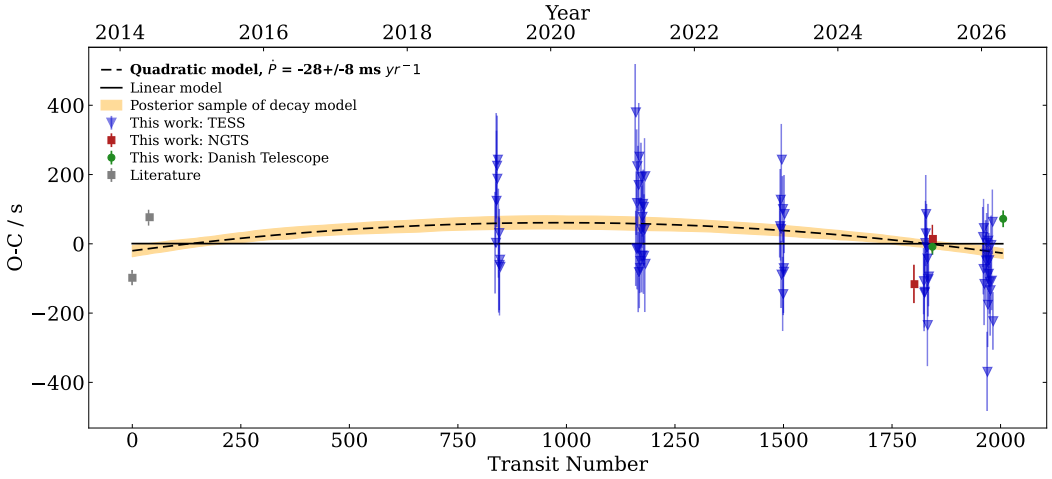


Figure 2.19: As Figure 2.8 but for WASP-128 b.

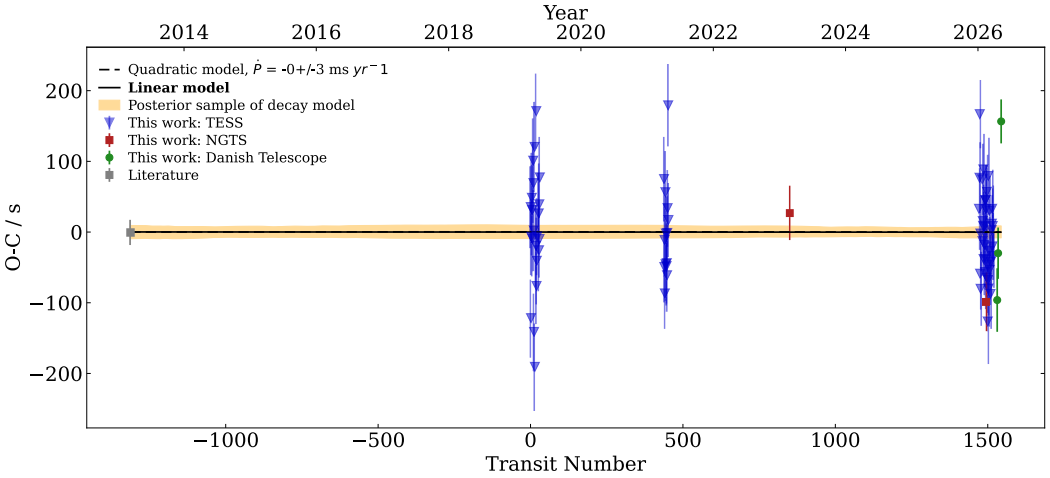


Figure 2.20: As Figure 2.8 but for WASP-87 b.

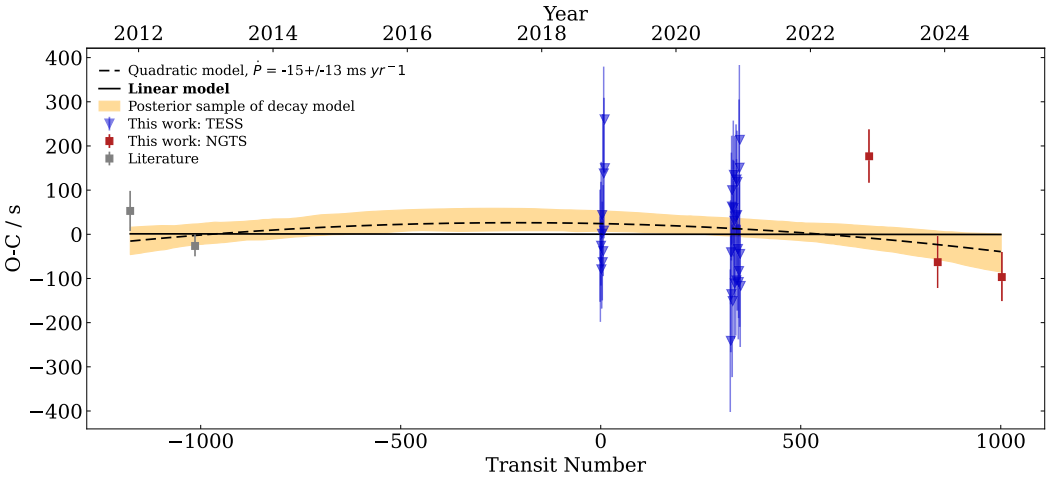


Figure 2.21: As Figure 2.8 but for WASP-78 b.

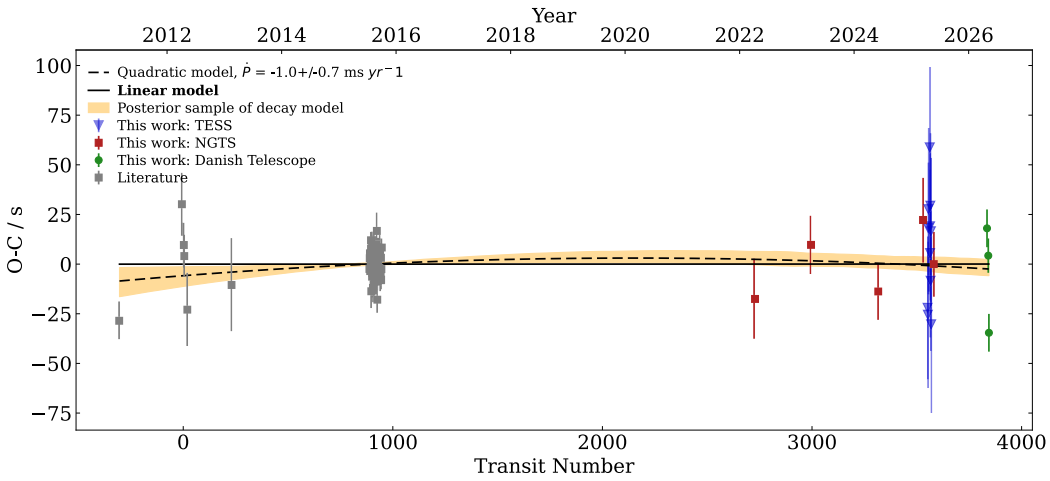


Figure 2.22: As Figure 2.8 but for Qatar-2 b.

at a rate of $-7.33 \pm 0.71\,\mathrm{ms\,yr^{-1}}$.

Harre et al. [2023] investigated this system for signs of orbital decay with the addition of CHEOPS [Benz et al., 2021] data, and found a strong signal for decay at $-6.2 \pm 1.2\,\mathrm{ms\,yr^{-1}}$ but could not rule out the presence of apsidal precession. With the addition of a further *TESS* sector, Harre & Smith [2023] found that the changes to the transit times were most likely caused by a light travel time effect due to a wide-orbiting companion. Baştürk et al. [2025] reported new ground-based transit observations and made a case for tidal decay, however with the addition of Sector 96 observations from *TESS*, Winn & Stefánsson [2025] strongly argued that the changes in transit times are due to light travel-time effects. This rich history of claims and counter-claims of orbital decay detection means WASP-4 is an incredibly interesting system for continued ephemeris monitoring.

In our analysis of WASP-4 (Figure 2.8), we find a best fitting quadratic model with decay rate of $-5.3 \pm 0.3\,\mathrm{ms\,yr^{-1}}$, which is preferred over a linear ephemeris with a ΔBIC value of 345.51, by far the strongest signal in this study. This is consistent to within an order of magnitude to previous results. It uses *TESS* observations as recent as May 2026, and eight NGTS observations from 2019 to 2026, contributing to the unequivocal preference for a quadratic ephemeris. However, determining whether this effect is due to true orbital decay or other effects such as apsidal precession or light travel-time effects from barycentric acceleration of the system is beyond the scope of this study as our observations consist purely of transit timing measurements, whereas long-baseline radial velocity monitoring and occultation timing measurements would be required to rule out these effects [Winn &

Stefánsson, 2025; Yee et al., 2020].

2.6.2 WASP-18 b

At the time of discovery in 2009, WASP-18 b [Hellier et al., 2009] was a planet expected to be undergoing some of the strongest tidal forces known for exoplanets, and for this reason WASP-18 has been one of the most studied systems for tidal effects. It is also the highest mass exoplanet in our sample, at $10.2\,M_J$. Brown et al. [2011] measured the stellar spin rate of WASP-18 to be faster than expected from models, implying that there may have been a transfer of angular momentum from the planet to the star. Recovery of a pre-discovery transit light curve in archival *Hipparcos* data led McDonald & Kerins [2018] to present weak evidence for orbital decay in WASP-18. However, subsequent studies [Wilkins et al., 2017; Maciejewski et al., 2020; Cortés-Zuleta et al., 2020; Patra et al., 2020; Adams et al., 2024; Ma et al., 2025], have found no significant evidence for orbital decay.

In our study, we choose to exclude the pre-discovery timing point from the *Hipparcos* data due to the principles outlined in Section 2.4. We find that the addition of our six NGTS observations to the existing data gives no significant evidence for a quadratic ephemeris in this system, with a ΔBIC value of 1.14 implying no preference for this model (Figure 2.9).

2.6.3 WASP-19 b

WASP-19 b [Hebb et al., 2010] is one of the shortest-period hot Jupiters known, and is predicted to be undergoing strong tidal interactions [Brown et al., 2011].

Ivshina & Winn [2022] found weak evidence of tidal decay in this system, at a rate of $-3.54 \pm 1.18\,\mathrm{ms\,yr^{-1}}$. This is in contrast to analyses from Petrucci et al. [2013], Ma et al. [2025], Maciejewski et al. [2024] and Kutluay et al. [2026] who found no evidence of tidal decay.

The possibility of apsidal precession in this system, as a consequence of eccentricity forcing by this system's wide-orbiting stellar companion, was discussed by Rosário et al. [2022], Biswas et al. [2025] and Rajkumar et al. [2026]. This would provide an explanation for changes in the transit timings observed in WASP-19. Additionally, Biswas et al. [2025] suggested that variations in the quadrupole moment of the star, the Applegate mechanism, as calculated by Watson & Marsh [2010], could contribute to observed timing variations in this system.

For our analysis of this system (Figure 2.10), we primarily use the curation of literature timing values provided by Adams et al. [2024], due to their detailed

analysis of the database provided by Ivshina & Winn [2022], including some notable exclusions of timing values. Our result, similar to Adams et al. [2024], gives no significant evidence for a quadratic ephemeris (ΔBIC = -4.71), and the best fitting quadratic model ($\dot{P} = -0.2 \pm 0.2\,\mathrm{ms\,yr^{-1}}$) is consistent with zero.

2.6.4 WASP-43 b

Early analyses of WASP-43 b [Hellier et al., 2011a] showed some evidence of orbital decay [Murgas et al., 2014; Jiang et al., 2016, $\dot{P} = -0.15 \pm 0.06\,\mathrm{s\ yr^{-1}}$ and $\dot{P} = -29 \pm 7\,\mathrm{ms\ yr^{-1}}$ respectively]. However, further observations analysed by Hoyer et al. [2016] and Stevenson et al. [2017] ruled out a decrease in the orbital period of the system. Similarly, later studies found no significant evidence for tidal decay in the WASP-43 system [Patra et al., 2020; Garai et al., 2021; Davoudi et al., 2021; Alvarado et al., 2024; Maciejewski et al., 2024; Ma et al., 2025]. In contrast, Bernabò et al. [2025] recently performed a joint fit of radial velocity as well as transit observations, and found a best fitting model that incorporated both tidal decay and a high rate of apsidal precession from their discovery that the orbit is slightly eccentric.

In this work, we find a significant suggestion (ΔBIC = 6.45) of the preference for a quadratic ephemeris, with a derived orbital decay rate of $\dot{P} = -0.6 \pm 0.2\,\mathrm{ms\,yr^{-1}}$. In our analysis (Figure 2.11) we have excluded data points compiled by Ivshina & Winn [2022] and originally reported by Saha et al. [2021]. These all appeared consistently anomalous to the trend in this planet's ephemeris, with O-C $\geq$ -100 s below the best-fit quadratic ephemeris. Given the magnitude of these outliers, it is possible that a time system conversion error led to this discrepancy so, for this reason, they were discounted from this study.

2.6.5 WASP-103 b

WASP-103 b [Gillon et al., 2014] has been the subject of numerous studies investigating transit timing [Southworth et al., 2015; Maciejewski et al., 2018; Barros et al., 2022; Baştürk et al., 2022; Maciejewski et al., 2022; Alvarado et al., 2024; Adams et al., 2024; Kutluay et al., 2026], all of which have found no evidence to indicate tidal decay in the system. Additionally, Patra et al. [2020] found tentative evidence for an orbital period increase in their analysis. This observational effort is impeded by the fact that WASP-103 lies close to the ecliptic plane, meaning it has not yet been observed by *TESS* (see Figure 2.2), so does not have as extensive an archive of transit times as other physically similar systems. However, evidence of strong

tidal forces within this system is inferred from the detection of tidal deformation of WASP-103 b from twelve high precision transits using CHEOPS [Barros et al., 2022].

From our analysis we find a significant (ΔBIC = 6.90) orbital decay signature, with $\dot{P} = -3 \pm 1\,\mathrm{ms\,yr^{-1}}$for this system. This is the first suggestion of orbital decay in WASP-103, and is strongly influenced by the three most recent NGTS observations (see Figure 2.12). Continued monitoring of this system by NGTS, and the first planned *TESS* observations in Sector 117, will be essential in determining the robustness of this orbital decay detection.

2.6.6 HATS-18 b

HATS-18 b is an ultra-short period hot Jupiter with a mass of nearly 2 $\mathrm{M_J}$, and has one of the largest predicted timing shift over a decade of observations out of short period systems known at the time of discovery [Penev et al., 2016]. HATS-18 was also found to have a faster stellar spin than predicted given its inferred age, which could be attributed to the transfer of angular momentum to the star as the planet spiralled in [Penev et al., 2016]. No further concrete evidence has been found for decay however, with Southworth et al. [2022] finding no departure from a linear orbital ephemeris with 8 years of transit observations and Maciejewski et al. [2024] also returning no preference for a quadratic ephemeris over a linear ephemeris. Our analysis (Figure 2.13), with the addition of seven new NGTS observations, finds that a linear ephemeris is still preferred for this system, with a ΔBIC value of -4.57.

2.6.7 NGTS-6 b

NGTS-6 b [Vines et al., 2019] is a 1.3 $\mathrm{M_J}$ planet in orbit around a K-star. The only previous timing analysis performed on this system was by Griffiths et al. [2026], who found only a weak statistical preference for decay in this system with $\dot{P} = -21 \pm 9$ms $\mathrm{yr^{-1}}$.

In our analysis of the ephemeris of NGTS-6 b (Figure 2.14), we find no preference (ΔBIC=2.35) for a quadratic ephemeris. Although this ΔBIC value is positive, the low value means that it is not possible to definitively confirm the preference for a quadratic fit. Future observations may strengthen the case for a quadratic fit, and this system is fortunate enough to lie in the first observation field of the *PLATO* mission (see Section 2.7.6), meaning that it will benefit from at least two years of continuous photometric observation from mid-2027.

2.6.8 NGTS-10 b

NGTS-10 b [McCormac et al., 2020] was discovered by the NGTS facility and was the shortest-period hot Jupiter at the time of its discovery in 2020. A predicted transit timing change of 7 s over a 10 year period was calculated by McCormac et al. [2020]. However on analysis of this system, Griffiths et al. [2026] could not place strong constraints on the decay rate of this planet due to a lack of available observations. Our analysis, with the inclusion of 10 NGTS observations, also shows no preference for an orbital decay model over a linear ephemeris with ΔBIC = -3.54 (Figure 2.15).

2.6.9 TOI-2109 b

TOI-2109 b is the shortest period hot-Jupiter known and the most recently discovered of all the planets in this study [Wong et al., 2021]. On its discovery it was predicted to have the highest decay rate of all known hot Jupiters due to its extremely short orbital period of just 0.67 days. However, Harre et al. [2024] only found tentative evidence for tidal decay in the TOI-2019 system using 31 CHEOPS observations and 2 *TESS* sectors. In addition, they found transit timing variations suggestive of a close outer companion in this system with period $P_c > 1.13$ d. Most recently, Alvarado-Montes et al. [2025] conducted a detailed analysis of this system with the addition of *TESS* Sector 79 data, and found tentative evidence for decay with $\dot{P} = -2.6 \pm 1.3 \mathrm{ms\,yr^{-1}}$.

Our timing analysis (Figure 2.16) involved the addition of five NGTS observations, the three *TESS* sectors, and the existing timing measurements in the literature. Despite the recent discovery of this planet, a long observational baseline is available thanks to the archival SuperWASP-N [Pollacco et al., 2006] observations recovered by Harre et al. [2024] that give a timing measurement from 2006. We opted to include this data point, despite generally not including literature timing values generated from multiple light curves (Section 2.4), due to the general reliability of the SuperWASP data and the large increase in observational baseline it afforded. In our analysis, we find no evidence to suggest a departure from a linear ephemeris is preferred (ΔBIC = -4.33), in contrast to the conclusion of Alvarado-Montes et al. [2025].

2.6.10 NGTS-7A b

NGTS-7 A b is a high mass ($62 \pm 17\,\mathrm{M_J}$) brown dwarf orbiting an active M-dwarf host star as part of a hierarchical triple system [Jackman et al., 2019]. It exhibits tidal

interactions through spin-orbit synchronization of the orbit. In addition, the high activity levels of the host star were suggested to cause magnetic braking, further removing angular momentum from the system and giving it a predicted inspiral time of only 5 Myr [Jackman et al., 2019].

The only timing analysis that has previously been performed for this system was by Wang et al. [2025], who had insufficient data to fit an ephemeris model but identified this system as a promising candidate for tidal decay. Through our analysis (Figure 2.17), with six NGTS observations, three *TESS* sectors and three Danish telescope transits, we find a strong (ΔBIC=52.72) preference for a quadratic ephemeris. However, rather than being suggestive of orbital decay, the positive value of $\dot{P} = +15 \pm 2 \mathrm{ms\,yr}^{-1}$ implies that the brown dwarf NGTS-7A b is migrating away from its host star. Given the relatively small number of timing measurements available, it is possible that this is a statistical artefact; however, an alternative explanation is that we are observing transit timing shifts due to the light travel time effect or apsidal precession in this system.

2.6.11 HATS-70 b

HATS-70 b [Zhou et al., 2019] is a low mass brown dwarf orbiting an A-star which, with a mass of 12.9 $\mathrm{M_J}$, lies very close to the deuterium-burning limit. The possibility of decay in this system was explored by both Ivshina & Winn [2022] and Adams et al. [2024] but no statistically significant tidal decay signal was found. For our analysis (see Figure 2.18) we also find no tidal decay signature, with a preference for a linear ephemeris with ΔBIC = -4.23.

2.6.12 WASP-128 b

WASP-128 b [Hodžić et al., 2018] is a 37.5 $\mathrm{M_J}$ brown dwarf orbiting a G-type star, which was predicted on discovery to be undergoing strong interactions through dynamical tides with an infall lifetime of approximately 270 Myr. A correction was made to the original ephemeris of this system [Smith et al., 2020a], and we use this updated ephemeris in this study. The possibility of decay in this system was investigated by Wang et al. [2025], but the short baseline of transit observations for WASP-128 b meant that it was unclear if there was any tidal decay occurring in this system.

We have performed a reanalysis of the original discovery data from Hodžić et al. [2018]. We determined the limb-darkening parameters using the limb-darkening coefficient calculator of Mullen et al. [2026], before performing a timing analysis

using the procedure outlined in Section 2.5. We selected the high signal-to-noise EulerCam observations of 2014 March 03 and 2014 May 26 in our analysis. We did not include the other EulerCam observation or the TRAPPIST observations from this study as they contained high levels of correlated noise that are detrimental to precise transit timing measurements.

Through the combination of these re-analysed observations, 7 *TESS* sectors and two NGTS observations, we find a (ΔBIC = 7.86) suggestion for a quadratic decay model with a decay rate of $\dot{P} = -28 \pm 8 \mathrm{ms\,yr^{-1}}$(see Figure 2.19). This is the largest derived orbital period decay rate we find in this study, however given the high mass of WASP-128 b and the mass dependence in Equation 2.3, this is not a surprising result. We also find a significant correction to the ephemeris of this system is necessary, further to that presented by Smith et al. [2020a], which we discuss in Section 2.7.4.

2.6.13 WASP-87 b

WASP-87 b is a 2.2 $\mathrm{M_J}$ hot Jupiter in a visual binary system, and is one of the most metal poor stars known to host a giant planet [Anderson et al., 2014]. This system has not been very well studied, and there are only two NGTS transits and three *TESS* sectors in addition to the original discovery transits. We find no statistically significant suggestion of orbital decay (ΔBIC=-4.37, see Figure 2.20).

2.6.14 WASP-78 b

WASP-78 b was discovered as part of the SuperWASP survey in 2012 [Smalley et al., 2012]. In addition to the discovery transit observations [Smalley et al., 2012; Ivshina & Winn, 2022], we also use I-band photometry from EulerCam from the night of 2012 November 02 [Brown et al., 2017]. We do not use the EulerCam observation of 2012 November 26 due to the presence of a known spot-crossing event [Brown et al., 2017]. Limb darkening coefficients for this passband were calculated using the limb-darkening calculator of Mullen et al. [2026], and we extracted the timing value using the same procedure as outlined in Section 2.5.

Our results (Figure 2.21) show no statistical preference for a decreasing orbital period (ΔBIC=-2.24).

2.6.15 Qatar-2 b

Qatar-2 b is a 2.49 $\mathrm{M_J}$ hot Jupiter discovered with the Qatar Exoplanet Survey [Bryan et al., 2012]. Its location near the ecliptic plane means that *TESS* has only

recently (Sector 91) included it in its coverage, however the study of this target benefits from *K2* [Howell et al., 2014] observations taken in 2015 and analysed by Močnik et al. [2017] and Dai et al. [2017]. These provide a strong anchor to the timing fits, however our overall result (Figure 2.22) shows no evidence that a quadratic ephemeris is preferred (ΔBIC = -2.51).

2.7 Discussion

2.7.1 Tidal Decay Candidates

In this study we find suggestions of orbital period decrease in three systems: WASP-43, WASP-103, and WASP-128.

WASP-43 shows the smallest period shift, with $\dot{P} = -0.6 \pm 0.2\,\mathrm{ms\,yr^{-1}}$. From Equation 2.3 this equates to a modified tidal quality factor of $Q'_\star = (2.2 \pm 0.7) \times 10^6$. Barker [2020] provide a theoretical prediction of 1.3×10^5 for this system, based on IGW dissipation. They suggest that weakly non-linear mechanisms may be responsible for any observed decay.

WASP-103 shows a tidal decay signal of $\dot{P} = -3 \pm 1\,\mathrm{ms\,yr^{-1}}$, which equates to a modified tidal quality factor of $Q'_\star = (1.9 \pm 0.7) \times 10^6$. Barker [2020] predict a theoretical tidal quality factor of 4×10^5 for this system, and in their simulations they note that they would not have expected to observe tidal decay in this star.

WASP-128 b shows a tidal decay signal of $\dot{P} = -28 \pm 8\,\mathrm{ms\,yr^{-1}}$, which equates to a modified tidal quality factor of $Q'_\star = (1.1 \pm 0.3) \times 10^5$. This is significantly lower than the value predicted by Barker [2020] of $Q'_\star = 1.7 \times 10^8$, for this system based on the dissipation of IGWs in the star, however they note the possibility of this orbit decaying on a timescale of magnetic braking, which could vary the decay rate from that predicted through tidal dissipation.

For reference we note that the WASP-12 system, which has a robust detection of tidal decay, is calculated to have a $Q'_\star$ value of 1.8×10^5 [Yee et al., 2020], broadly consistent with the values we derive for the three detections reported in this work. It is also possible that a combination of the above effects could contribute to the observed difference between our results and the theoretical values. While these signals could be suggestive of tidal decay, we note the possibility of apsidal precession [e.g. for WASP-43 b, Bernabò et al., 2025] and light travel-time effects from a companion [e.g. WASP-4 b, Harre & Smith, 2023; Winn & Stefánsson, 2025] that could contribute to these trends.

2.7.2 Systems with other Timing Shifts

WASP-4 b shows a very strong preference for the quadratic model ($\Delta\mathrm{BIC} = 345.51$). However as noted in previous literature, this is likely due to an outer companion causing a light travel time effect [Harre & Smith, 2023; Winn & Stefánsson, 2025] rather than originating from true tidal decay.

Our results for the NGTS-7A system show evidence for a positive period shift ($\dot{P} = +15 \pm 2\,\mathrm{ms\,yr^{-1}}$), which therefore cannot be caused by tidal decay. Instead this is more likely to be a light travel time effect caused by an outer companion. NGTS-7 A has a known wide-orbiting companion star, NGTS-7 B, with mass $0.35\,\mathrm{M_\odot}$ and projected separation at discovery of 173 au [Jackman et al., 2019]. To check if the binary companion could be responsible for this light travel time effect, we use the time shift equations of Harre & Smith [2023] for a circular orbit and Irwin [1952] for an eccentric orbit.

For a circular orbit, we find that the maximum time-shift over the orbital period of NGTS-7 B would be ∼1.5 days, which would also correspond to a time shift of around 10 s over the ∼2500 day observing baseline available, less than that observed. However in the case of high eccentricity (∼0.8) and 90°inclination, a period shift of a similar magnitude to that observed is possible. Therefore while it is possible that the known companion NGTS-7 B could be the cause of these observed time shifts, it would require a very specific orbital configuration and a similar effect could arise from a massive companion closer in to the system.

The remaining systems in our study do not, as yet, show any evidence for tidal decay.

2.7.3 *Gaia* Astrometry

Astrometric information from the *Gaia* mission [Gaia Collaboration et al., 2016] is useful to determine if the host stars of our sample have unseen companions [e.g. WASP-19, Bernabò et al., 2024]. Such companions can cause light travel time effects that may be detectable in our analysis. In December 2026 *Gaia* Data Release 4 (DR4) will be released,[6] which will provide epoch astrometry over a 5.5 yr baseline. This will allow us to further constrain any outer companions to these systems, primarily in the brown dwarf or low mass star regime.

Prior to the release of the astrometry from *Gaia* DR4, we can use existing data available from *Gaia* DR3 [Gaia Collaboration et al., 2023]. The Re-normalised Unit Weight Error (RUWE) values from *Gaia* DR3 can be used as an indication of

[6] `https://www.cosmos.esa.int/web/gaia/data-release-4`

System	$M_\star$ ($M_\odot$)	Distance (pc)	*Gaia* RUWE
WASP-4	$0.899^{+0.033}_{-0.031}$	272^{+2}_{-1}	1.05
WASP-18	$1.294^{+0.063}_{-0.061}$	$123.5^{+0.2}_{-0.1}$	0.95
WASP-19	$0.965^{+0.091}_{-0.095}$	256.2 ± 0.6	0.85
WASP-43	0.688 ± 0.037	87.0 ± 0.1	1.15
WASP-103	$1.220^{+0.039}_{-0.036}$	520 ± 30	7.24
HATS-18	1.037 ± 0.047	607 ± 6	1.02
NGTS-6	0.767 ± 0.025	303 ± 1	1.07
NGTS-10	0.696 ± 0.040	270 ± 10	12.33
TOI-2109	$1.477^{+0.075}_{-0.078}$	266 ± 1	1.02
NGTS-7A	$0.47^{+0.03}_{-0.012}$	146 ± 2	2.01
HATS-70	1.78 ± 0.12	1270 ± 20	0.98
WASP-128	1.155 ± 0.039	411 ± 2	1.00
WASP-87	$1.220^{+0.039}_{-0.036}$	290 ± 2	1.24
WASP-78	$1.39^{+0.09}_{-0.08}$	706 ± 7	1.09
Qatar-2	0.727 ± 0.024	$181.2^{+0.6}_{-0.5}$	1.02

Table 2.3: The stellar masses (sources listed in Table 2.4) for host stars in our sample, along with the *Gaia* DR3 distances [Bailer-Jones et al., 2021] and RUWE (Re-normalised Unit Weight Error) measurements [Gaia Collaboration et al., 2023].

the presence of an unresolved binary system, with values around 1 suggesting a single star and above a threshold of >1.25 suggesting potential evidence for an orbiting companion in the *Gaia* astrometry [Penoyre et al., 2022; Castro-Ginard et al., 2024]. The RUWE values for each host star in our sample are set out in Table 2.3. The majority of the host stars in our sample have RUWE values consistent with a single star, with three exceptions discussed below, in order of decreasing RUWE.

NGTS-10 has a significantly elevated RUWE value of 12.33, suggestive of a binary companion in this system. However, based on information from *Gaia* DR2, McCormac et al. [2020] noted the presence of a background star at a projected separation of only 1.2" and speculated that this could be the source of the astrometric excess noise of NGTS-10. This background star remains present in *Gaia* DR3 (source ID 2911987212508106880), but in contrast to NGTS-10 it has a normal RUWE of 1.04, suggesting the astrometry of this star has not been strongly affected by NGTS-10. The observed astrometric excess noise may therefore be intrinsic to NGTS-10 alone. From our timing analysis, we find no suggestion of a deviation from a linear ephemeris in this system (Figure 2.15), indicating that if NGTS-10 has an additional companion responsible for the excess astrometric noise, it does not impart a detectable light travel time effect signal. The origin of the elevated astrometric noise of NGTS-10 may be elucidated in *Gaia* DR4.

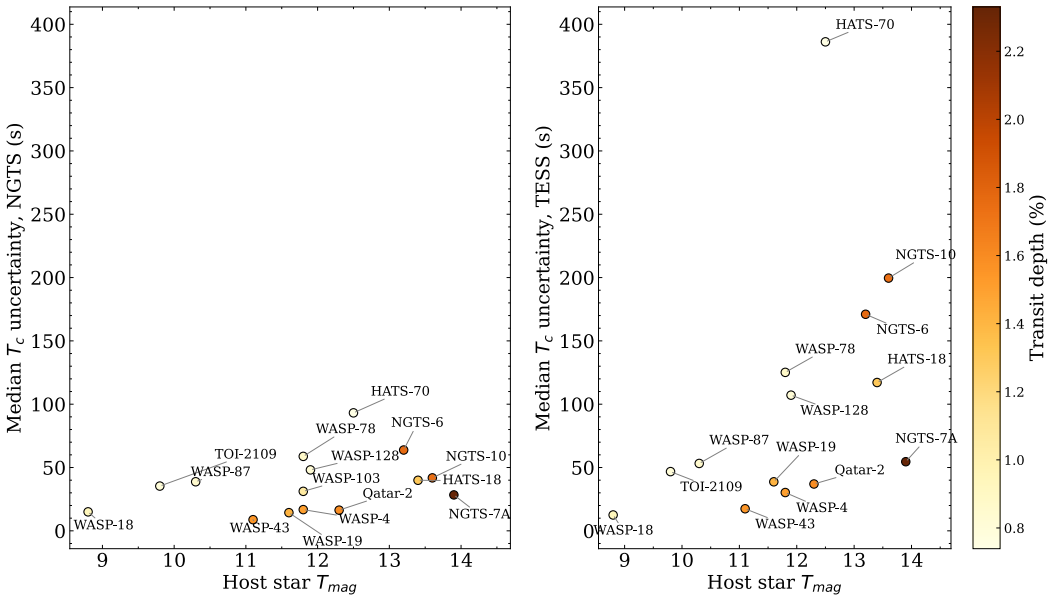


Figure 2.23: Plot of the median error on derived mid-transit times in our NGTS (left) and *TESS* (right) observations against the *TESS* Magnitude of the host star, with labels showing the names of the systems. The colour scale indicates the transit depth.

WASP-103 has an elevated RUWE value of 7.24, strongly suggesting a source of astrometric noise in this system. A candidate stellar companion to this system was previously detected by Wöllert & Brandner [2015] using Lucky Imaging observations and by Ngo et al. [2016] with high-resolution Adaptive Optics observations at a projected separation of 0.24", however they note that they could not rule out this being a background object. Barros et al. [2022] also performed Lucky Imaging observations of the same system, but did not detect the companion candidate and concluded that the previously imaged companion is most likely not bound to WASP-103. This study also noted the elevated astrometric noise of the star. The second star is not detected in *Gaia* DR3, presumably because of its close separation, but regardless of whether it is bound or a background star it could conceivably affect the *Gaia* astrometry; however, only if it were gravitationally bound could it possibly influence the drift in the planetary transit ephemeris observed in this work. Further observations and *Gaia* DR4 astrometry will allow for further constraints on the behaviour of this system.

In the discovery paper, based upon *Gaia* DR2, Jackman et al. [2019] observe that NGTS-7A has an elevated RUWE of 3.4, whereas the stellar companion NGTS-7B has a more typical value of 1.3. In *Gaia* DR3 this pattern is conserved, with

the primary showing a high RUWE of 2.01 while the secondary has a low RUWE of 0.89. Jackman et al. [2019] note that given the close angular separation of the binary (1.13") there is a risk of confusion in the *Gaia* astrometry; however, it is difficult to see why this would disproportionately affect only the primary star. It may therefore be preferable to consider the astrometric excess noise as intrinsic to NGTS-7A. As set out in Section 2.6, NGTS-7Ab shows evidence for an increasing period, which is inconsistent in sign with the hypothesis of tidal decay. It is possible this is could be due to the light travel time effect of a hypothetical third companion that is also the cause of the high RUWE value; the period of the transit timing variation appears to exceed the 9-yr baseline of the transit observations, which is plausibly compatible with the 3-yr duration of *Gaia* DR3. It will be interesting to explore the companion hypothesis further with the forthcoming release of the epoch *Gaia* astrometry in *Gaia* DR4.

2.7.4 Ephemeris Updates

In the process of measuring transit times to look for tidal decay signatures, we also calculate the orbital ephemeris based on all available data. These new ephemerides represent the most up-to-date and accurate ephemerides for the 15 systems in our study, and should be used by anyone interested in photometrically or spectroscopically monitoring future transit events. These are presented in Table 2.2.

A particularly significant ephemeris update worth noting is for the WASP-128 system. Our work corrects the orbital period by almost 1 s, corresponding to a shift of nearly 30 min over a ten year duration.

2.7.5 Transit Timing Precision

With 15 systems studied in the NGTS Orbital Decay programme, we can investigate the transit timing precision we achieve for each system using both NGTS and *TESS* light curves. As expected, the transit timing precision is a function of both the magnitude of the host star and the depth of the transit events – see Figure 2.23. The best median precision achieved for a single transit event with NGTS is 8.8 s. This is for the WASP-43 system, which has a bright host star and a deep transit. For other systems our precision is typically between 10-60 s. One exception is the transit timing of HATS-70 b which gives the highest median uncertainty at 93.2 s. The HATS-70 system has shallow transits and a relatively faint host star, giving a lower signal-to-noise ratio for these observations.

The transit timing precision for the *TESS* light curves follows a similar trend

to the NGTS timings, although for single transits *TESS* is less precise as the *TESS* telescopes have a smaller diameter. NGTS observations use multiple telescopes (typically 6 telescopes) and the observing cadence of *TESS* is much slower than NGTS.

2.7.6 Future Follow-up

Over the coming years we expect the study our systems to benefit from new releases of data, and we provide a brief description of these below.

As discussed in Section 2.7.3, *Gaia* DR3 [Gaia Collaboration et al., 2023] has already offered insight into the system architectures of the exoplanets examined by this work. *Gaia* DR4 will extend the baseline of astrometric observations from almost 3 years (34 months) to 5.5 years, provide epoch astrometric data across that period of time, and is expected to have increased astrometric precision when compared to *Gaia* DR3. To further explore what unresolved companions may be detected in *Gaia* DR4 astrometry around our target systems, we calculate *Gaia*'s ability to detect orbiting companions around these host stars.

From these calculations, we determined that primarily due to their distances (see Table 2.3), *Gaia* DR4 will only be able to detect brown dwarfs or low-mass stellar companions for most of the host stars in our sample. The exception to this is WASP-43, which at a distance of only 87 pc will mean that *Gaia* DR4 will be able to detect an unseen companion on a 5 yr orbital period down to a mass of $\sim 3\,M_J$.

ESA's *PLATO* (PLAnetary Transits and Oscillations of stars) Mission [Rauer et al., 2025], due to launch in March 2027, will provide continuous photometric observations of a section of the sky for at least two years, making this a valuable future prospect for long-term transit monitoring. In particular, the LOPS2 (Long Observation Phase South) field [Nascimbeni et al., 2022, 2025], *PLATO*'s first two-year pointing, significantly overlaps with the visibility region of NGTS and therefore with the on-sky region of our programme. The systems NGTS-6, NGTS-10 and HATS-70 are in the LOPS2 region, and are included in the PIC [*PLATO* Input Catalogue; Montalto et al., 2026]. These systems will be observed with six, twelve and six *PLATO* cameras respectively for the duration of the LOPS2 observation phase [Eschen et al., 2024] – see Figure 2.24.

For the purposes of long-term transit monitoring, the two year guaranteed monitoring period of the *PLATO* LOPS2 field is short compared to the 10+ yr baseline required for determining tidal decay signatures. However, the observing strategy of *PLATO* after the first two years is not confirmed. With the nominal mission lasting four years and a possible extension expanding observations to eight

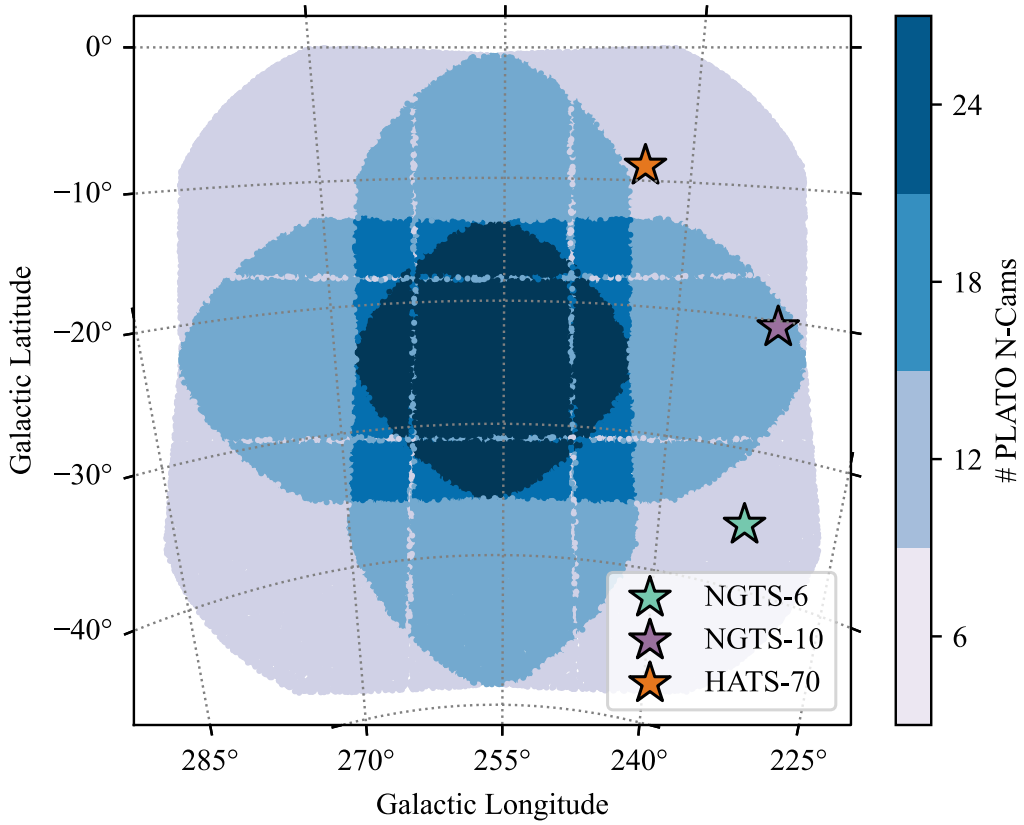


Figure 2.24: Position of targets in this programme within *PLATO*'s LOPS2 field [Eschen et al., 2024]. Darker shades correspond to more cameras observing a particular region. This visibility plot is shown on a galactic coordinate system.

years [Rauer et al., 2025], one possibility would be to monitor the LOPS2 field for up to 4 or 8 years continuously as discussed in Eschen et al. (in prep.). Such long-term monitoring would enable more precise determination of long-term ephemeris trends. Regardless, the high precision and continuous coverage of *PLATO* will provide extremely valuable anchors for transit timing analyses of ultra-short period transiting systems.

The continuation of the *TESS* mission in the coming years, with its repeated high-quality photometric observations, will greatly improve the prospects for confirming orbital decay in these systems when it returns to these regions of the sky. In particular, we note that *TESS* gives very high timing precision for systems with bright host stars (T<12.5) – see Figure 2.23, essential for further high-precision transit time analysis.

2.8 Conclusion

In this work we have presented an overview of the NGTS Orbital Decay Programme, a long-term campaign to monitor the orbital ephemerides of known transiting hot Jupiters and brown dwarfs with ultra-short ($\lesssim$2 day) orbits using high-precision photometric observations taken with the NGTS facility at Cerro Paranal, Chile. We aim to determine whether these systems are exhibiting signs of orbital period decrease over multi-decade timescales. This programme is complementary to the observational efforts of the *TESS* mission and other ground-based facilities.

We find that for the majority of systems studied, no statistical preference is present to indicate a deviation from a linear ephemeris at the current level of precision. However, the ephemerides of five of our targets show a preference for a quadratic trend. We confirm the strong quadratic trend previously seen in the timing data for WASP-4 b but note that this may be due to light travel time effects [Winn & Stefánsson, 2025]. We find tentative evidence for a quadratic trend that may be due to orbital decay in WASP-43 b,WASP-103 b and WASP-128 b, and a positive quadratic trend in NGTS-7 A b.

While we present evidence for orbital decay in three systems, we advise caution in the interpretation of these signals as true orbital decay. Studies of similar systems [Bouma et al., 2020; Winn & Stefánsson, 2025; Rajkumar et al., 2026] have shown how effects such as apsidal precession from a slightly eccentric orbit and variations in light-travel time due to the acceleration of the system, possibly due to a wide-orbiting companion, can mimic the appearance of orbital decay when solely studying photometric TTVs. Therefore, follow-up occultation timing and radial velocity observations, as well as information on unseen stellar companions from *Gaia* DR4, will be necessary to robustly confirm whether these timing signals are due to orbital decay.

In addition, some of the systems presented in this study (such as NGTS-7A b, WASP-87 b, WASP-78 b, Qatar-2 b) suffer from limited archival transit-timing coverage. Continued ephemeris monitoring of these systems, and indeed all systems in this study, will aid in the future detection of orbital period decay. The continuation of the NGTS and *TESS* missions, as well as input from future observatories such as *PLATO*, will prove vital in constraining and predicting the future evolution of these important exoplanet systems.

Table 2.4: Stellar parameters for the 15 decay candidates targeted by NGTS in this study. *: Target hosts a brown dwarf. **: Different source used for determination of limb darkening parameters: WASP-4: Bouma et al. [2019]; WASP-103: Barros et al. [2022]; HATS-18: Penev et al. [2016]; WASP-87: Anderson et al. [2014]; WASP-78: Smalley et al. [2012]; Qatar-2: Esposito et al. [2017]

Target Name	TIC ID	RA (J2000)	Dec (J2000)	V_{mag}	T_{mag} (K)	T_{eff}	Discovery Paper	Parameter Source
WASP-4	402026209	23h34m15.10s	-42°03'42.41"	12.5	11.8	5500	Wilson et al. [2008]	Baştürk et al. [2025]**
WASP-18	100100827	01h37m25.07s	-45°40'40.06"	9.3	8.8	6226	Hellier et al. [2009]	Cortés-Zuleta et al. [2020]
WASP-19	35516889	09h53m40.02s	-45°39'32.79"	12.2	11.6	5500	Hebb et al. [2010]	Cortés-Zuleta et al. [2020]
WASP-43	36734222	10h19m37.96s	-09°48'23.20"	12.3	11.1	4120	Hellier et al. [2011a]	Esposito et al. [2017]
WASP-103	276754403	16h37m15.57s	07°11'00.15"	12.4	11.8	6110	Gillon et al. [2014]	Bonomo et al. [2017]**
HATS-18	14614418	11h35m49.78s	-29°09'21.83"	14.2	13.4	5670	Penev et al. [2016]	Chakrabarty & Sengupta [2019]**
NGTS-6	1528696	05h03m10.89s	-30°23'58.06"	14.2	13.2	4670	Vines et al. [2019]	Vines et al. [2019]
NGTS-10	37348844	06h07m29.35s	-25°35'41.63"	14.5	13.6	4400	McCormac et al. [2020]	McCormac et al. [2020]
TOI-2109	392476080	16h52m44.71s	16°34'49.70"	10.2	9.8	6650	Wong et al. [2021]	Wong et al. [2021]
NGTS-7A*	2055733261	23h30m05.20s	-38°58'11.17"	15.5	13.9	3360	Jackman et al. [2019]	Jackman et al. [2019]
HATS-70*	98545929	07h16m25.09s	-31°14'39.82"	12.2	12.5	8550	Zhou et al. [2019]	Zhou et al. [2019]
WASP-128*	180991313	11h31m26.10s	-41°41'22.30"	12.4	11.9	5960	Hodžić et al. [2018]	Hodžić et al. [2018]
WASP-87	15445551	12h21m17.92s	-52°50'26.94"	10.8	10.3	6460	Anderson et al. [2014]	Addison et al. [2016]**
WASP-78	139528693	04h15m01.50s	-22°06'59.00"	12.0	11.8	6290	Smalley et al. [2012]	Brown et al. [2017]**
Qatar-2	2521105	13h50m37.32s	-06°48'14.66"	13.4	12.3	4460	Bryan et al. [2012]	Močnik et al. [2017]**

2.9 Decay Candidate Stellar Parameters

2.10 Decay Candidate Planetary Parameters

Table 2.5: Planetary parameters for the 15 Hot Jupiter decay candidates targeted by NGTS. Values for T_c and Period are taken from the ephemeris tables of Ivshina & Winn [2022] unless labelled otherwise. a: Value from planet discovery paper; b: Value from Smith et al. [2020a]; $*$: T_c value quoted simply as BJD so the timing regime is unclear; $**$: Time conversion completed using the online calculator of Eastman et al. [2010].

Target Name	M_p (M_J)	R_p (R_J)	Period days	T_c / BJD_{TDB} - 2,400,000	Transit Depth	Transit Duration / hrs
WASP-4 b	1.20±0.03	$1.349^{+0.011}_{-0.012}$	1.338230994±0.000000084	56576.675079±0.000031	2.7%	2.16±0.01
WASP-18 b	10.20±0.35	1.240±0.079	0.941452422±0.00000035	53403.35962±0.000020	1.1%	2.05 ±0.04
WASP-19 b	1.15±0.08	$1.415^{+0.044}_{-0.048}$	0.788839025±0.000000022	56977.776606±0.000042	2.3%	1.64±0.01
WASP-43 b	1.78±0.10	$0.93^{+0.07}_{-0.09}$	0.813474037±0.000000028	57423.449697±0.000048	2.6%	1.26±0.01
WASP-103 b	1.49±0.09	$1.528^{+0.073}_{-0.047}$	0.92554542±0.00000011	57511.944436±0.000076	1.1%	2.59 ± 0.02
HATS-18 b	1.98±0.08	1.329±0.075	0.8378434±0.0000016	58217.64374±0.00016	2.1%	2.16±0.03
NGTS-6 b	1.34±0.03	$1.326^{+0.097}_{-0.112}$	0.882059±0.0000008	57982.3784±0.003*	1.2%	0.58±0.10
NGTS-10 b	$2.16^{+0.09}_{-0.11}$	$1.205^{+0.117}_{-0.083}$	0.7668944±0.0000003	57518.844568±0.00017	3.1%	1.09±0.02
TOI-2109 b	5.02±0.75	1.347±0.047	0.67247414±0.00000028[a]	59378.459370±0.000059[a]	0.78%	1.80±0.13
NGTS-7 A b	62±17	1.07±0.28	0.675990±0.0000001	$57708.554102^{+0.0000017}_{-0.0000055}$ [a,**]	5.4%	1.3±0.3
HATS-70 b	$12.9^{+1.8}_{-1.6}$	$1.384^{+0.079}_{-0.074}$	1.8882393±0.0000031	59202.3099±0.0012	0.44%	3.67±0.12
WASP-128 b	37.5±0.8	0.94±0.02	2.20883665±0.00000045	56720.68772±0.00021[b]	0.78%	2.54±0.09
WASP-87 b	2.18±0.15	1.385±0.060	1.68279426±0.00000040	58571.34992±0.00014	0.81%	3.03±0.02
WASP-78 b	1.11±0.54	1.93±0.45	2.1751847±0.0000040	58440.3768±0.0022	0.78%	4.79±0.04
Qatar-2 b	2.49±0.05	1.254±0.013	1.33711647±0.00000026	56030.75054±0.00015	2.6%	1.81±0.01

2.11 Observation summaries

Table 2.6: Summary of NGTS observations presented in this work.

Target	TIC ID	Obs-night	Time (hr)	Ncam	Nimage	Airmass
WASP-4	402026209	25/09/2019	5.2	6	8770	$1.3 \rightarrow 1.05 \rightarrow 1.2$
WASP-4	402026209	09/10/2020	5.0	5	7006	$1.05 \rightarrow 1.6$
WASP-4	402026209	08/10/2021	4.2	4	4714	$1.05 \rightarrow 1.5$
WASP-4	402026209	28/07/2022	6.5	6	10869	$1.75 \rightarrow 1.05 \rightarrow 1.2$
WASP-4	402026209	08/08/2023	5.0	6	8360	$1.15 \rightarrow 1.3$
WASP-4	402026209	02/08/2024	6.2	5	8771	$1.35 \rightarrow 1.05 \rightarrow 1.25$
WASP-4	402026209	05/08/2025	5.7	6	9692	$1.3 \rightarrow 1.05 \rightarrow 1.3$
WASP-4	402026209	29/09/2025	8.7	6	14529	$1.6 \rightarrow 1.05 \rightarrow 2.0$
WASP-18	100180827	28/10/2019	4.1	6	6980	$1.25 \rightarrow 1.15$
WASP-18	100180827	17/11/2020	4.5	6	7493	$1.15 \rightarrow 1.35$
WASP-18	100180827	02/10/2021	4.0	4	4451	$1.1 \rightarrow 1.45$
WASP-18	100180827	03/08/2022	5.4	3	4241	$2.0 \rightarrow 1.1$
WASP-18	100180827	10/09/2023	5.3	6	8972	$1.4 \rightarrow 1.05 \rightarrow 1.2$
WASP-18	100180827	03/11/2024	8.0	6	13537	$1.4 \rightarrow 1.05 \rightarrow 2.0$
WASP-19	35516889	10/02/2020	4.8	6	8111	$1.25 \rightarrow 1.2$
WASP-19	35516889	11/01/2021	4.1	6	6954	$1.3 \rightarrow 1.1$
WASP-19	35516889	11/02/2022	6.0	5	8360	$1.2 \rightarrow 1.6$
WASP-19	35516889	17/01/2023	4.7	6	7843	$1.4 \rightarrow 1.15$
WASP-19	35516889	03/01/2024	3.8	6	6402	$1.35 \rightarrow 1.1$
WASP-19	35516889	18/01/2025	5.0	6	8370	$1.25 \rightarrow 1.2$
WASP-19	35516889	31/03/2025	4.2	6	7112	$1.2 \rightarrow 1.2$
WASP-43	36734222	16/01/2021	3.0	5	4182	$1.15 \rightarrow 1.1$
WASP-43	36734222	04/02/2022	5.5	5	6782	$1.3 \rightarrow 1.05 \rightarrow 1.4$
WASP-43	36734222	23/01/2023	3.6	5	5074	$1.1 \rightarrow 1.2$
WASP-43	36734222	07/01/2024	3.6	6	6118	$1.4 \rightarrow 1.05$
WASP-43	36734222	28/03/2025	4.4	6	7393	$1.35 \rightarrow 1.1$
WASP-43	36734222	02/05/2025	3.5	6	5866	$1.05 \rightarrow 1.35$
WASP-43	36734222	13/01/2026	3.0	5	4181	$1.15 \rightarrow 1.05$
WASP-103	276754403	27/05/2022	5.5	4	6140	$1.7 \rightarrow 1.2 \rightarrow 1.5$
WASP-103	276754403	29/04/2025	6.7	6	11257	$2.0 \rightarrow 1.2 \rightarrow 1.8$
WASP-103	276754403	15/07/2025	5.9	6	9933	$1.5 \rightarrow 1.2 \rightarrow 2.0$
WASP-103	276754403	18/03/2026	3.4	6	5734	$2.0 \rightarrow 1.2$
HATS-18	14614418	12/03/2021	5.0	5	6940	$1.1 \rightarrow 1.35$
HATS-18	14614418	02/02/2023	4.7	6	7816	$1.3 \rightarrow 1.1$
HATS-18	14614418	09/01/2024	4.3	6	7283	$2.0 \rightarrow 1.0$
HATS-18	14614418	03/05/2024	4.5	5	6272	$1.1 \rightarrow 1.2$
HATS-18	14614418	03/03/2025	8.6	6	14452	$2.0 \rightarrow 1.0 \rightarrow 1.7$
HATS-18	14614418	24/04/2025	7.2	6	12130	$1.25 \rightarrow 1.0 \rightarrow 2.0$
HATS-18	14614418	12/01/2026	3.7	6	6260	$2.0 \rightarrow 1.0$
NGTS-6	1528696	29/11/2019	2.8	6	4756	$1.15 \rightarrow 1.0$
NGTS-6	1528696	22/12/2020	3.0	5	3549	$1.05 \rightarrow 1.1$
NGTS-6	1528696	07/02/2022	2.6	5	3630	$1.0 \rightarrow 1.45$
NGTS-6	1528696	25/12/2022	3.2	6	5022	$1.05 \rightarrow 1.1$
NGTS-6	1528696	11/11/2023	2.6	6	4431	$1.15 \rightarrow 1.0$
NGTS-6	1528696	26/01/2024	2.8	6	4733	$1.0 \rightarrow 1.2$
NGTS-6	1528696	04/11/2024	4.7	6	7987	$1.25 \rightarrow 1.1$
NGTS-6	1528696	19/01/2025	2.8	6	4635	$1.05 \rightarrow 1.1$
NGTS-6	1528696	13/11/2025	2.8	6	4712	$1.1 \rightarrow 1.0$

2.12 References for Literature Transit Times

As described in Section 2.4, the data analysis in this study required the collation of 538 transit timing measurements from across the peer-reviewed scientific literature. Here we provide the citations for the literature sources used:

WASP-4: Ivshina & Winn [2022]; Wilson et al. [2008]; Gillon et al. [2009]; Southworth et al. [2019]; Winn et al. [2009]; Hoyer et al. [2013]; Dragomir et al. [2011]; Sanchis-Ojeda et al. [2011]; Nikolov et al. [2012]; Ranjan et al. [2014]; Baluev et al. [2019]; Huitson et al. [2017]; Bouma et al. [2020]; Baştürk et al. [2025]; Harre et al. [2023]; WASP-18: Ivshina & Winn [2022]; Hellier et al. [2009]; Maxted et al. [2013]; Ma et al. [2025]; Wilkins et al. [2017]; Patra et al. [2020]; WASP-19: Adams et al. [2024]; Hebb et al. [2010]; Lendl et al. [2013]; Hellier et al. [2011b]; Tregloan-Reed et al. [2013]; Petrucci et al. [2020]; Mancini et al. [2013]; Dragomir et al. [2011]; Ma et al. [2025]; Kutluay et al. [2026]; Espinoza et al. [2019]; Patra et al. [2020]; Sedaghati et al. [2017]; WASP-43: Wang et al. [2021]; Ricci et al. [2015]; Davoudi et al. [2021]; Alvarado et al. [2024]; Gillon et al. [2012]; Murgas et al. [2014]; Chen et al. [2014]; Jiang et al. [2016]; Stevenson et al. [2014]; Hoyer et al. [2016]; Stevenson et al. [2017]; Patra et al. [2020]; A-thano et al. [2026]; Garai et al. [2021]; Saha et al. [2021]; Murphy et al. [2023]; Bell et al. [2024]; Ivshina & Winn [2022]; WASP-103: Ivshina & Winn [2022]; Gillon et al. [2014]; Southworth et al. [2015]; Alvarado et al. [2024]; Baştürk et al. [2022]; Delrez et al. [2018]; Barros et al. [2022]; Kreidberg et al. [2018]; Turner et al. [2017]; Kirk et al. [2021]; Lendl et al. [2017]; Patra et al. [2020]; Maciejewski et al. [2018, 2022]; Kutluay et al. [2026]; HATS-18: Ivshina & Winn [2022]; Penev et al. [2016]; Patra et al. [2020]; Kutluay et al. [2026]; Southworth et al. [2022]; NGTS-6: Ivshina & Winn [2022]; Vines et al. [2019]; Griffiths et al. [2026]; NGTS-10: Ivshina & Winn [2022]; McCormac et al. [2020]; Griffiths et al. [2026]; TOI-2109: Alvarado-Montes et al. [2025]; Harre et al. [2024]; NGTS-7A: Jackman et al. [2019]; HATS-70: Ivshina & Winn [2022]; Zhou et al. [2019]; WASP-128: Hodžić et al. [2018]; WASP-87: Ivshina & Winn [2022]; Anderson et al. [2014]; WASP-78: Ivshina & Winn [2022]; Smalley et al. [2012]; Brown et al. [2017]; Qatar-2: Bryan et al. [2012]; Mancini et al. [2014]; Dai et al. [2017]

Table 2.7: Continuation of Table 2.6

Target	TIC ID	Obs-night	Time (hr)	Ncam	Nimage	Airmass
NGTS-10	37348844	30/11/2019	3.0	6	4992	1.15 → 1.0
NGTS-10	37348844	09/12/2020	4.0	4	4420	1.1 → 1.15
NGTS-10	37348844	28/01/2022	4.5	5	5524	1.05 → 1.4
NGTS-10	37348844	17/02/2022	3.5	7	6907	1.0 → 1.25
NGTS-10	37348844	26/12/2022	3.7	7	7262	1.1 → 1.15
NGTS-10	37348844	13/11/2023	2.9	5	4053	1.15 → 1.0
NGTS-10	37348844	19/11/2024	6.2	6	10402	2.0 → 1.1
NGTS-10	37348844	23/02/2025	4.4	6	7313	1.0 → 2.0
NGTS-10	37348844	09/11/2025	2.7	6	4580	1.1 → 1.05
NGTS-10	37348844	08/01/2026	3.2	6	5424	1.15 → 1.0
TOI-2109	392476080	18/06/2022	4.7	4	5296	1.65 → 1.35 → 1.75
TOI-2109	392476080	07/04/2023	3.7	7	7232	1.7 → 1.45
TOI-2109	392476080	06/05/2025	4.2	6	7107	1.75 → 1.35 → 1.5
TOI-2109	392476080	04/06/2025	5.9	6	10039	2.0 → 1.35 → 2.0
TOI-2109	392476080	20/03/2026	2.8	6	4691	2.0 → 1.35
NGTS-7A	2055733261	04/11/2021	3.9	5	5433	1.05 → 1.25
NGTS-7A	2055733261	21/09/2022	7.5	6	12413	1.35 → 1.05 → 1.8
NGTS-7A	2055733261	18/07/2023	3.5	5	4858	1.2 → 1.05
NGTS-7A	2055733261	26/10/2024	4.2	6	7145	1.1 → 1.2
NGTS-7A	2055733261	03/08/2025	7.5	6	12675	2.0 → 1.05 → 1.3
NGTS-7A	2055733261	24/10/2025	4.7	6	7957	1.15 → 1.25
HATS-70	98545929	24/12/2022	7.1	6	11878	1.75 → 1.0 → 1.3
HATS-70	98545929	31/12/2023	7.9	6	12376	1.95 → 1.0 → 1.45
HATS-70	98545929	06/01/2025	5.9	6	9877	1.7 → 1.1
HATS-70	98545929	30/01/2026	5.5	6	9248	1.1 → 1.5
WASP-128	180991313	22/01/2025	4.0	6	6767	2.0 → 1.05
WASP-128	180991313	25/04/2025	7.3	6	12251	1.25 → 1.05 → 2.0
WASP-87	15445551	25/02/2023	6.0	5	8342	1.7 → 1.2
WASP-87	15445551	11/02/2026	5.0	4	5657	1.55 → 1.2
WASP-78	139528693	13/11/2022	7.6	5	10568	2.0 → 1.0 → 1.4
WASP-78	139528693	20/11/2023	8.0	6	13446	2.0 → 1.0 → 1.55
WASP-78	139528693	02/11/2024	7.0	6	11840	2.0 → 1.0 → 1.25
Qatar-2	2521105	05/04/2022	5.0	4	5581	1.35 → 1.05 → 1.3
Qatar-2	2521105	28/03/2023	4.5	6	7522	1.35 → 1.05 → 1.2
Qatar-2	2521105	29/05/2024	4.5	6	7509	1.15 → 1.45
Qatar-2	2521105	11/03/2025	6.4	6	10818	2.0 → 1.05 → 1.3
Qatar-2	2521105	17/05/2025	3.7	6	6337	1.2 → 1.15

Table 2.8: Summary of Danish 1.54m Telescope observations presented in this work.

Target	Obs-night	Time (hr)	Nimage	Texp	Filter	Airmass
WASP-18	17/09/2021	3.9	171	60	V	1.26 → 1.04 → 1.06
WASP-18	02/10/2021	4.0	182	60	V	1.05 → 1.04 → 1.38
WASP-18	05/09/2022	4.2	185	60	V	1.24 → 1.04 → 1.09
WASP-18	20/09/2022	4.6	243	40–40	V	1.05 → 1.04 → 1.38
WASP-18	24/08/2023	4.7	242	50–50	V	1.24 → 1.04 → 1.13
WASP-18	26/09/2023	3.0	198	60	V	1.05 → 1.04 → 1.17
WASP-18	12/08/2024	3.8	155	60	V	1.49 → 1.05
WASP-18	18/09/2025	4.4	185	60	V	1.10 → 1.04 → 1.11
WASP-18	19/09/2025	3.9	168	60	V	1.18 → 1.04 → 1.19
WASP-19	12/04/2026	3.6	341	60	I	1.04 → 1.47
WASP-19	23/04/2026	3.0	192	30–45	I	1.14 → 2.01
WASP-19	16/05/2026	3.0	177	40–60	I	1.06 → 1.47
WASP-43	09/05/2019	3.7	124	85	I	1.06 → 1.86
WASP-43	22/06/2019	3.0	88	100	I	1.23 → 1.06 → 1.22
WASP-43	28/05/2021	3.1	93	100	I	1.15 → 2.65
WASP-43	06/06/2021	3.5	101	100	I	1.08 → 2.16
WASP-43	21/05/2022	3.4	93	100	I	1.06 → 1.06
WASP-43	25/05/2022	3.0	84	100	I	1.12 → 2.30
WASP-43	13/05/2023	3.1	85	100	I	1.15 → 1.06 → 1.13
WASP-43	31/05/2023	3.0	88	100	I	1.07 → 1.66
WASP-43	27/05/2024	3.0	343	10	I	1.07 → 1.66
WASP-43	23/04/2025	2.9	112	50–70	I	1.06 → 1.49
WASP-43	28/05/2025	3.4	95	100	I	1.13 → 2.86
WASP-43	11/04/2026	3.0	241	25–27	I	1.06 → 1.60
WASP-43	29/04/2026	3.0	130	64–68	I	1.10 → 1.06 → 1.21
WASP-43	03/05/2026	2.7	121	45–70	I	1.09 → 1.79
WASP-103	24/04/2026	4.8	174	72–78	R	1.49 → 1.24 → 1.65
WASP-103	07/05/2026	4.7	158	60–90	R	1.44 → 1.24 → 1.72
WASP-103	10/07/2026	3.5	216	60–1–	R	1.25 → 1.24 → 2.08
HATS-18	10/04/2026	3.9	121	100	R	1.00 → 1.64
HATS-18	17/05/2026	3.3	131	50–100	R	1.00 → 1.27
HATS-18	22/05/2026	4.4	121	100	R	1.00 → 1.82
TOI-2109	22/04/2026	3.9	343	20–32	I	1.96 → 1.43 → 1.54
TOI-2109	26/04/2026	3.8	316	15–28	I	1.56 → 1.43 → 1.84
NGTS-7 A	26/05/2026	2.1	77	50–80	I	1.56 → 1.11
NGTS-7 A	07/07/2026	3.7	75	100	I	1.54 → 1.02 → 1.68
NGTS-7 A	09/07/2026	3.6	109	60–100	I	1.32 → 1.01 → 1.33
WASP-128	25/04/2025	4.2	295	30	R	1.18 → 1.02 → 1.11
WASP-128	20/04/2026	5.1	317	20–60	R	1.25 → 1.02 → 1.15
WASP-87	16/04/2026	5.0	914	15	R	1.11 → 1.09 → 1.56
WASP-87	21/04/2026	5.4	995	8	R	1.09 → 2.16
WASP-87	08/05/2026	5.0	527	20	R	1.23 → 1.09 → 1.25
Qatar-2	27/04/2026	3.9	133	70–92	R	2.08 → 1.08
Qatar-2	05/05/2026	3.6	142	100	R	1.33 → 1.08 → 1.34
Qatar-2	09/05/2026	3.1	94	90–100	R	1.26 → 1.08 → 1.11

Table 2.9: Summary of *TESS* observations presented in this work.

Target	TIC ID	Sector	Cadence (s)	Provenance	Camera	CCD
WASP-4	402026209	2	120	SPOC	2	4
WASP-4	402026209	28	20	SPOC	2	3
WASP-4	402026209	29	20	SPOC	2	4
WASP-4	402026209	69	120	SPOC	2	4
WASP-4	402026209	96	20	SPOC	2	4
WASP-4	402026209	103	20	SPOC	4	4
WASP-18	100100827	2	120	SPOC	2	2
WASP-18	100100827	3	120	SPOC	2	1
WASP-18	100100827	29	20	SPOC	2	2
WASP-18	100100827	30	20	SPOC	2	1
WASP-18	100100827	69	20	SPOC	2	2
WASP-18	100100827	96	20	SPOC	2	2
WASP-18	100100827	103	20	SPOC	4	3
WASP-18	100100827	104	20	SPOC	4	2
WASP-19	35516889	9	120	SPOC	2	2
WASP-19	35516889	36	20	SPOC	2	1
WASP-19	35516889	62	120	SPOC	2	2
WASP-19	35516889	63	120	SPOC	2	1
WASP-43	36734222	9	120	SPOC	1	1
WASP-43	36734222	35	20	SPOC	1	2
WASP-43	36734222	62	20	SPOC	1	3
WASP-43	36734222	89	20	SPOC	1	3
WASP-43	36734222	100	20	SPOC	1	4
HATS-18	14614418	10	120	SPOC	1	1
HATS-18	14614418	36	20	SPOC	1	2
HATS-18	14614418	63	120	SPOC	1	2
HATS-18	14614418	90	20	SPOC	1	2
HATS-18	14614418	100	20	SPOC	2	3
HATS-18	14614418	101	20	SPOC	1	4
NGTS-6	1528696	5	120	SPOC	2	2
NGTS-6	1528696	32	20	SPOC	2	1
NGTS-6	1528696	98	20	SPOC	2	1
NGTS-10	37348844	87	20	SPOC	2	1
NGTS-10	37348844	98	20	SPOC	2	2
TOI-2109	392476080	25	1800	SPOC	1	4
TOI-2109	392476080	52	120	SPOC	1	3
TOI-2109	392476080	79	20	SPOC	1	3
NGTS-7A	2055733261	2	1800	QLP	2	4
NGTS-7A	2055733261	29	120	SPOC	2	4
NGTS-7A	2055733261	96	20	SPOC	2	4

Table 2.10: Continuation of Table 2.9

Target	TIC ID	Sector	Cadence (s)	Provenance	Camera	CCD
HATS-70	98545929	7	1800	QLP	2	1
HATS-70	98545929	33	20	SPOC	3	1
HATS-70	98545929	34	20	SPOC	2	1
HATS-70	98545929	61	120	SPOC	2	1
HATS-70	98545929	87	120	SPOC	2	2
HATS-70	98545929	88	120	SPOC	2	1
WASP-128	180991313	10	1800	TESS-SPOC	2	4
WASP-128	180991313	36	120	SPOC	2	3
WASP-128	180991313	37	120	SPOC	2	4
WASP-128	180991313	63	120	SPOC	2	3
WASP-128	180991313	90	120	SPOC	2	3
WASP-128	180991313	99	20	SPOC	3	1
WASP-128	180991313	100	20	SPOC	2	2
WASP-87	15445551	10	120	SPOC	2	2
WASP-87	15445551	11	120	SPOC	2	1
WASP-87	15445551	37	20	SPOC	2	2
WASP-87	15445551	99	20	SPOC	3	4
WASP-87	15445551	100	20	SPOC	3	1
WASP-87	15445551	101	20	SPOC	2	4
WASP-78	139528693	5	120	SPOC	2	1
WASP-78	139528693	31	120	SPOC	2	2
WASP-78	139528693	32	120	SPOC	2	1
Qatar-2 b	2521105	91	20	SPOC	2	3

Chapter 3

Outlook

3.1 Summary

This thesis presents the results of a long-term photometric monitoring campaign of ultra-short period transiting hot Jupiters and brown dwarfs. These objects undergo strong tidal interactions with their host stars, resulting in the tidal decay of their orbits. Transit observations from the NGTS facility and the *TESS* space telescope are analysed and precise mid-transit times derived, before they are combined with observations from the Danish 1.54 m telescope and archival transit observations from the peer reviewed literature.

Through our analysis we derive updated orbital ephemerides for all 15 of our systems. We fit the resulting transit times to linear and quadratic ephemeris models to search for evidence of a changing orbital period. For most systems in this study, our statistical analysis returned no definitive preference for a quadratic ephemeris. For these systems we are still able to derive upper limits on the magnitude of tidal dissipation processes occurring within the host stars.

For five systems in our study, we find a preference for a quadratic trend in the transit timings. A strong quadratic trend is found for the WASP-4 system ($\dot{P} = -5.3 \pm 0.3\,\mathrm{ms\,yr^{-1}}$), a system already known to exhibit an apparently varying orbital period which is thought to be due to an outer companion. For the NGTS-7 A system, our results imply an increasing orbital period ($\dot{P} = +15 \pm 2\,\mathrm{ms\,yr^{-1}}$) - this is probably a light travel time effect due to an outer unseen companion. In our observations of WASP-43 b, WASP-103 b and WASP-128 b, we find a weak preference for a quadratic model which could be due to tidal orbital decay ($\dot{P} = -0.6 \pm 0.2\,\mathrm{ms\,yr^{-1}}$, $-3 \pm 1\,\mathrm{ms\,yr^{-1}}$& $-28 \pm 8\,\mathrm{ms\,yr^{-1}}$ respectively). However analysis of *Gaia* data showing the potential for companions, and previous studies suggesting the presence

of apsidal precession in WASP-43 b, mean the exact nature of these systems remains an open question.

3.2 Future Work

The study of transit-timing variations in exoplanets is at the forefront of developments in time-domain astronomy. Within this thesis I have presented a comprehensive study of transit timing within 15 systems of interest. In this section I outline further work that could be undertaken to help investigate further the possibility of detecting tidal decay in our target systems. Additionally I discuss further observations that would identify orbital decay in these systems.

3.2.1 Further Analysis

Leave-One-Out Analysis

To increase the robustness of our analysis, it would be beneficial to perform a 'bootstrap', or 'leave-one-out' analysis [Wall & Jenkins, 2012], to assess the potential impact of outliers on the interpretation of our results. As explained in Section 2.5.5, we deduced whether a linear or quadratic fit was preferable for the ephemerides of our systems by performing a comparison of the ΔBIC value. However, it is possible that individual transit timing measurements can have an abnormally large effect on the overall result.

To quantify this effect, a statistical test can be performed to re-analyse a given dataset having removed individual data points (or groups of data points). From this, the ΔBIC value can be re-calculated and any outliers identified and closely examined.

An example of the success of this method is illustrated in the large study of Adams et al. [2024]. This work was of a similar scope to the work presented in this thesis, being a large study of transit timing measurements of short period exoplanets over long baselines in order to constrain the presence and rates of tidal decay in these systems. In this work, these authors performed a 'bootstrap' test, as described above, on systems for which a high (ΔBIC>30) preference for a quadratic ephemeris was detected. Performing this test allowed the authors to identify timing points that shifted the derived ΔBIC value by more that 20%. A closer analysis of these data led them to discover significant discrepancies in the literature data sets they used, such as errors in timing systems and instances of observations being reported multiple times.

In this thesis I have followed the rigorous analysis of Adams et al. [2024] in selecting transit timing values from the literature, and adopted their curation of transit times for WASP-19 b entirely. However performing an analysis such as that described above would increase the statistical rigour of the conclusions we have reached through identifying anomalous data-points, and would be a useful addition to large scale statistical studies of this type.

Additional Ephemeris Models

In this study, the data analysed were fit to linear and quadratic ephemeris models, which represent a constant and apparently changing orbital period respectively. In the interpretation of the results, we caution against the implication that a quadratic trend means orbital decay, and refer to it as the apparent reduction in orbital period. In Section 1.6 I discuss alternative scenarios that can appear to mimic orbital decay such as the light-travel time effect and apsidal precession, however it could be possible to place some constraints on the latter effect using available data.

Using Equation 1.34, studies such as Yee et al. [2020] and Bernabò et al. [2024] fit observed mid-transit times to a sinusoidal ephemeris consistent with apsidal precession, a test which could be possible with the data set used in this study. However, as found by the theoretical work of Jackson et al. [2026], who fit similar ephemeris models to simulated data-sets of quadratic ephemerides and calculated the 'observed' ΔBIC value, fitting to transit time observations alone is unlikely to constrain the difference in physical processes. For this, occultation and radial velocity observations will be needed, as discussed in Section 3.2.2.

Tidal Dissipation Modelling

As part of this work, we have calculated the values of $Q'_\star$ predicted by the observed orbital decay rates, or limits on these if no prediction of orbital decay is presented, and it is useful to compare these to those calculated in the theoretical models of Barker [2020]. This work presents a detailed modelling framework for tidal dissipation in a sample of 20 known USP-HJ hosts, including 10 that also form part of our study. Discounting those systems where we suspect additional physical effects are mimicking the presence of orbital decay, we are left with 7 systems to compare to: WASP-18, WASP-19, WASP-103, WASP-128, NGTS-6, NGTS-10 and HATS-18. Of these, the closest match between theory and our observation is found for HATS-18, with a predicted $Q'_\star$ based on IGW dissipation of 1.1×10^5, and an observed value of $> 4.4 \times 10^5$. For all other systems in this joint sample, the theoretical prediction of

Barker [2020] is over an order of magnitude different that our observed value, with $Q'_\star$ higher for observation than theory for WASP-18, WASP-19 and WASP-103, and lower by 3 orders of magnitude for WASP-128. For NGTS-6 and NGTS-10, both our observed value of $Q'_\star$ and that predicted by Barker [2020] are lower limits that differ, but are still consistent.

This difference suggests that either that a refinement to models of tidal dissipation processes is necessary, or additional physical effects are in effect (such as those mentioned in Section 1.6) which are obscuring our view of true tidal dissipation mechanisms. If we are able to rule out false-positive detections with future targeted observations (see Section 3.2.2), the true strength of Internal Gravity Wave dissipation in these stars could begin to be deduced, aiding with theoretical predictions for other systems.

In addition, improvement to age estimates of stars can improve our insight into the tidal dissipation mechanisms in a star. For example, the theoretical work of Alvarado-Montes et al. [2025] found that predictions of $Q'_\star$ for TOI-2109 varied with different age estimates for the star, due to different mechanisms dominating at different evolutionary stages. This is also seen in the form of Inertial Waves becoming dominant as stars evolve off the main sequence [Bryant & Van Eylen, 2025].

3.2.2 Further Targeted Observations

In this thesis I have analysed transit observations of 15 ultra-short period exoplanets and brown dwarfs of interest in front of their host stars. However, further observations of these systems can help to gain insight into their dynamical behaviour.

As discussed in Section 1.6.1, the tidal decay of short period exoplanets can be mimicked by the light-travel time effect from a, sometimes unseen, companion, a hypothesis that has been presented for the apparent orbital period decrease observed in WASP-4 b [e.g. Harre & Smith, 2023; Winn & Stefánsson, 2025, see Section 2.6], and has long been observed for eclipsing binary systems [e.g. Borkovits et al., 2015].

Taking radial velocity observations of the star of interest over as long a baseline as the transit observations has been shown to constrain this effect, contributing to the confirmation of orbital decay in WASP-12 b [Yee et al., 2020] and the hypothesis of LTTE present in WASP-4 [Winn & Stefánsson, 2025]. A radial-velocity curve happening coincident with observed orbital period changes will betray the presence of a companion causing this effect.

It is important however that these observations are taken continuously over a long baseline, similar to transit timing observations, in order to fully constrain

the nature of any observed signal. The companion to WASP-4 b hypothesised by Winn & Stefánsson [2025] to be causing the observed signal has a derived orbital period of 25 yr, meaning observations taken over this baseline will be necessary for full constraints on its behaviour.

Radial velocity observations are also useful in constraining the presence of apsidal precession in a system, due to the information they can give on the eccentricity of a system. Ultra-short period systems are expected to have zero eccentricity due to tidal effects (see Section 1.5.4), however in the presence of a companion a small but non-zero eccentricity can be induced. Radial velocity observations can provide additional information to place constraints on system eccentricity [e.g. Bernabò et al., 2024], making these observations valuable in constraining system behaviours.

Additionally, high contrast imaging using adaptive optics (AO) or lucky imaging can be used to detect companions in these systems, as was deployed for WASP-103 [Wöllert & Brandner, 2015; Ngo et al., 2016]. However, follow up of these images is required to determine the true nature of these companions and whether they are gravitationally bound [e.g. Barros et al., 2022].

In order to determine system eccentricities and therefore constrain rates of apsidal precession, it is very useful to observe the occultations (secondary eclipses) of these systems. As discussed in Jackson et al. [2026] and demonstrated in Yee et al. [2020], tidal decay and apsidal precession appear similarly in plots of transit timings, but trend in opposite directions for occultation timings, a feature which was key to determining the presence of orbital decay in the WASP-12 system. Therefore occultation timing measurements are key to differentiating between these processes.

These observations do, however, come with challenges. Secondary eclipses are notoriously shallow (see Figure 1.2) and often require space-based photometry, such as from the *Spitzer* [Werner et al., 2004] or *James Webb* [Gardner et al., 2006] Space Telescopes to detect. Additionally, they are strongest in the Near-IR range of the spectrum making ground-based observations challenging. However, given the high surface temperature of the close in planets likely to be undergoing decay, targeted observations with 1-2 m class telescopes, such as those used in occultation observations of WASP-12 b [Yee et al., 2020], can also successfully provide the required timing data.

3.2.3 Project continuation

In this thesis, I have presented the results of ∼7 yr of monitoring of known ultra-short period exoplanet and brown dwarf systems with the NGTS and *TESS* observatories, however these observations are set to continue. At the time of writing (August

2026), the observing plan for the *TESS* mission through Cycle 10 is confirmed, covering continuous observations up to September 2028 [1]. This covers many of the systems within this study and means that high-cadence, high-precision photometric observations of them will continue for the foreseeable future.

Additionally, the continuation of the NGTS Orbital Decay programme will allow for high-precision transit observations of systems in this study to continue in the coming years from NGTS.

Further transit observations for some systems in this study will be taken by the *PLATO* mission. As discussed in Section 2.7.6, NGTS-6, NGTS-10 and HATS-70 lie within the LOPS2 field of the *PLATO* mission and are included in the PIC meaning they will receive extremely high precision continuous photometric observations for at least the first two years of the *PLATO* mission. Extensions to this pointing, of up to four or even eight years, will allow for extremely detailed study of these systems to determine their behaviour on an unprecedented baseline of continuous observation (see Eschen et al. (in prep)).

Further transit observations from the continuation of this project will prove vital for constraining the nature of ultra-short period planetary systems, especially for systems in this study such as NGTS-6, NGTS-10 and WASP-128 that show potential for a quadratic trend but need more observations to be able to statistically confirm this. Confirmation of the now known quadratic trends in WASP-4 and WASP-12 took many years and many studies, each with new observations, to confirm (WASP-4: e.g. Bouma et al. [2019]; Harre et al. [2023]; Winn & Stefánsson [2025]; WASP-12: e.g. Maciejewski et al. [2016]; Patra et al. [2017]; Yee et al. [2020]). With the confirmed continuation of transit monitoring of many systems of interests, I hope that more exciting results of this sort are just a few years away.

3.3 Conclusion

The dawn of the field of exoplanet science in 1995, with the discovery of the exoplanet 51 Pegasi b [Mayor & Queloz, 1995], brought a paradigm shift to our knowledge of planetary systems. In particular, the new planet population of hot Jupiters soon gained attention for their potentially short lifespans due to tidal forces [Rasio et al., 1996], and it is these processes that form the basis for this study.

Long-term monitoring campaigns of known transiting systems can shed light into the dynamical behaviour of these systems, as well as interactions between the host star and its companion, and we present the results of such a campaign in this

[1] Full observing details are available at `https://heasarc.gsfc.nasa.gov/docs/tess/`

thesis. Within the constraints of our observations, we are unable to definitively confirm the presence of tidal decay in a system as many other processes can mimic this in transit timing observations, but for five systems, we find strong hints of interesting dynamical processes causing an apparent reduction in orbital period. If these signals are due to tidal decay, they are approximately consistent with those expected but if not, will reveal new dynamics or companions that will make for exciting follow up studies.

Future observations will constrain the exact nature of these processes, and give insights into how they can be measured. The continuation of the *NGTS* and *TESS* missions, as well as future data releases from *Gaia* and *PLATO* have the potential to vastly increase our knowledge of ultra-short period exoplanets and brown dwarfs, making the next few years of exoplanet science a very exciting time.

Bibliography

A-thano N., et al., 2026, AJ, 171, 321

Adams E. R., et al., 2024, Planetary Science Journal, 5, 163

Addison B. C., Tinney C. G., Wright D. J., Bayliss D., 2016, ApJ, 823, 29

Allart R., et al., 2025, Nature Communications, 16, 10822

Alvarado-Montes J. A., Sucerquia M., Zuluaga J. I., Schwab C., 2025, ApJ, 988, 66

Alvarado E., et al., 2024, MNRAS, 534, 800

Anderson D. R., et al., 2014, arXiv e-prints, p. arXiv:1410.3449

Apergis I., et al., 2026, MNRAS, 550, stag1271

Applegate J. H., 1992, ApJ, 385, 621

Auvergne M., et al., 2009, A&A, 506, 411

Bailer-Jones C. A. L., Rybizki J., Fouesneau M., Demleitner M., Andrae R., 2021, AJ, 161, 147

Bailey C., 1926, Epicurus, the extant remains. Clarendon Press

Bakos G., Noyes R. W., Kovács G., Stanek K. Z., Sasselov D. D., Domsa I., 2004, PASP, 116, 266

Ballard S., et al., 2011, ApJ, 743, 200

Baluev R. V., et al., 2019, MNRAS, 490, 1294

Baptista R., Jablonski F., Oliveira E., Vrielmann S., Woudt P. A., Catalán M. S., 2002, MNRAS, 335, L75

Barbary K., 2016, Journal of Open Source Software, 1, 58

Barker A. J., 2020, MNRAS, 498, 2270

Barker A. J., 2022, ApJ, 927, L36

Barker A. J., 2025, in Mandel I., ed., , Vol. 2, Encyclopedia of Astrophysics (First Edition), first edition edn, Elsevier, Oxford, pp 326–348

Barker A. J., Ogilvie G. I., 2010, MNRAS, 404, 1849

Barragán O., et al., 2026, MNRAS, 546, stag087

Barros S. C. C., et al., 2022, A&A, 657, A52

Baruteau C., et al., 2014, in Beuther H., Klessen R. S., Dullemond C. P., Henning T., eds, Protostars and Planets VI. pp 667–689

Baștürk Ö., et al., 2022, MNRAS, 512, 2062

Baștürk Ö., et al., 2025, MNRAS, 541, 714

Bayliss D., et al., 2018, MNRAS, 475, 4467

Beleznay M., Kunimoto M., 2022, MNRAS, 516, 75

Bell T. J., et al., 2024, Nature Astronomy, 8, 879

Benz W., et al., 2021, Experimental Astronomy, 51, 109

Bernabò L. M., Csizmadia S., Smith A. M. S., Rauer H., Hatzes A., Esposito M., Gandolfi D., Cabrera J., 2024, A&A, 684, A78

Bernabò L. M., et al., 2025, A&A, 694, A233

Bertin E., Arnouts S., 1996, A&AS, 117, 393

Birkby J. L., 2018, in Deeg H. J., Belmonte J. A., eds, , Handbook of Exoplanets. Springer International Publishing, pp 1485–1508

Biswas S., et al., 2025, AJ, 170, 133

Bonomo A. S., et al., 2017, A&A, 602, A107

Borges B. W., Baptista R., Papadimitriou C., Giannakis O., 2008, A&A, 480, 481

Borkovits T., Rappaport S., Hajdu T., Sztakovics J., 2015, MNRAS, 448, 946

Borucki W. J., et al., 2010, Science, 327, 977

Bouma L. G., et al., 2019, AJ, 157, 217

Bouma L. G., Winn J. N., Howard A. W., Howell S. B., Isaacson H., Knutson H., Matson R. A., 2020, ApJ, 893, L29

Bressan A., Marigo P., Girardi L., Salasnich B., Dal Cero C., Rubele S., Nanni A., 2012, MNRAS, 427, 127

Brown D. J. A., Collier Cameron A., Hall C., Hebb L., Smalley B., 2011, MNRAS, 415, 605

Brown D. J. A., et al., 2017, MNRAS, 464, 810

Bryan M. L., et al., 2012, ApJ, 750, 84

Bryant E. M., Van Eylen V., 2025, MNRAS, 544, 1186

Bryant E. M., et al., 2020, MNRAS, 494, 5872

Caldwell D. A., et al., 2020, Research Notes of the American Astronomical Society, 4, 201

Campbell B., Walker G. A. H., Yang S., 1988, ApJ, 331, 902

Castro-Ginard A., et al., 2024, A&A, 688, A1

Chakrabarty A., Sengupta S., 2019, AJ, 158, 39

Chaplin W. J., Miglio A., 2013, ARA&A, 51, 353

Charbonneau D., Brown T. M., Latham D. W., Mayor M., 2000, ApJ, 529, L45

Charbonneau D., Brown T. M., Noyes R. W., Gilliland R. L., 2002, ApJ, 568, 377

Chen G., et al., 2014, A&A, 563, A40

Chen D.-C., et al., 2023, Proceedings of the National Academy of Science, 120, e2304179120

Choi J., Dotter A., Conroy C., Cantiello M., Paxton B., Johnson B. D., 2016, ApJ, 823, 102

Cochran W. D., Hatzes A. P., 1994, Ap&SS, 212, 281

Collier Cameron A., Jardine M., 2018, MNRAS, 476, 2542

Cortés-Zuleta P., Rojo P., Wang S., Hinse T. C., Hoyer S., Sanhueza B., Correa-Amaro P., Albornoz J., 2020, A&A, 636, A98

D'Amico M., 2000, Giordano Bruno: Avventure e Misteri Del Grande Mago Nell'europa Del Cinquecento. Piemme, Casale Monferrato (Alessandria)

Dai F., Winn J. N., Yu L., Albrecht S., 2017, AJ, 153, 40

Darwin G. H., 1880, Philosophical Transactions of the Royal Society of London Series I, 171, 713

Davoudi F., Baştürk Ö., Yalçınkaya S., Esmer E. M., Safari H., 2021, AJ, 162, 210

Dawson R. I., Johnson J. A., 2018, ARA&A, 56, 175

De K., et al., 2023, Nature, 617, 55

Delrez L., et al., 2018, MNRAS, 474, 2334

Dominik M., et al., 2010, AN, 331, 671

Doyle L., et al., 2022, MNRAS, 516, 298

Dragomir D., et al., 2011, AJ, 142, 115

Durisen R. H., Boss A. P., Mayer L., Nelson A. F., Quinn T., Rice W. K. M., 2007, in Reipurth B., Jewitt D., Keil K., eds, Protostars and Planets V. p. 607

Eastman J., Siverd R., Gaudi B. S., 2010, PASP, 122, 935

Edwards R. T., Hobbs G. B., Manchester R. N., 2006, MNRAS, 372, 1549

Ehrenreich D., et al., 2020, Nature, 580, 597

Eschen Y. N. E., Bayliss D., Wilson T. G., Kunimoto M., Pelisoli I., Rodel T., 2024, MNRAS, 535, 1778

Espinoza N., et al., 2019, MNRAS, 482, 2065

Esposito M., et al., 2017, A&A, 601, A53

Ford E. B., et al., 2012, ApJ, 750, 113

Foreman-Mackey D., Hogg D. W., Lang D., Goodman J., 2013, PASP, 125, 306

Fortney J. J., Dawson R. I., Komacek T. D., 2021, Journal of Geophysical Research (Planets), 126, e06629

Gaia Collaboration et al., 2016, A&A, 595, A1

Gaia Collaboration et al., 2023, A&A, 674, A1

Garai Z., et al., 2021, MNRAS, 508, 5514

Gardner J. P., et al., 2006, Space Sci. Rev., 123, 485

Gill S., et al., 2020, ApJ, 898, L11

Gillen E., et al., 2020, MNRAS, 492, 1008

Gillon M., et al., 2009, A&A, 496, 259

Gillon M., et al., 2012, A&A, 542, A4

Gillon M., et al., 2014, A&A, 562, L3

Giménez A., Bastero M., 1995, Ap&SS, 226, 99

Goldreich P., Soter S., 1966, Icarus, 5, 375

Goldreich P., Tremaine S., 1980, ApJ, 241, 425

Gray D. F., 2022, The Observation and Analysis of Stellar Photospheres, 4 edn. Cambridge University Press

Griffiths A. W., et al., 2026, MNRAS, 545, staf2057

Hamer J. H., Schlaufman K. C., 2019, AJ, 158, 190

Harre J.-V., Smith A. M. S., 2023, Universe, 9, 506

Harre J.-V., et al., 2023, A&A, 669, A124

Harre J.-V., et al., 2024, A&A, 692, A254

Haswell C. A., 2010, Transiting Exoplanets. Cambridge University Press

Hebb L., et al., 2009, ApJ, 693, 1920

Hebb L., et al., 2010, ApJ, 708, 224

Hellier C., et al., 2009, Nature, 460, 1098

Hellier C., et al., 2011a, A&A, 535, L7

Hellier C., Anderson D. R., Collier-Cameron A., Miller G. R. M., Queloz D., Smalley B., Southworth J., Triaud A. H. M. J., 2011b, ApJ, 730, L31

Hodžić V., et al., 2018, MNRAS, 481, 5091

Holman M. J., Murray N. W., 2005, Science, 307, 1288

Holman M. J., et al., 2010, Science, 330, 51

Howell S. B., et al., 2014, PASP, 126, 398

Hoyer S., et al., 2013, MNRAS, 434, 46

Hoyer S., Pallé E., Dragomir D., Murgas F., 2016, AJ, 151, 137

Hu Q., Zhu W., Huang Y., Zhang B., 2026, arXiv e-prints, p. arXiv:2608.12790

Huang C. X., et al., 2020a, Research Notes of the American Astronomical Society, 4, 204

Huang C. X., et al., 2020b, Research Notes of the American Astronomical Society, 4, 206

Huitson C. M., Désert J.-M., Bean J. L., Fortney J. J., Stevenson K. B., Bergmann M., 2017, AJ, 154, 95

Husser T.-O., Wende-von Berg S., Dreizler S., Homeier D., Reiners A., Barman T., Hauschildt P. H., 2013, A&A, 553, A6

Hut P., 1981, A&A, 99, 126

Irwin J. B., 1952, ApJ, 116, 211

Ivshina E. S., Winn J. N., 2022, ApJS, 259, 62

Jackman J. A. G., et al., 2019, MNRAS, 489, 5146

Jackman J. A. G., et al., 2021, MNRAS, 504, 3246

Jackson B., Adams E. R., Huchmala R. M., Barker M., Rothmeier M., Morgenthaler J. P., Sickafoose A. A., 2026, AJ, 171, 103

Jenkins J. M., et al., 2016, in Chiozzi G., Guzman J. C., eds, Society of Photo-Optical Instrumentation Engineers (SPIE) Conference Series Vol. 9913, Software and Cyberinfrastructure for Astronomy IV. p. 99133E

Jiang I.-G., Lai C.-Y., Savushkin A., Mkrtichian D., Antonyuk K., Griv E., Hsieh H.-F., Yeh L.-C., 2016, AJ, 151, 17

Kipping D. M., 2009, MNRAS, 392, 181

Kirk J., et al., 2021, AJ, 162, 34

Knutson H. A., Charbonneau D., Noyes R. W., Brown T. M., Gilliland R. L., 2007, ApJ, 655, 564

Kopal Z., 1950, Harvard College Observatory Circular, 454, 1

Kozai Y., 1962, AJ, 67, 591

Kreidberg L., 2015, PASP, 127, 1161

Kreidberg L., et al., 2015, ApJ, 814, 66

Kreidberg L., et al., 2018, AJ, 156, 17

Kutluay A. C., et al., 2026, PASP, 138, 024405

Lammers C., Winn J. N., 2026, AJ, 171, 18

Lau R. M., et al., 2025, ApJ, 983, 87

Lendl M., Gillon M., Queloz D., Alonso R., Fumel A., Jehin E., Naef D., 2013, A&A, 552, A2

Lendl M., Cubillos P. E., Hagelberg J., Müller A., Juvan I., Fossati L., 2017, A&A, 606, A18

Lidov M. L., 1962, Planet. Space Sci., 9, 719

Lin D. N. C., Bodenheimer P., Richardson D. C., 1996, Nature, 380, 606

Love A. E. H., 1909, Proceedings of the Royal Society of London Series A, 82, 73

Ma X., et al., 2025, AJ, 169, 169

Maciejewski G., et al., 2016, A&A, 588, L6

Maciejewski G., et al., 2018, Acta Astron., 68, 371

Maciejewski G., Knutson H. A., Howard A. W., Isaacson H., Fernández-Lajús E., DiSisto R. P., Migaszewski C., 2020, Acta Astron., 70, 1

Maciejewski G., et al., 2022, A&A, 667, A127

Maciejewski G., Golonka J., Fernández M., Ohlert J., Casanova V., Pérez Medialdea D., 2024, A&A, 692, A35

Madhusudhan N., et al., 2011, Nature, 469, 64

Mancini L., et al., 2013, MNRAS, 436, 2

Mancini L., et al., 2014, MNRAS, 443, 2391

Mandel K., Agol E., 2002, ApJ, 580, L171

Marcy G. W., Benitz K. J., 1989, ApJ, 344, 441

Maxted P. F. L., et al., 2013, MNRAS, 428, 2645

Mayor M., Queloz D., 1995, Nature, 378, 355

McCormac J., Pollacco D., Skillen I., Faedi F., Todd I., Watson C. A., 2013, PASP, 125, 548

McCormac J., et al., 2020, MNRAS, 493, 126

McDonald I., Kerins E., 2018, MNRAS, 477, L21

Miyazaki S., Masuda K., 2023, AJ, 166, 209

Montalto M., et al., 2026, arXiv e-prints, p. arXiv:2604.03369

Močnik T., Southworth J., Hellier C., 2017, MNRAS, 471, 394

Mullen E. H., Conti D. M., Collins K. A., 2026, Research Notes of the American Astronomical Society, 10, 165

Murgas F., Pallé E., Zapatero Osorio M. R., Nortmann L., Hoyer S., Cabrera-Lavers A., 2014, A&A, 563, A41

Murphy M. M., et al., 2023, AJ, 165, 107

Murray C. D., Correia A. C. M., 2010, in Seager S., ed., , Exoplanets. University of Arizona Press, Tuscon, pp 15–23

Naponiello L., 2026, A&A, 705, A5

Nascimbeni V., et al., 2022, A&A, 658, A31

Nascimbeni V., et al., 2025, A&A, 694, A313

Nelder J. A., Mead R., 1965, The Computer Journal, 7, 308

Newville M., Stensitzki T., Allen D. B., Rawlik M., Ingargiola A., Nelson A., 2016, Lmfit: Non-Linear Least-Square Minimization and Curve-Fitting for Python, Astrophysics Source Code Library, record ascl:1606.014 (ascl:1606.014)

Ngo H., et al., 2016, ApJ, 827, 8

Nikolov N., Henning T., Koppenhoefer J., Lendl M., Maciejewski G., Greiner J., 2012, A&A, 539, A159

O'Brien S. M., et al., 2022, MNRAS, 509, 6111

O'Brien S. M., et al., 2025, AJ, 170, 316

Ogilvie G. I., 2014, ARA&A, 52, 171

Ogilvie G. I., Lin D. N. C., 2004, ApJ, 610, 477

Owen J. E., 2019, Annual Review of Earth and Planetary Sciences, 47, 67

Parviainen H., Aigrain S., 2015, MNRAS, 453, 3821

Patra K. C., Winn J. N., Holman M. J., Yu L., Deming D., Dai F., 2017, AJ, 154, 4

Patra K. C., et al., 2020, AJ, 159, 150

Penev K., 2026, in Mandel I., ed., , Encyclopedia of Astrophysics (First Edition), 1st edn, Elsevier, Oxford, pp 510–519

Penev K., et al., 2016, AJ, 152, 127

Penev K., Bouma L. G., Winn J. N., Hartman J. D., 2018, AJ, 155, 165

Penoyre Z., Belokurov V., Evans N. W., 2022, MNRAS, 513, 2437

Pepper J., et al., 2007, PASP, 119, 923

Petrucci R., Jofré E., Schwartz M., Cúneo V., Martínez C., Gómez M., Buccino A. P., Mauas P. J. D., 2013, ApJ, 779, L23

Petrucci R., Jofré E., Gómez Maqueo Chew Y., Hinse T. C., Mašek M., Tan T.-G., Gómez M., 2020, MNRAS, 491, 1243

Pollacco D. L., et al., 2006, PASP, 118, 1407

Pollack J. B., Hubickyj O., Bodenheimer P., Lissauer J. J., Podolak M., Greenzweig Y., 1996, Icarus, 124, 62

Pont F., Husnoo N., Mazeh T., Fabrycky D., 2011, MNRAS, 414, 1278

Rafikov R. R., 2005, ApJ, 621, L69

Ragozzine D., Wolf A. S., 2009, ApJ, 698, 1778

Rajkumar A. R., et al., 2026, A&A, 708, A313

Ranjan S., Charbonneau D., Désert J.-M., Madhusudhan N., Deming D., Wilkins A., Mandell A. M., 2014, ApJ, 785, 148

Rasio F. A., Ford E. B., 1996, Science, 274, 954

Rasio F. A., Tout C. A., Lubow S. H., Livio M., 1996, ApJ, 470, 1187

Rauer H., et al., 2025, Experimental Astronomy, 59, 26

Ricci D., et al., 2015, PASP, 127, 143

Ricker G. R., et al., 2015, Journal of Astronomical Telescopes, Instruments, and Systems, 1, 014003

Rodel T., et al., 2025, MNRAS, 537, 35

Rodel T., et al., 2026, MNRAS, 549, stag1061

Roemer O., 1677, Philosophical Transactions of the Royal Society, 12, 893

Rosário N. M., Barros S. C. C., Demangeon O. D. S., Santos N. C., 2022, A&A, 668, A114

Russell H. N., 1912, ApJ, 36, 54

Saha S., Chakrabarty A., Sengupta S., 2021, AJ, 162, 18

Sanchis-Ojeda R., Winn J. N., Holman M. J., Carter J. A., Osip D. J., Fuentes C. I., 2011, ApJ, 733, 127

Sarkis P., Mordasini C., Henning T., Marleau G. D., Mollière P., 2021, A&A, 645, A79

Schlichting H. E., 2014, ApJ, 795, L15

Schneider J., 2005, in Sterken C., ed., Astronomical Society of the Pacific Conference Series Vol. 335, The Light-Time Effect in Astrophysics: Causes and cures of the O-C diagram. p. 191

Schwarz G., 1978, Annals of Statistics, 6, 461

Sedaghati E., et al., 2017, Nature, 549, 238

Smalley B., et al., 2012, A&A, 547, A61

Smith A. M. S., Eigmüller P., Oshagh M., Southworth J., 2020a, Research Notes of the American Astronomical Society, 4, 23

Smith A. M. S., et al., 2020b, Astronomische Nachrichten, 341, 273

Southworth J., 2008, MNRAS, 386, 1644

Southworth J., 2013, A&A, 557, A119

Southworth J., Maxted P. F. L., Smalley B., 2004, MNRAS, 351, 1277

Southworth J., et al., 2009, MNRAS, 396, 1023

Southworth J., et al., 2014, MNRAS, 444, 776

Southworth J., et al., 2015, MNRAS, 447, 711

Southworth J., et al., 2019, MNRAS, 490, 4230

Southworth J., et al., 2022, MNRAS, 515, 3212

Stassun K. G., et al., 2018, AJ, 156, 102

Stassun K. G., et al., 2019, AJ, 158, 138

Stetson P. B., 1987, PASP, 99, 191

Stevenson K. B., et al., 2014, Science, 346, 838

Stevenson K. B., et al., 2017, AJ, 153, 68

Toomre A., 1964, ApJ, 139, 1217

Tregloan-Reed J., Southworth J., Tappert C., 2013, MNRAS, 428, 3671

Trotta R., 2024, Starborn. Basic Books

Turner J. D., et al., 2017, MNRAS, 472, 3871

Turner J. D., Flagg L., Ridden-Harper A., Jayawardhana R., 2022, AJ, 163, 281

Van Eylen V., Winn J. N., Albrecht S., 2016, ApJ, 824, 15

Vines J. I., et al., 2019, MNRAS, 489, 4125

Vissapragada S., et al., 2022, ApJ, 941, L31

Wall J. V., Jenkins C. R., 2012, Practical Statistics for Astronomers. Cambridge University Press

Wang X.-Y., et al., 2021, ApJS, 255, 15

Wang W., Ma X., Chen Z., Yu C., Liu S., Ma B., 2025, ApJ, 986, 121

Watson C. A., Marsh T. R., 2010, MNRAS, 405, 2037

Werner M. W., et al., 2004, ApJS, 154, 1

West R. G., et al., 2019, MNRAS, 486, 5094

Wheatley P. J., et al., 2018, MNRAS, 475, 4476

Wilkins A. N., Delrez L., Barker A. J., Deming D., Hamilton D., Gillon M., Jehin E., 2017, ApJ, 836, L24

Wilson D. M., et al., 2008, ApJ, 675, L113

Winn J. N., 2010, in Seager S., ed., , Exoplanets. University of Arizona Press, Tuscon, pp 55–77

Winn J. N., Stefánsson G., 2025, Planetary Science Journal, 6, 300

Winn J. N., Holman M. J., Carter J. A., Torres G., Osip D. J., Beatty T., 2009, AJ, 137, 3826

Wöllert M., Brandner W., 2015, A&A, 579, A129

Wolszczan A., Frail D. A., 1992, Nature, 355, 145

Woltjer Jr. J., 1922, Bull. Astron. Inst. Netherlands, 1, 93

Wong I., et al., 2021, AJ, 162, 256

Wright T., 1750, An original theory or new hypothesis of the universe. H. Chapelle

Yee S. W., et al., 2020, ApJ, 888, L5

Zhou G., et al., 2019, AJ, 157, 31

van Helden A., 1983, Journal for the History of Astronomy, 14, 137